Integrated Waveguide Interfaces for Quantum Optics Applications

by

Rubayet Al Maruf

A thesis
presented to the University of Waterloo
in fulfillment of the
thesis requirement for the degree of
Doctor of Philosophy
in
Electrical and Computer Engineering (Quantum Information)

Waterloo, Ontario, Canada, 2020

Examining Committee Membership

The following served on the Examining Committee for this thesis. The decision of the Examining Committee is by majority vote.

External Examiner:	Ray DeCorby Professor, Dept. of Electrical and Computer Engineering, University of Alberta
Supervisor(s):	Michal Bajcsy Associate Professor, Dept. of Electrical and Computer Engineering, University of Waterloo
Internal Member:	Na Young Kim Associate Professor, Dept. of Electrical and Computer Engineering, University of Waterloo
Internal Member:	Thomas Jennewein Associate Professor, Dept. of Physics and Astronomy, University of Waterloo
Internal-External Member:	Kyung Soo Choi Assistant Professor, Dept. of Physics and Astronomy, University of Waterloo

Author's Declaration

I hereby declare that I am the sole author of this thesis. This is a true copy of the thesis, including any required final revisions, as accepted by my examiners.

I understand that my thesis may be made electronically available to the public.

Abstract

This dissertation explores the integration and interfacing of a variety of photonic devices with optical waveguides, aiming to minimize the optical losses and physical footprint of such systems. The specific investigations include interfacing solid-core and hollow-core optical fibers, development of a monolithic single-photon source based on a quantum dot embedded in a semiconductor nanowire aligned with a single-mode fiber, a proposal for a waveguide-integrated power limiter that can protect detectors in a quantum key distribution (QKD) network, and integrating superconducting-nanowire single photon detectors (SNSPD) with laser-written waveguides.

Hollow-core photonic-crystal fibers (HCPCFs), which can allow simultaneous tight confinement of both photons and atoms in their hollow core, offer a platform for enhancing interactions between light and atomic ensembles. However, interfacing HCPCFs with conventional solid core (SC) fibers presents a unique set of challenges including significant losses in the joint region due to partial melting and deformation of the photonic crystal during the conventional arc-fusion splicing process. We address this issue with a lithographically defined, vacuum-compatible on-chip structure acting as a mechanical splicer that allows efficient injection of light from a SC fiber to a HCPCF and vice versa, with maximum observed light injection efficiency from a single-mode SC fiber into a HCPCF of 90%.

Single photon sources (SPS) are often required in photonic quantum information applications. Among various candidates, quantum dots (QD) embedded in tapered semiconductor nanowires have demonstrated excellent progress so far to realize a SPS. However, the overall collection efficiency of the emitted photon into a single mode fiber remains as one of the major challenges, mainly due to loss in the intermediate optical components. We design a complete scheme for high efficiency light coupling from such quantum dot to a single mode fiber. We optimize the geometry of the tapered nanowire to achieve a low numerical aperture Gaussian output mode profile from the wire tip and use a lithographically defined structure to align the SMF collecting the emitted photons. A graded-index multimode fiber acting as a lens is spliced on the SMF end for high efficiency coupling of light from the nanowire into the fiber.

Extremely sensitive photonic devices are often used in quantum optics applications for detection and manipulation of signals with very low power. To prevent malfunction or even damage to these sensitive devices by excess incident power, we propose an optical power limiter based on a pair of cavities integrated with optical waveguides. Such power limiter can be used to protect sensitive electro-optical devices and prevent certain types of attacks on QKD systems.

Lastly, a 2D photonic lattice formed by laser-written waveguides in bulk glass can be used as an analogue quantum simulator. We explore the integration of SNSPDs with laser-written waveguides with the goal of making this platform fully on-chip.

Acknowledgements

Graduate life was an emotional journey for me! It was the most challenging, at the same time most fulfilling part of my entire educational pursuit. I would like to sincerely acknowledge the many people who mentored me, criticized me, helped me in the difficult times, and made me a better person today.

First of all, I would like to express my sincere gratitude to my supervisor Prof. Michal Bajcsy, whose constant guidance, support and encouragement helped me to endure the entire journey of the doctoral study. I have learned the basics of hands on optics experiments, importance of small details in the laboratory, consequence of not maintaining a detailed notebook, and so many other things from him. I really admire him for his teaching methods of using anecdotes and funny stories to convey valuable life lessons. I would like to explicitly mention his support during the difficult times in my personal life, as well as in financial needs. He was the person I could rely on duirng the strenous times of graduate student life.

I got the opportunity to work with many Postdocs who shared their knowledge and wisdom that helped me to learn a great deal. When I started my study here, Chris Haapamaki and Taehyun Yoon were the Postdocs who taught me many things in the lab and in the cleanroom. I could just go to them whenever I needed advice and they were very enthusiastic to help me. Fereshteh Rajabi joined the group near the mid point of my study and we had a good friendship outside of the academic arena. I was very lucky to work with Behrooz Semnani towards the end of my study who is not only a very knowledgable person, but also admirably passionate about science. We spent a lot of time discussing about science, philosphy and life in general. I met Divya Bharadwaj at the very end of my study who helped me whenever I needed.

The place where I spent most time in the university is my office in QNC. I was fortunate enough to have great office mates like Jeremy Flannery, Andy Ding and Golam Bappi. Jeremy is one of smarterst and coolest persons I have ever met. Our after lunch discussion on random topics including science, culture, music, movies, philosophy and other issues certainly enriched my knowledge and broaden my horizon. I couldn't have asked for a better person other than Jeremy for spending long five years as my office mate. Apart from them, I am very thankful to my group mates Paul Anderson, Sai Sreesh Venuturumilli, Vinodh Raj Rajagopal Muthu, Supratik Sarkar, Cameron Vickers, Sema Kuru, Jackson Qiu and others for their valuable help and support.

My friends and colleagues in IQC always created such an environment that encouraged me to go to the university everyday. Here I met the brightest minds from across the world whose presence stimulated my thirst for knowledge. All the staff members of IQC and QNC including administration, IT and NanoFab have always tried to help us in everyway possible.

It's hard to properly describe the role my parents, sister and family in the entirety of my educational career. They are the reason behind the person who I am today. Though I lived almost half of the world away from my family, they were always a phone call away. Since my childhood, my parents always supported me in every way possible to pursue my dream. They showed me the path to be a good human being. Along with my family, my friends and peers in Waterloo, in Bangladesh, and across the world basically shaped my persona. I can't emphasize enough to express my gratitude for having such great friends and family who really care.

Dedication

This thesis is dedicated to my parents who have encouraged and supported me throughout my entire life.

Contents

List of Figures

List of Tables

Chapter 1

Introduction

In the late nineteenth and early twentieth century, scientific community observed several phenomena including black-body radiation and photoelectric effect those were not correctly explained by existing classical physics. Max Planck proposed the famous Planck's law in 1900 to theoretically explain the experimentally observed black-body radiation and Albert Einstein proposed the concept of light as discrete quantized packets to explain the experimental observation of photoelectric effect in his groundbreaking paper in 1905. The idea of quantized picture of electromagnetic radiation along with the wave nature essentially led to the discovery of the fundamental theory in physics called quantum mechanics. Quantum mechanics encompasses the study of nature on an atomic scale, however, the branch of quantum mechanics study the behavior of light quanta is called quantum optics.

Unlike electrons, photons being neutral particles do not interact with each other directly, rather requires a medium to interact. In quantum optical treatment, light is regarded as photons and matter as atoms. Due to this inherent requirement, though most of the fundamental theories of quantum optics were developed in twentieth century, the experimental realization is being done gradually with the necessary technological advancement. Initially the proof of concept is demonstrated using large experimental setup, usually on a table top using bulk components for quantum optics. However, incorporation of several functionalities, smaller footprints, and often higher efficiency demand for on-chip integration of photonic components.

One of the major areas of applications of quantum optics is in the field of quantum information, where the unique properties of quantum mechanics is implemented in information science. Advantages of quantum information includes secure communication using quantum states as the information carrier (Quantum Key Distribution or QKD) compared to their classical counterpart, as well as the advent of quantum computing where superposition and entanglement of the quantum states are used for computation. Quantum computing has the potential to revolutionize computation by making certain types of classically intractable problems solvable. Quantum communication has the advantage of being theoretically secure unlike classical communication which is mostly practically secure. However, in photonic quantum communication, one of the major challenges is the efficient transport of the photons.

Intra-chip and inter-chip photon transport requires waveguides to guide light from one point to another. On-chip waveguides in visible and near-infrared frequencies are generally made of dielectric materials and the dimensions are on the order of the wavelengths. Optical fibers (waveguide made of glass) and/or free-space propagation is used to transport light from few centimeters to thousands of kilometers. However, interfaces among waveguides and photonic components often incur losses due to material properties and/or modal properties. It is imperative to have efficient coupling between photonic devices and waveguides

for large scale integration, as well as for practical applications. In this thesis, such possibilities are explored for efficient coupling between waveguides and photonic devices.

Apart from efficient interfacing among photonic components, novel devices or existing devices on a novel platform are often required to further enhance the functionality or introduce new functionality. In this thesis, two such cases are explored: an optical power limiter integrated with an optical filter and a single photon detector integrated on a glass waveguide platform. Both of the devices could have additional applications outside of the specific platform considered in this thesis.

A long sought goal in quantum information is to have a quantum network consisting of quantum nodes and channels (Figure 1.1), where quantum nodes could be source, memory or processor for generation, storing and processing of quantum states and quantum channels could be waveguides or free space for transporting quantum states from one site to another. Consider a small segment of the network consists of three nodes: A, B and C. Node A is a single photon source, Node B is a memory element and there is a QKD channel between Node A and C. In this case, the single photon source is a quantum dot embedded in a semiconductor nanowire and the memory element is a cold atomic ensemble in a hollow-core

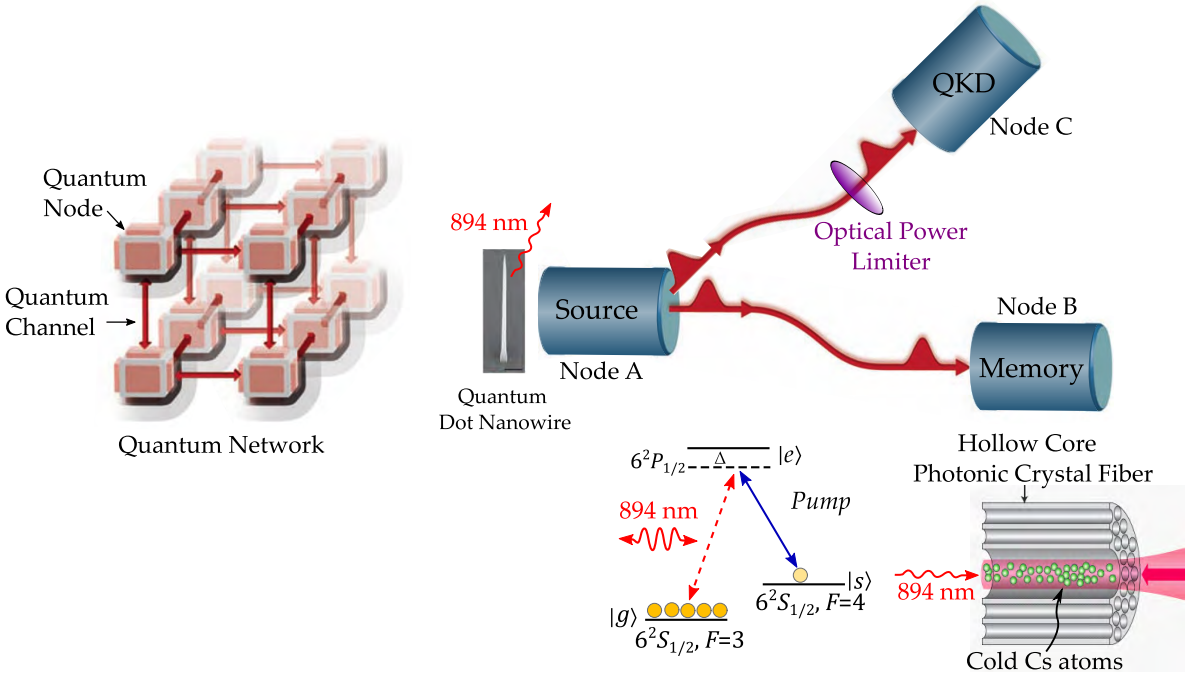

FIGURE 1.1: (left) Schematic of a Quantum Network consisting of quantum nodes and quantum channels [1]. (right) Small segment of a network with three nodes: Node A is a single photon source, Note B being a memory element and there is a QKD channel between Node A and C. The single photon source (at 894 nm) is a quantum dot embedded in a semiconductor nanowire (nanowire image from [2]). The memory element is a Cs cold atomic ensemble in a hollow-core photonic-crystal fiber, which can store the emitted photons from the quantum dot. A three level Λ-scheme shows the memory operation of the cold Cs atoms: 894 nm photons can excite electrons from $|g\rangle$ to $|e\rangle$ and then they decay to $|s\rangle$ (write operation), and then a classical pump can retrieve the photons by coupling $|s\rangle$ and $|e\rangle$ (read operation).

photonic-crystal fiber. In chapter 2 (summarized in section 1.1), an on-chip fiber splicer is demonstrated for efficient coupling of light between photonic-crystal and solid-core fibers, where the solid-core fiber can serve as a quantum channel. In chapter 3 (summarized in section 1.2), a scheme is proposed for efficient collection of photons from the quantum dot source to a single mode fiber. In chapter 4 (summarized in section 1.3), an optical power limiter integrated with an optical filter is proposed for preventing 'blinding attack' on a QKD system [3, 4]. Apart from that, the possibility of integrating a single photon detector on a photonic lattice platform is explored in chapter 5 (summarized in section 1.4). A photonic lattice is made of waveguides written in the glass substrate using femtosecond laser pulses, has the advantage of being able to 2D or 3D structures, and could be used for on-chip analog quantum simulator. An example is illustrated in Figure 1.2 where a controlled NOT (CNOT) gate is implemented on the photonic lattice platform [5]. Integration of the single photon detectors on the chip could make the experimental setup more efficient with smaller footprint.

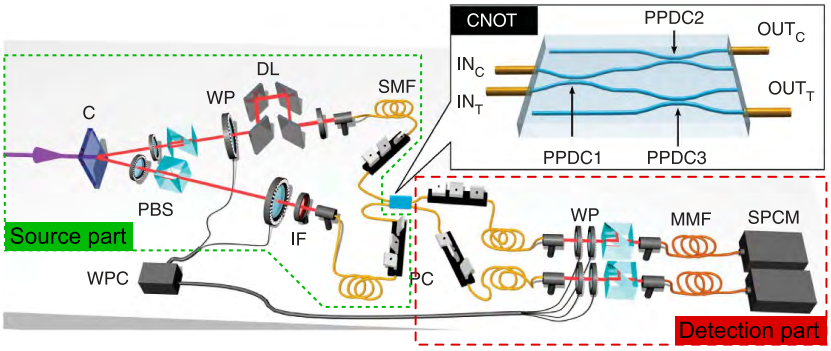

FIGURE 1.2: A controlled NOT (CNOT) gate is implemented on the photonic lattice platform [5]. The overall experimental setup can be conceptually divided into three parts: source, CNOT gate and detection. An integrated single photon detector on the chip could make the setup more efficient with smaller footprint.

1.1 On-chip splicer for coupling light between photonic-crystal and solid-core fibers

Efficient light-matter interaction is the heart of nonlinear quantum optics. However, the probability of interaction between a single atom and a photon in free space is very low. An ensemble of atoms can increase the probability of interaction, however, to obtain optical nonlinearity at single photon levels, the electric field of a single photon needs to be increased, e.g., through spatial confinement of the photon. Several waveguide-based platforms have been explored for this approach including tapered optical nanofibers [6], planar photonic crystal waveguides [7] and hollow-core photonic crystal fibers[8].

Hollow-core photonic-crystal fibers (HCPCFs) can allow simultaneous tight confinement of both photons and atoms in their hollow core region and offer a platform for enhancing interactions between light and atomic ensembles. However, interfacing HCPCFs with conventional solid core (SC) fibers presents a unique set of challenges including significant losses in the joint region due to partial melting and deformation of the photonic crystal region during the conventional arc-fusion splicing process. Several techniques have been employed to reduce the splice loss between solid-core and hollow core fibers including the use of CO_2 laser

[9], graded index fiber [10], modified arc discharge on the joint [11, 12], overlap between fibers [13] and N_2 pressure to prevent hole collapse [14].

Loss in a fiber joint usually caused by the mode field area mismatch between the two fibers, misalignment of the optical axis, reflection from the air-glass interface and the deformation of the fiber structure in the joint region when HCPCFs are joined with solid-core fibers. While the mode field area mismatch puts essentially a fundamental lower limit on the loss in the fiber joint, the other losses depend on the technique used to join the fibers. Mechanical splicing avoids losses caused by the fiber deformation, but requires careful alignment [15]. One way to achieve a precise alignment between two fiber ends is to use optical lithography to form on-chip structures, such as etched V-grooves in silicon [16] and fiber clamping structures [17] formed by undercut in thick photoresist. The latter in particular provides an excellent mechanical stability and has been successfully used to align high-finesse optical cavities formed between two fiber faces in ultra-high vacuum environment. Here, we investigate the lithographically defined alignment method to implement a mechanical splicer for HCPCFs and present a modification to the structure that enables sub-micron precision alignment and splicing for fibers with different cladding diameters.

1.2 High efficiency fiber-coupled single-photon source based on quantum dot embedded in a semiconductor nanowire

Single photon sources (SPS) are often required in photonic quantum information applications. Commonly used approaches for generation of single photons include nonlinear frequency conversion and spontaneous emission of single quantum emitter. The spontaneous emission from a two-level quantum emitter is inherently single-photon like. Early demonstrations of single-photon emission were based on atoms [18], ions [19] and molecules [20], and followed by demonstrations with artificial atoms in a solid-state environment. Among various candidates, quantum dots (QD), an artificial atom, embedded in tapered semiconductor nanowires have demonstrated excellent progress so far to realize a SPS [21].

However, one of the major challenges remains the overall collection efficiency of the emitted photon into a single mode fiber due to high refractive index contrast of the III-V semiconductors and air. Several schemes have been proposed to overcome this challenge where nanophotonic structures including micropillar cavities [22, 23], Bragg gratings [24] and photonic nanowires [25] were used. Nevertheless, due to directionality of the emitted photon, reflection at the high refractive index boundary, very high numerical aperture (NA) of the output mode, and loss in the optical components, overall collection efficiency at the SMF is very low compared to the theoretical limit. In this work we investigate a complete scheme for high efficiency light coupling from an InP/InAsP quantum dot nanowire to a single mode fiber.

1.3 Solid state optical power limiter integrated with optical filter

Extremely sensitive photonic devices are often used in quantum optics application for detection and manipulation of signals with very low power. Excess incident power can cause malfunction or even damage these sensitive devices. In some special cases, intentional excess power can possibly be used to hack quantum key distribution (QKD) system [3, 4] by damaging the photo detectors (referred to as the 'blinding' attack).

Intentional or unintentional, it is an inherent necessity to protect sensitive devices from excess input signal. Analogous to the current limiter in electronics, optical power limiter (OPL) is getting more and more attention in different areas of photonics. Of particular interest for us was the use of the power limiter as a tool to prevent the so called 'blinding' attacks in a QKD system. Different schemes have been demonstrated for optical power limiting including use of third-order nonlinear material as a cavity layer in Bragg mirror cavity [26–28], cavities with phase-changing materials [29, 30], exploiting intensity induced thermal effect in silicon photonic crystal cavity [31] or in silicon micro-ring resonator [32].

The basic idea behind nonlinear cavity OPL or thermally induced size change OPL is the shift of resonance peak (usually red shift) with the increased intensity of the incoming light. In most cases, these devices should work fine to act as an optical limiter, however, there might be some instances where someone might maliciously intend to exploit the loophole in the limiting performance of the OPL. One way this can be done is to slightly red detune the pump signal which will cause the red shift of the resonance peak and slowly increase the wavelength at the same rate of the device's cavity resonance. At the same time, send another probe signal at the cavity resonance wavelength with high enough intensity to sabotage the device protected by the OPL. In this work we try to address the issue by proposing an OPL integrated with an optical filter that can limit the input light power without any loophole.

1.4 High efficiency SNSPDs evanescently coupled to DLW waveguides

When high energy femtosecond laser pulses are focused inside a glass substrate, the refractive index of the focal volume changes. By moving the beam focus, waveguides can be made inside the substrate [33]. These waveguides have good mode matching with optical fibers which can be used to increase the efficiency of light coupling from the external source to the chip. Different kinds of passive devices, such as power splitters, directional couplers, interferometers, Bragg gratings, waveguides and waveguide lattices, as well as active devices, such as waveguide amplifiers or lasers, can be made using direct laser writing (DLW) [34]. Additionally, the capability to write 2D and 3D photonic lattices inside glass substrate make it more robust for fabricating on-chip integrated photonic devices and offers a promising platform for on-chip analogue quantum simulator. In this work, we explore the integration of superconducting nanowire single photon detectors (SNSPDs) with DLW waveguides with the goal of making this platform fully on-chip.

1.5 Outline of thesis

The thesis contains six chapters including the introduction and conclusion. Chapter 2 presents the motivation, design, fabrication and experimental result for on-chip splicer for coupling light between photonic-crystal and solid-core fibers. It also include some potential applications using the on-chip splicer for enhancing the coupling efficiency between different fibers. Chapter 3 includes the motivation and design proposal for high efficiency fiber-coupled single-photon source based on quantum dot embedded in a semiconductor nanowire. We also report the fabrication progress for experimental realization. Chapter 4 includes the motivation and design for a solid state optical power limiter integrated with an optical filter, mainly intended for preventing the 'blinding' attack on a QKD system. It also presents the

fabrication outlook for realizing in-plane and out-of-plane structures for the proposed structure. Chapter 5 presents the motivation and design for high efficiency SNSPDs evanescently coupled to DLW waveguides. We also report the fabrication progress for experimental realization. The thesis concludes with Chapter 6, in which a summary of the work done is given and the possible future directions are discussed.

Chapter 2

On-chip Splicer for Coupling Light between Photonic-Crystal and Solid-Core Fibers

2.1 Introduction

Hollow-core photonic-crystal fibers (HCPCFs) offer a promising platform for implementing light-matter interactions at low optical powers by allowing simultaneous tight confinement of both photons and atoms. However, interfacing HCPCFs with conventional solid-core (SC) fibers presents a unique set of challenges. While electric-arc fusion splicing between HCPCF and SC fiber is commonly performed with off-the-shelf splicers, significant losses in the joint region are inevitable due to partial melting and deformation of the photonic crystal during the splicing process. Several techniques have been employed to reduce the splice loss between solid-core and hollow core fibers including the use of a CO_2 laser (1.3 - 2.8 dB loss [9]), graded index fiber (0.6 dB loss [10]), offset electrode arc discharge (1.5 - 2 dB loss [11]), repeated arc discharges on the joint (1.5 - 2 dB loss [12]), overlap between fibers (1.4 dB loss [13]), and N_2 pressure to prevent hole collapse (1.05 dB loss [14]).

In general, the main causes of loss in a fiber joint arise from the mode field area (MFA) mismatch between the two fibers, vertical or horizontal misalignment, angular misalignment, as well as the reflection from the air-glass interface and the deformation of the fiber structure in the joint region when HCPCFs are joined with solid-core fibers. While the MFA mismatch puts essentially a fundamental lower limit on the loss in the fiber joint, the other losses depend on the technique used to join the fibers. Mechanical splicing avoids losses caused by the fiber deformation, but requires careful alignment [15]. One way to achieve a precise alignment between two fiber ends is to use optical lithography to form on-chip structures, such as etched V-grooves in silicon [16] and fiber clamping structures [17] formed by undercut in thick photoresist. The latter in particular provides an excellent mechanical stability and has been successfully used to align high-finesse optical cavities formed between two fiber faces in ultra-high vacuum (UHV) environment [17]. Here, we apply this alignment method to implement a mechanical splicer for HCPCFs and present a modification to the structure that enables sub-micron precision alignment and splicing for fibers with different cladding diameters, such as a commercially available 130 µm diameter HCPCF and a 125 µm diameter single-mode fiber (SMF).

2.2 Design

Guiding and holding of optical fibers with an undercut resist structure requires slanted walls with height greater than the radii of the fibers as depicted in Figure 2.1. In general, the optical fibers have a cladding diameter of ∼125 µm, so a clamping structure with walls of ∼90 µm height is a reasonable choice. Though conventional photoresists yield micron range coating thickness, some photoresists like SU-8 or AZ series are capable of providing 100 µm thickness. Depending on the exposure dose and proximity gap (gap between wafer and photomask), oblique sidewalls with varying undercut angles are attainable [35]. To facilitate different diameter fibers having same optical axis, half of the chip is etched with the etch depth determined by the difference in radii of the fibers. Two photomasks are needed to complete the lithography process: the first one is for etching the chip to accommodate the difference in diameters of the two fibers being aligned and the second one is for making the actual clamping structure. Designing the first mask with rectangles (as shown in Figure 2.3) is straightforward, but to design the second photomask, care has to be taken as the target is to precisely control the angles of the sidewalls and the gap between them. For the second photomask, the width of the channel feature as a function of photoresist height, fiber diameter and undercut angle, as illustrated in Figure 2.1a, can be found from trigonometric calculations:

$$w = \sqrt{\left(\frac{2h-d}{\cos\theta} - d\tan\theta\right)^2 + 4h(d-h)} \tag{2.1}$$

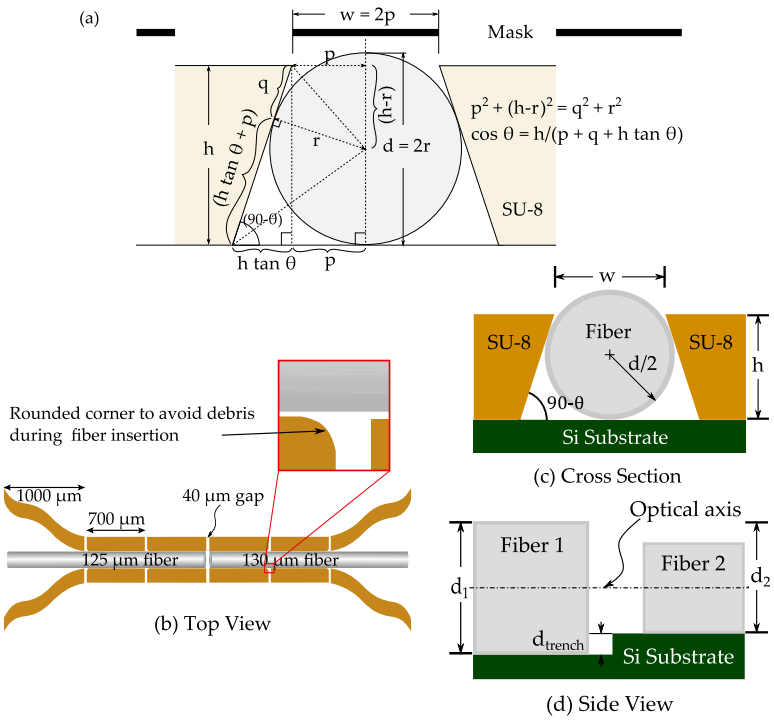

FIGURE 2.1: Fiber alignment structure (a) geometry of the clamping structure design; (b) top view; (c) cross section and (d) side view: different diameter fibers vertically aligned to have the same optical axis.

Note that since the undercut angle and resist thickness will be the same for a particular fabrication run, it is the channel width that is adjusted on each side of the clamping structure for the two fibers being aligned. For example, to align a 125 µm diameter fiber with a 130 µm diameter fiber using a 90 µm thick photoresist with 10° undercut, we use a 117 µm mask channel on one side of the splicer and 123 µm channel on the other side of the splicer (Figure 2.2). A funnel shaped opening was designed to guide the fiber during insertion. The long sidewalls were split into segments with gaps ≈4-5% of the segment lengths to reduce stress from thermal expansion of the photoresist as the dimensional change of the SU-8 resist is < 2.5% for up to 350°C [36]. Additionally, the inner corners of the sidewall segments were rounded to minimize debris formation at the tip of the fibers during insertion.

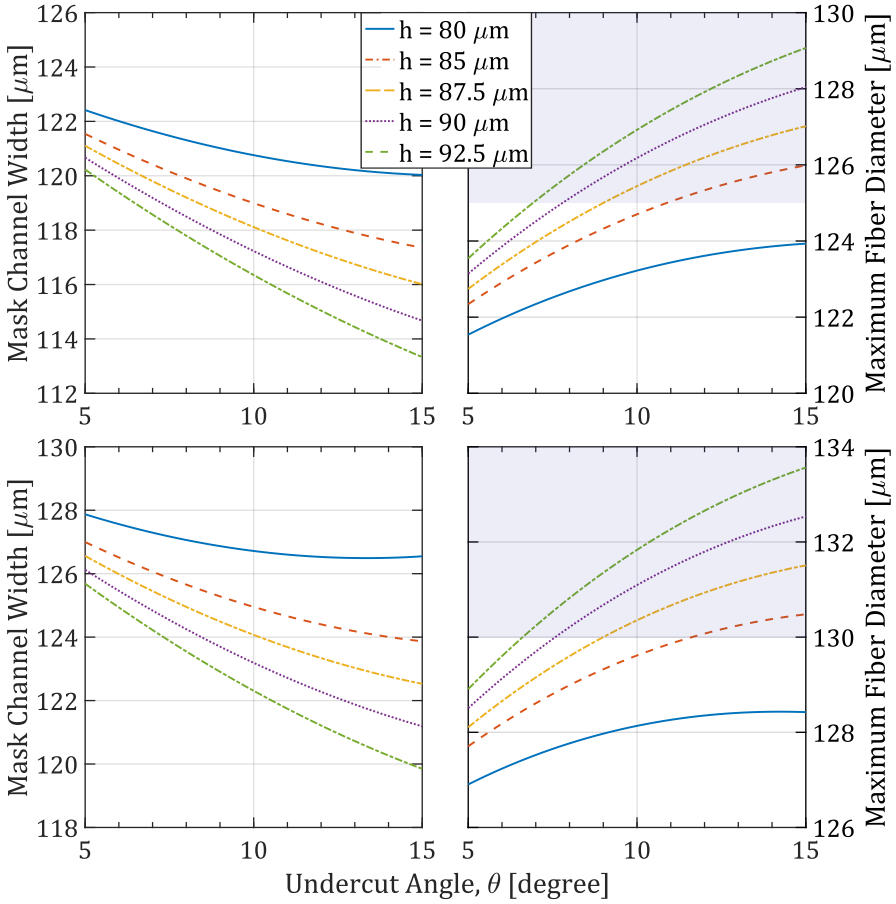

FIGURE 2.2: (Top left) Photomask channel width needed for a 125 µm diameter fiber as a function of undercut angle (θ) and height (h) of the SU-8 structure (from equation 2.1). The target width was selected at $\theta = 10°$ and h = 90 µm. (Top right) Maximum fiber diameter that can be accommodated with the selected channel width by adjusting the wall angle and resist thickness. The shaded region shows the values needed for a 125 µm diameter fiber. (Bottom) Similar calculation shown for 130 µm diameter fiber.

2.3 Fabrication

Optimizing the process to get alignment structures having consistent undercuts was the main challenge in fabrication. Exact width and predictable undercut in the guiding channel is necessary for easy insertion and holding of the optical fibers. Fabrication of the on-chip fiber splicer consists of two parts: the first one is to etch the Si chip to accommodate different diameters fibers and in the second step, a clamping structure is made of photoresist to guide and hold the fibers on the chip. The details of the fabrication process is described in the following sections and depicted in Figure 2.3.

2.3.1 Si wafer etching

Starting with a 4" Si wafer, standard solvent cleaning (5 min. in acetone, 5 min. in IPA and 2 min. DI water rinse) and O_2 plasma cleaning (RF power 1000 W, pressure 300 mTorr, temperature 180°C, O_2 flow rate 50 sccm) for 2 min. was done followed by an HMDS coating for better adhesion to the photoresist. In the next step, a negative tone photoresist, ma-N 1410, was spun at 3000 rpm for 1 min. with 500 rpm/s acceleration and baked at 110°C for 90 sec. for a target thickness of ∼1 µm. Then the wafer was exposed with 365 nm UV light at a dose of 350 mJ/cm^2 and developed with ma-D 533/S for 2 min. followed by a DI water rinse. Now the wafer has windows where the silicon is exposed. The wafer was then loaded in a Oxford inductively coupled plasma etching tool (Oxford ICP380) for etching the silicon using a Bosch process. The etch depth depends on the difference in radius between the hollow core fiber and the solid core single mode fiber, which is ∼2.5 µm in this case. Etching was done for 5 cycles as the etch rate was measured to be ∼0.5 µm/cycle. Then the wafer was dipped into Remover PG for 5 min. followed by a standard solvent cleaning and O_2 plasma cleaning to remove the ma-N 1410 resist. To measure the etch depth, a Dektak 150 surface profiler was used. In Figure 2.4, an SEM image and measured height profile after the Bosch process is given.

2.3.2 SU-8 alignment structure formation

Si wafer with etched windows was dehydrated for 1 hour at 200°C immediately before dispensing SU-8. After applying the SU-8, the wafer was spun at 500 rpm for 20 s at 100 rpm/s acceleration to spread the resist evenly and then it was spun at 2000 rpm for 20 s at 300 rpm/s acceleration for a uniform coating. The soft baking was done in 2 steps: the wafer was first baked at 65°C for 10 min. and then ramped for 6 min. to reach 95°C where it was kept for 2 hours.

After baking and bringing the wafer at room temperature, the wafer was exposed with UV light at a dose of 275 mJ/cm^2 with 150 µm proximity gap. The dose and proximity gap was optimized to obtain undercut at the sidewalls so that the fibers do not move upward after coupling. In general, photolithographic structures are made with vertical sidewalls to avoid unwanted effects. However, here we exploited the non-ideal behavior of the photoresist in our favor. Following the exposure, a 2-step post expose bake (PEB) was performed to selectively cross-link the exposed portions of the film. The exposed wafer was baked at 65°C for 1 min. and then at 95°C for 10 min. In the subsequent step, the wafer was developed with SU-8 developer for 30 min. along with a magnetic stirrer for faster developing. The developer was changed after 15 min. as the rate was slowing significantly. In the next step, a profilometer was used to make a wafer map to measure the SU-8 structure height as shown

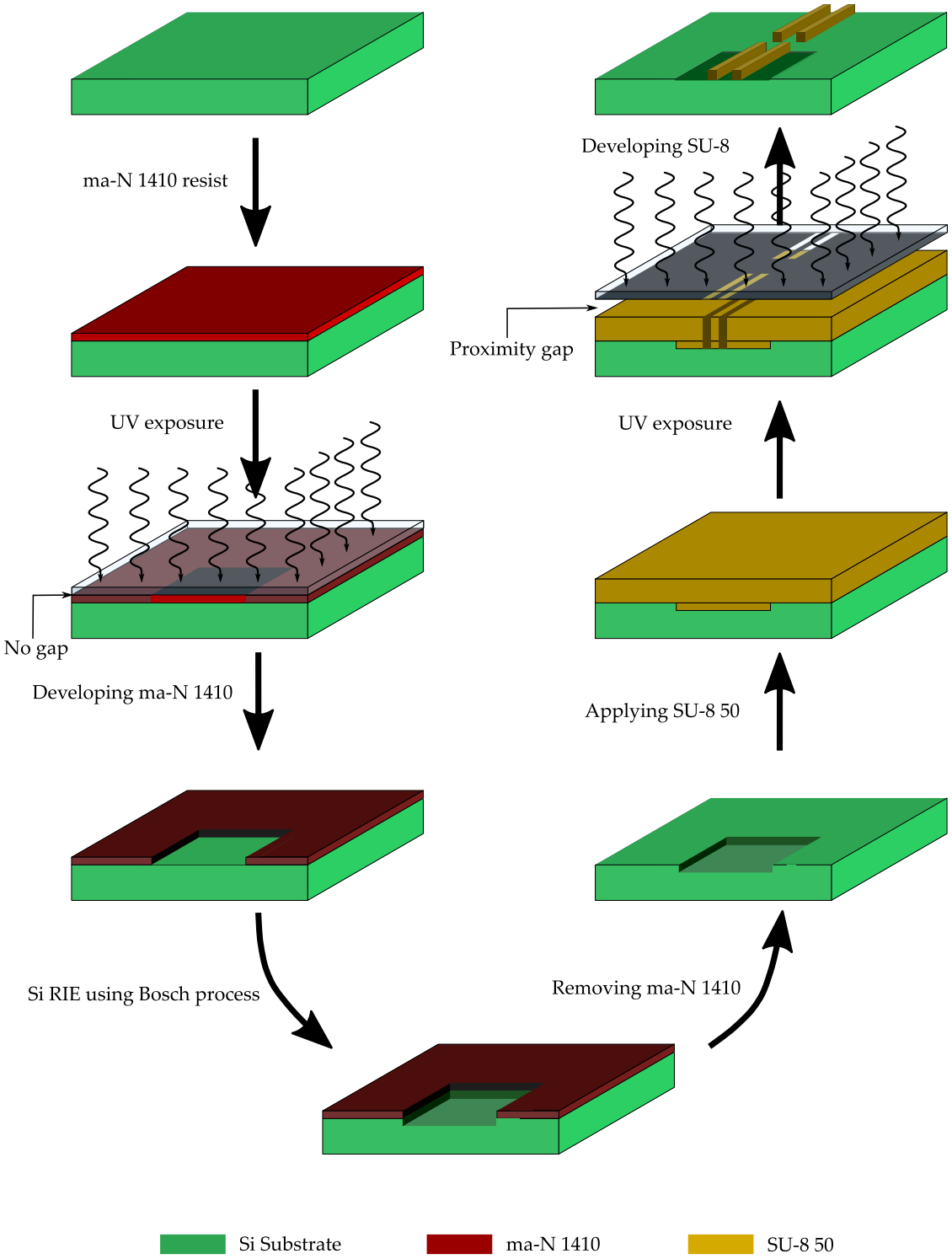

FIGURE 2.3: Fabrication process flow for on-chip fiber splicer.

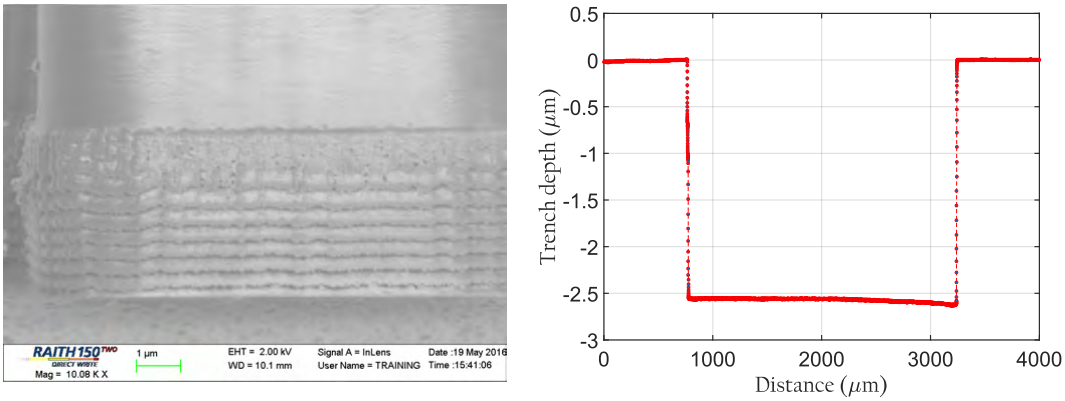

(a) (b)

FIGURE 2.4: (a) SEM image after silicon Bosch etch. The steps are result of multiple etch cycles. (b) Measured silicon etch profile for 2.5 µm etch.

in Figure 2.5. The SU-8 alignment structures were ∼85 µm except near the edge of the wafer, where the height was measured to be >100 µm due to the edge bead effect during spinning of the resist. Following the measurement, the wafer was diced and individual chips were isolated. In Figure 2.6, microscope images of a chip with and without the fibers inserted are depicted.

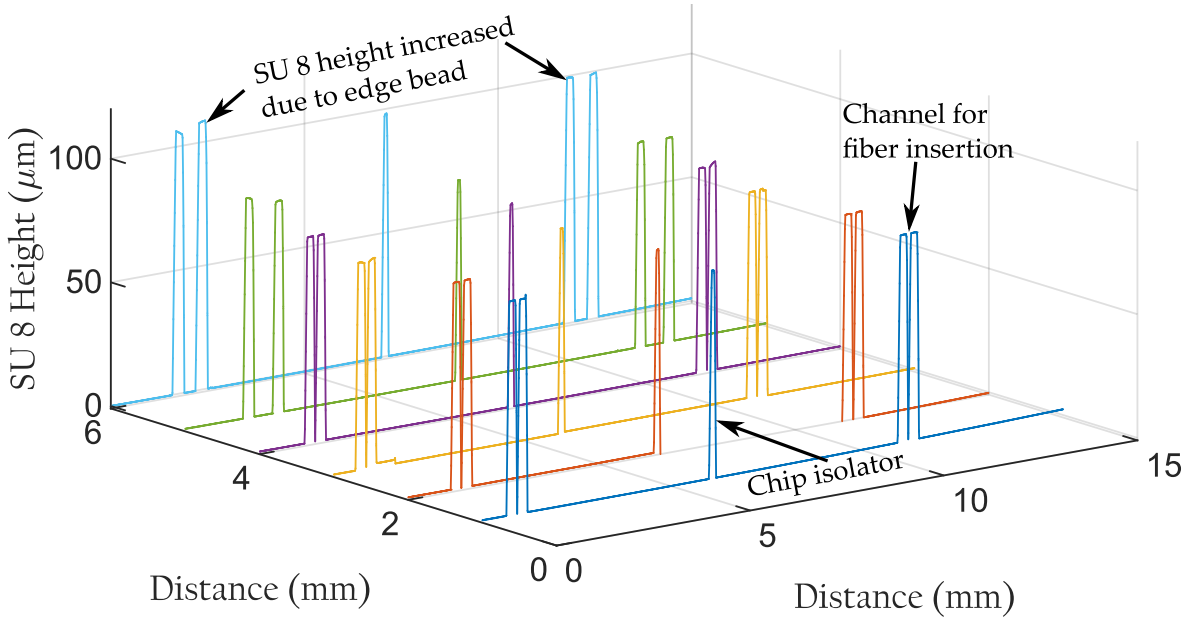

FIGURE 2.5: SU-8 alignment structure height profile on the wafer measured by Dektak 150 surface profiler. The structures are ∼85 µm high except at the edge of the wafer. Chip isolators were used (∼50 µm pre-cut in dicing saw) to isolate the chips and help dicing.

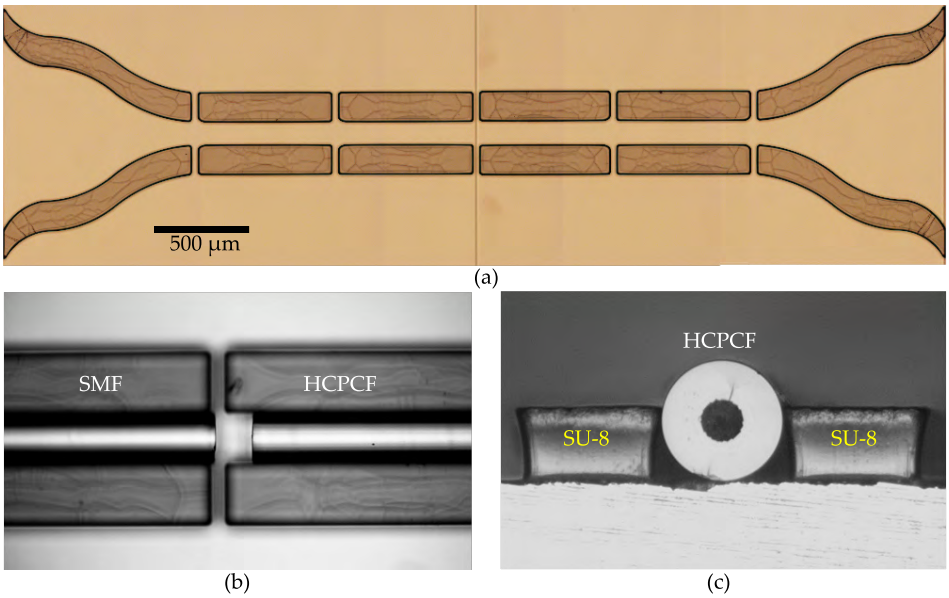

FIGURE 2.6: Microscope image of the on-chip fiber splicer. (a) top view of the chip. (b) top view of the chip with a conventional single mode fiber and a hollow core photonic-crystal fiber inserted from two sides. (c) cross section of a chip with a hollow core photonic-crystal fiber inserted. The undercuts along the side walls are holding the fiber nicely so that it doesn't move.

2.4 Experimental Results

2.4.1 Coupling Characterization Setup

The performance of the produced mechanical on-chip fiber splicer was assessed by measuring the coupling efficiency for an assortment of fibers using the setup illustrated in Figure 2.7. A Ti:Sapphire laser system was used to generate 852 nm laser and the light was coupled to a 1 m section of PM780HP solid-core SMF through a beam splitter. Powers in both arms of the beam splitter were measured and the power splitting ratio was determined. The fiber was then joined with a 1 m long section of HC800B hollow-core PCF using the fiber splicer chip and powers were measured after the hollow-core fiber (PD-2) and the beam splitter (PD-1). Knowing the power splitting ratio at the beam splitter, coupling efficiency from the SMF to the HCPCF was determined. The hollow-core fiber and its splicer chip were then replaced with an assortment of solid-core single-mode and multimode fibers that would be joined with the PM780HP with an appropriate splicer chip and the measurement procedure was repeated. Finally, the PM780HP fiber was replaced by a roughly 1 m long section of HC800B fiber and the coupling efficiencies from the hollow-core PCF to solid-core single-mode, multimode, and to another hollow-core PCF were measured in a similar fashion. For the SMFs and the HCPCF, we assumed that 1 m is long enough for light not coupled into the fundamental mode to get sufficiently attenuated.

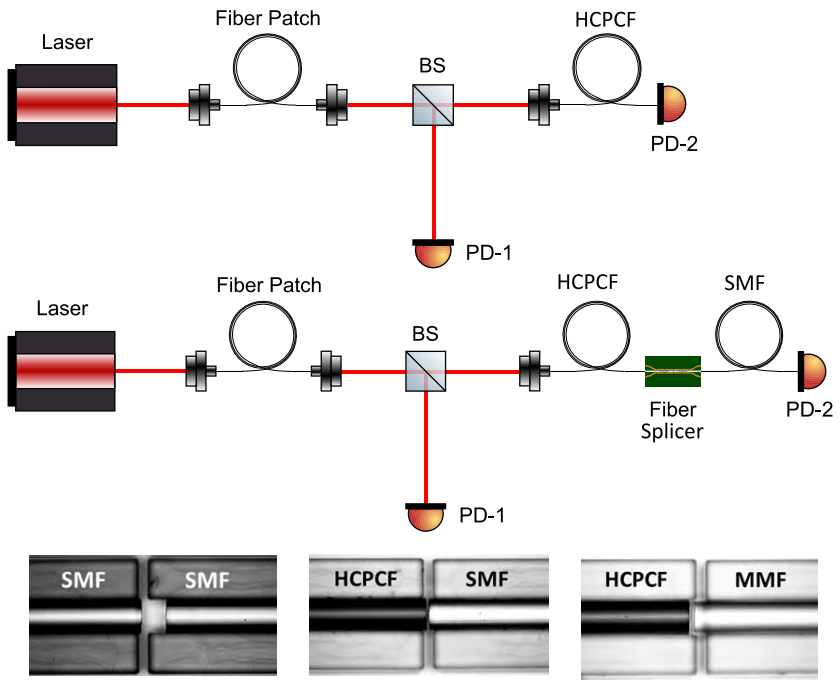

FIGURE 2.7: Experimental setup for on-chip fiber splicer efficiency measurement. (top) setup used to determine the power at the HCPCF output. (middle) setup used to determine the coupling efficiency. (bottom) microscope snapshot taken during different measurements.

2.5 Measurement and Analysis

Fibers were inserted from both sides of the on-chip splicer, butt coupled, and then coupling efficiency was measured. After that, the distance between fiber faces was increased in steps and the coupling efficiencies and the gaps were measured. Each measurement consists of an average of 60,000 data points taken over a 60 s time period and is shown in Figure 2.9 as red circles. The distance was increased until the power coupled to the second fiber became almost zero. Measured coupling efficiencies were compared with an approximate theoretical model assuming the mode field distribution has a Gaussian shape. Although the guided modes in SMF or HCPCF are not completely Gaussian, the approximation seems good enough for this calculation. The approximate theoretical model used to calculate the expected coupling efficiency is given in equation 2.2 [37] and a schematic is illustrated in Figure 2.8 for clarification.

$$\eta = \frac{4w_1^2 w_2^2}{\left(w_1^2 + w_2^2\right)^2 + \left[\frac{\lambda z_w}{\pi n_i}\right]^2} exp\left[- \frac{2w_1 w_2}{w_1^2 + w_2^2}\left(\frac{s^2}{w_1 w_2} + \frac{\theta^2}{\theta_{d1}\theta_{d2}}\right)\right] \tag{2.2}$$

Where, η = coupling efficiency, $w_{1,2}$ = spot size of the fibers, z_w = horizontal separation between fibers, n_i = refractive index of the material between the fibers, s = vertical misalignment of the optical axes, θ = angular misalignment, $\theta_{d1,d2} = \lambda/(\pi n_{1,2} w_{1,2})$ = divergence angle, and $n_{1,2}$ = core refractive index of the fibers.

Measurement results for solid-core single-mode fiber (PM780HP) to solid-core single-mode (780HP), solid-core multimode (GIF625) and hollow-core photonic crystal fiber (HC800B)

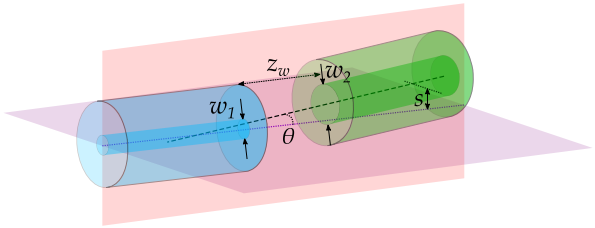

FIGURE 2.8: Fiber coupling schematic: two fibers are placed at distance z_w having vertical and angular misalignment between their optical axes s and θ, respectively.

coupling are illustrated in Figure 2.9. The blue dashed lines in Figure 2.9(a) are theoretically expected values obtained by using spot sizes from fiber datasheets and assuming zero vertical and angular misalignment, while the blue shaded region is obtained by taking the maximum and minimum expected values. The maximum butt coupling efficiency obtained for SMF to SMF coupling was 94%, SMF to MMF coupling was 90% and SMF to HCPCF was 90%. Approximately 6.8% loss was due to Fresnel reflection at the glass-air interface (∼3.4% per interface), assuming $n_{glass} = 1.45$, which can be improved by depositing anti-reflection coating onto the tip of the solid-core fibers or by adding a drop of index-matching liquid between the fiber tips. Slightly higher measured value for SMF (PM780HP) to SMF (PM780HP) coupling can be caused by etalon effect from fiber faces or from measurement error. Expected values for the single-mode to multimode fiber were not calculated which is not crucial for this work. The measured efficiencies for SMF to HCPCF is higher than the expected values after a certain gap between fiber faces mainly due to the fact that the HCPCF is not a true single-mode fiber, but it can support several higher order modes in the core region, and in some cases, additional surface modes can be located at the core cladding photonic crystal interface [38].

Similar measurement results for hollow-core photonic crystal fiber to solid-core single-mode and multimode fibers are presented in Figure 2.10. The maximum observed butt coupling efficiency from HCPCF to SMF was 80%, to MMF was 93% and to HCPCF was 70%. This reduced coupling efficiency was likely due to (i) imperfect cleaving of the fibers, as depicted in the inset of Figure 2.10(a), and (ii) some of the light coupled into the HCPCF going into non-fundamental modes that do not get fully attenuated after 1 m. The non-reciprocal coupling efficiency between SMF (PM780HP) and HCPCF (HC800B) arises from the multimodal nature of the HCPCF, which is consistent with other reported results [11, 13]. Coupling light to and from the HCPCF is also dependent on the orientation of the hollow core fiber, which we attribute to the HCPCF's higher-order modes not being axially symmetric [9–11]. Though the traditional fiber cleaving tools are not optimized for perfect cleaving (cleaved fiber face is perpendicular to optical axis), careful cleaving can improve the quality. However, HCPCF was more prone to imperfect cleaving compared to SMFs during the experiment. For the theoretical expected value calculation, this angular misalignment was considered in equation 2.2. To calculate the loss contribution from the fiber splicing, losses due to MFA mismatch and Fresnel reflection are subtracted from the overall measured loss:

$$Loss_{splice} = Loss_{measured} - \left| 10 \log \left[\frac{4 w_1^2 w_2^2}{\left(w_1^2 + w_2^2\right)^2} \times \left(1 - R\right)^n \right] \right| \tag{2.3}$$

Where, R = Fresnel reflection at air-glass interface and n = number of air-glass interfaces.

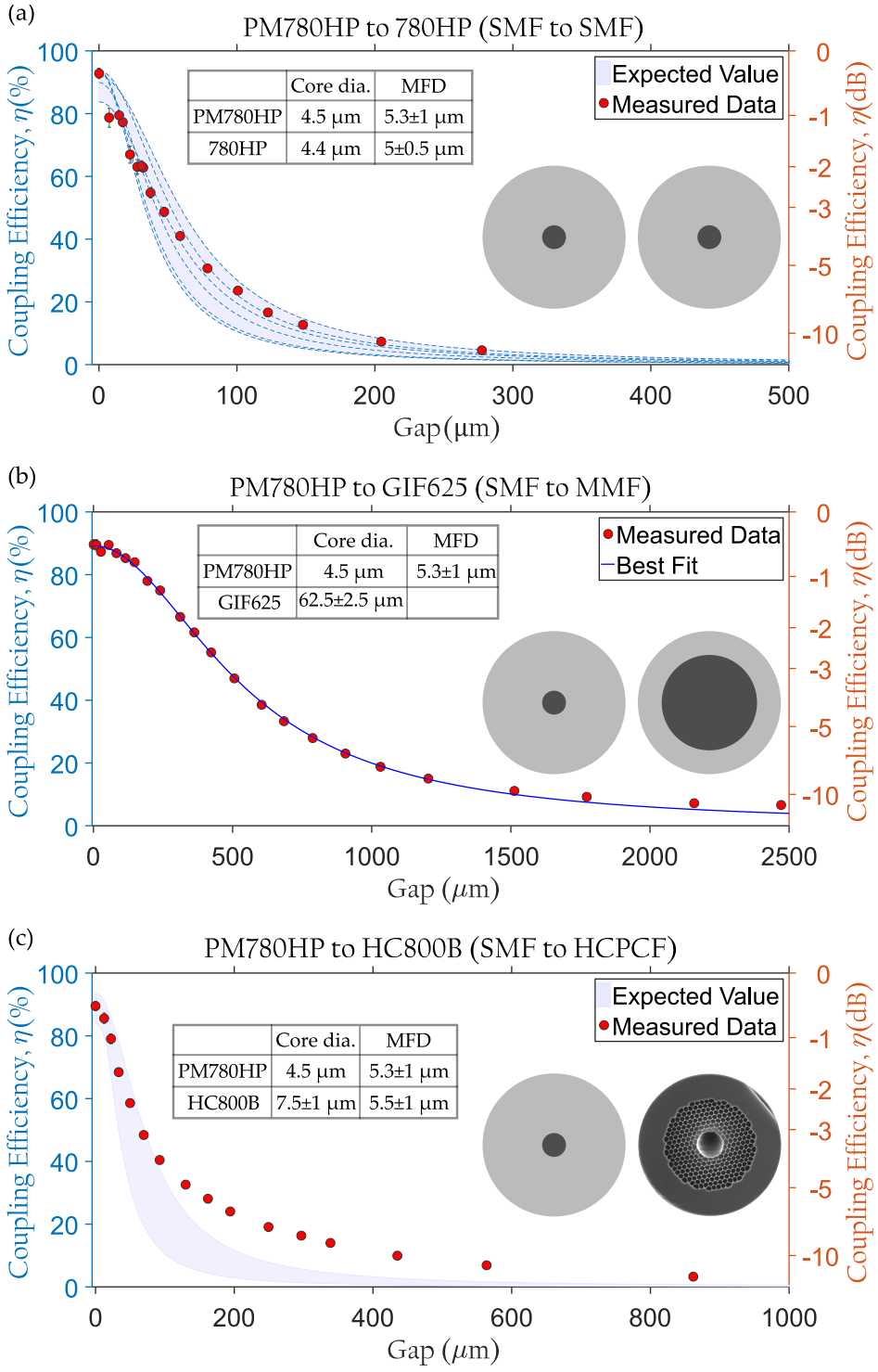

FIGURE 2.9: Coupling efficiency measurement results for SMF to SMF, MMF and HCPCF. Core diameter and mode field diameter (MFD) from the datasheet of the fibers are shown in the table. Each red circle with error bar (most of them are very small) is a measured value averaged over 60,000 samples.

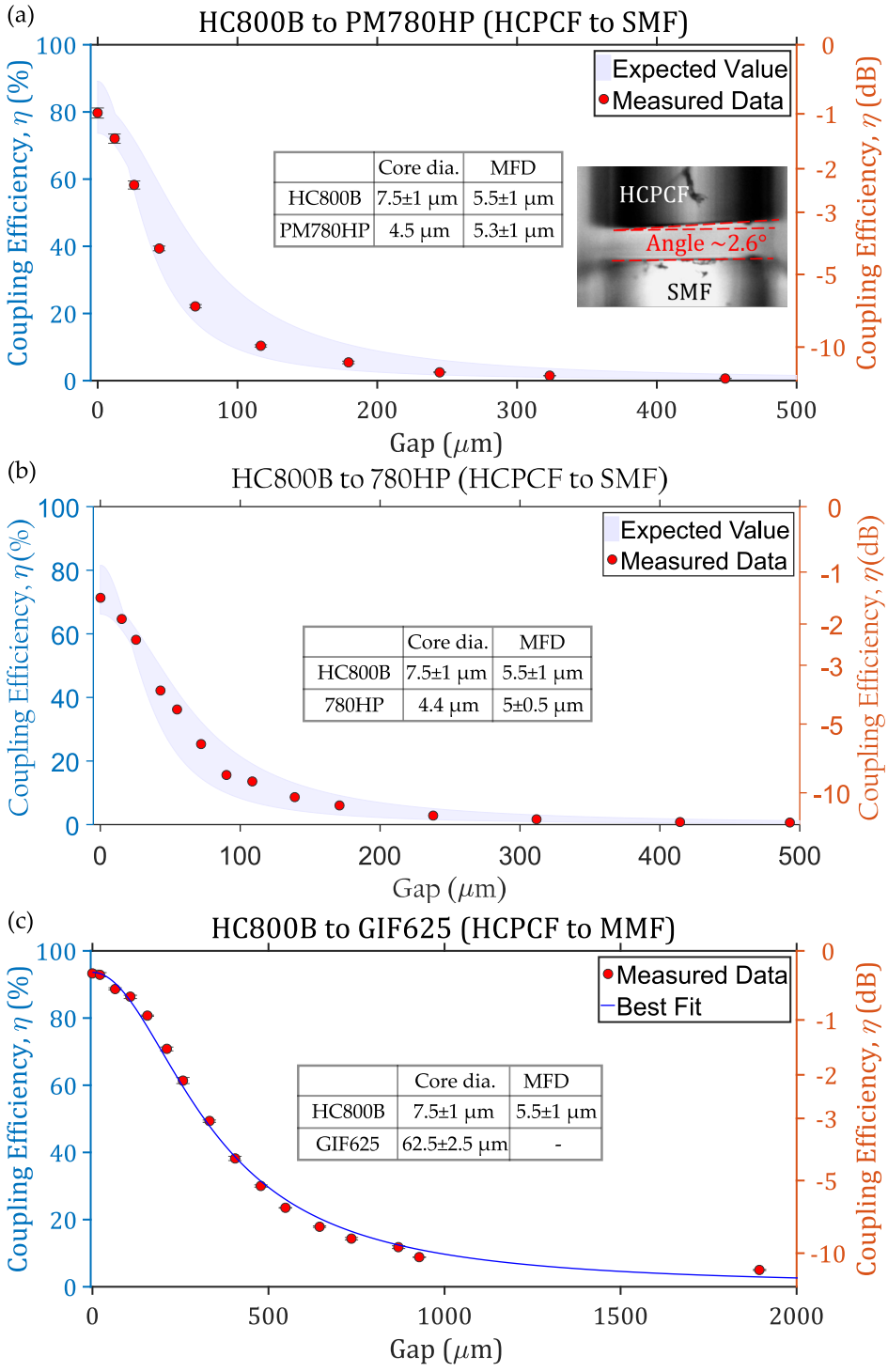

FIGURE 2.10: Coupling efficiency measurement results for HCPCF to SMF and MMF. Inset shows the imperfection in cleaving the hollow-core fiber that results in lower coupling efficiency.

The measurement results are illustrated in Figure 2.11 and summarized in Table 2.1. The coupling efficiencies from solid core single mode fiber to other fibers are >90%, where ~3.4% loss (per interface) is accounted for by Fresnel reflection due to the air-glass interface. The efficiencies for SC to SC fiber coupling was achieved as high as ~100% with the addition of index matching liquid at the joint region. The coupling efficiencies from hollow core fiber to solid core single mode fibers are ~70-80%, which can be improved by better cleaving of the HCPCF and adding anti-reflection coating at the solid core fiber face.

TABLE 2.1: Measured butt coupling efficiency (η) & loss in the fiber joint
Splice loss includes losses other than MFA mismatch and interface reflection.

		SM800	780HP	PM780HP	GIF625	HC800B
PM780HP	η	93%	93%	94%*	90%	90%
	Total loss	0.32 dB	0.32 dB	0.27 dB	0.46 dB	0.46 dB
	Splice loss	0.01 dB	0.009 dB	*	0.17 dB	0.31 dB
HC800B	η	-	71%	80%	93%	70%
	Total loss	-	1.49 dB	0.97 dB	0.32 dB	1.55 dB
	Splice loss	-	1.3 dB	0.82 dB	0.17 dB	1.5 dB

*Efficiency is slightly higher than the expected value.

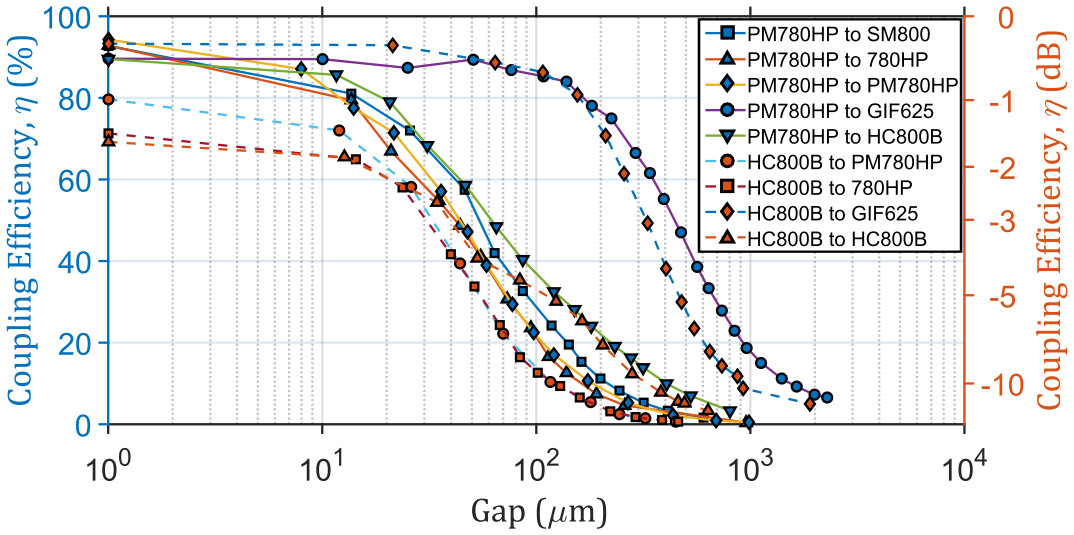

FIGURE 2.11: Coupling efficiency measurement summary.

2.6 Application: Coupling light between SMF and HCPCF containing cold atomic ensemble

HCPCFs offer a unique platform for studies of light-matter interactions, quantum, and nonlinear optics, and effective photon-photon interactions mediated by cold atomic ensembles. The skeleton of the experimental setup used in our lab is: laser-cooled cesium atoms are loaded into a vertically placed hollow core photonic band gap fiber using gravitational force, and pump and probe signals are used to do desired quantum optics experiment (as depicted in Figure 2.12(top) from [39]). The optical signals are coupled to the hollow-core fiber using free space optics and typical coupling efficiency achieved in our lab is ∼40%. This efficiency can be increased significantly by using direct coupling between HCPCF and SMF using the on-chip splicer. Also a monolithic coupling would be preferable as the current setup is sensitive to misalignment which can excite additional, undesired modes in the HCPCF and which affects the repeatability of the experiment.

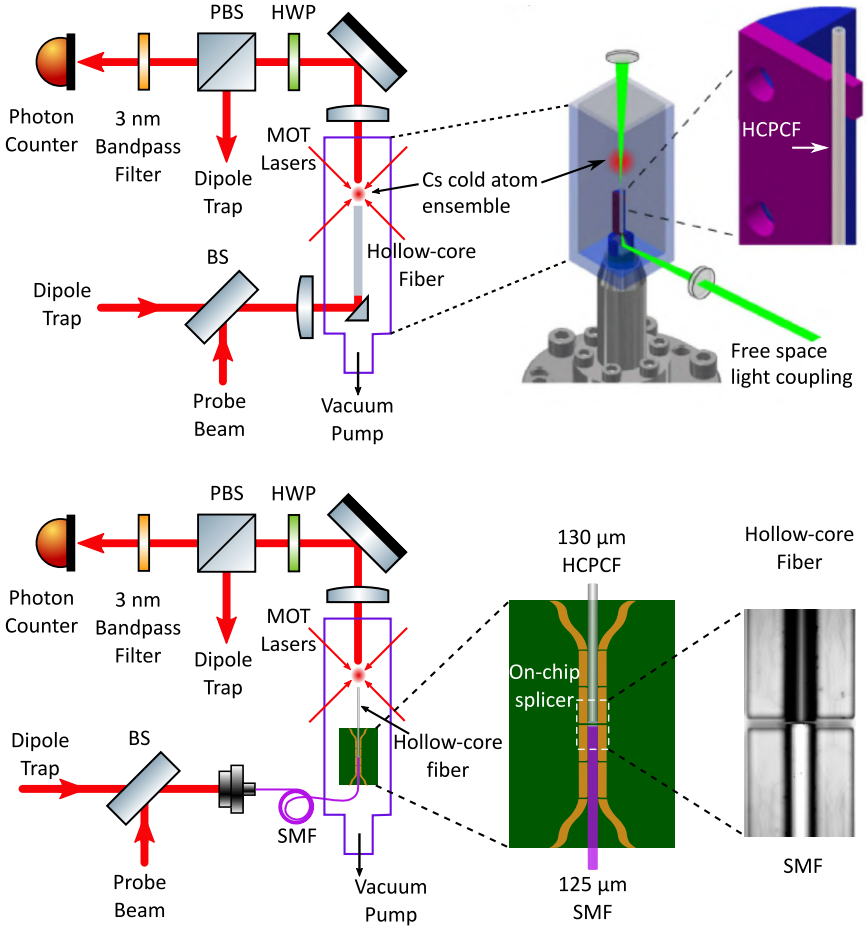

FIGURE 2.12: (top) Present experimental setup: the glass cell containing the magneto-optical trap and the hollow-core fiber (HCPCF) and a detail of the fiber mounting structure. Light is being coupled via free space coupling from top and bottom. (b) Proposed experimental setup: the HCPCF holder is replaced by the on-chip fiber splicer and light is being coupled to the HCPCF using a single mode fiber (SMF) from the bottom.

The schematic of the proposed modification of the existing setup with the fiber coupling is depicted in Figure 2.12 (bottom). A Cold atomic ensemble is loaded into hollow-core fiber from the top, the optical signal at the top is free space coupled and at the bottom is fiber coupled. The fiber interface is designed for efficient bidirectional coupling along with minimized Fresnel back reflection from air-glass interface in the case of input light from the hollow-core fiber to avoid standing waves in the hollow-core fiber. The optimization parameters are, θ = cleave angle at the solid-core fiber face and ϕ = rotation angle of the SMF (Figure 2.13).

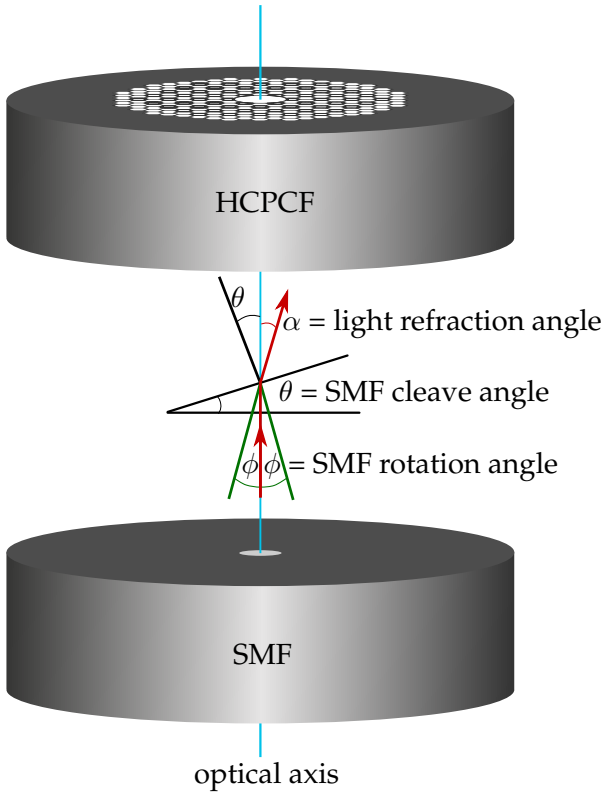

FIGURE 2.13: Schematic for coupling optimization between HCPCF and SMF.

Fresnel Reflection minimization

At the glass-air interface of the solid-core fiber, Fresnel reflection occurs due to refractive index mismatch. When input light guides through the solid-core fiber and if the fiber face is cleaved perpendicularly ($\theta = 0$) to the propagation direction, the back reflection is again guided into the fiber but in the opposite direction. The back reflection can be minimized by cleaving the fiber face at an angle which causes the reflection outside of the acceptance angle of the fiber. However, the angle cleave also causes the outgoing light to exit at an angle (α) with the optical axis. When the outgoing light from solid-core fiber enters to the hollow-core fiber, there is negligible Fresnel reflection as the effective index of propagation in the hollow-core fiber is ≈ 1. Lumerical FDTD simulation results for Fresnel back reflection and α vs θ are depicted in Figure 2.14 (a-b).

For the case that the input light comes from hollow-core fiber and is being coupled to

solid-core fiber, Fresnel reflection from the solid-core fiber face may guide back to the hollow-core fiber and can cause an unwanted standing wave. However, angle cleaved solid-core fiber face can reflect the light outside of the acceptance angle of the hollow-core fiber. To investigate the phenomena, simulation result for reflected guided light in the hollow-core fiber as a function of solid-core fiber cleave angle and gap between the fiber faces is depicted in Figure 2.14 (c).

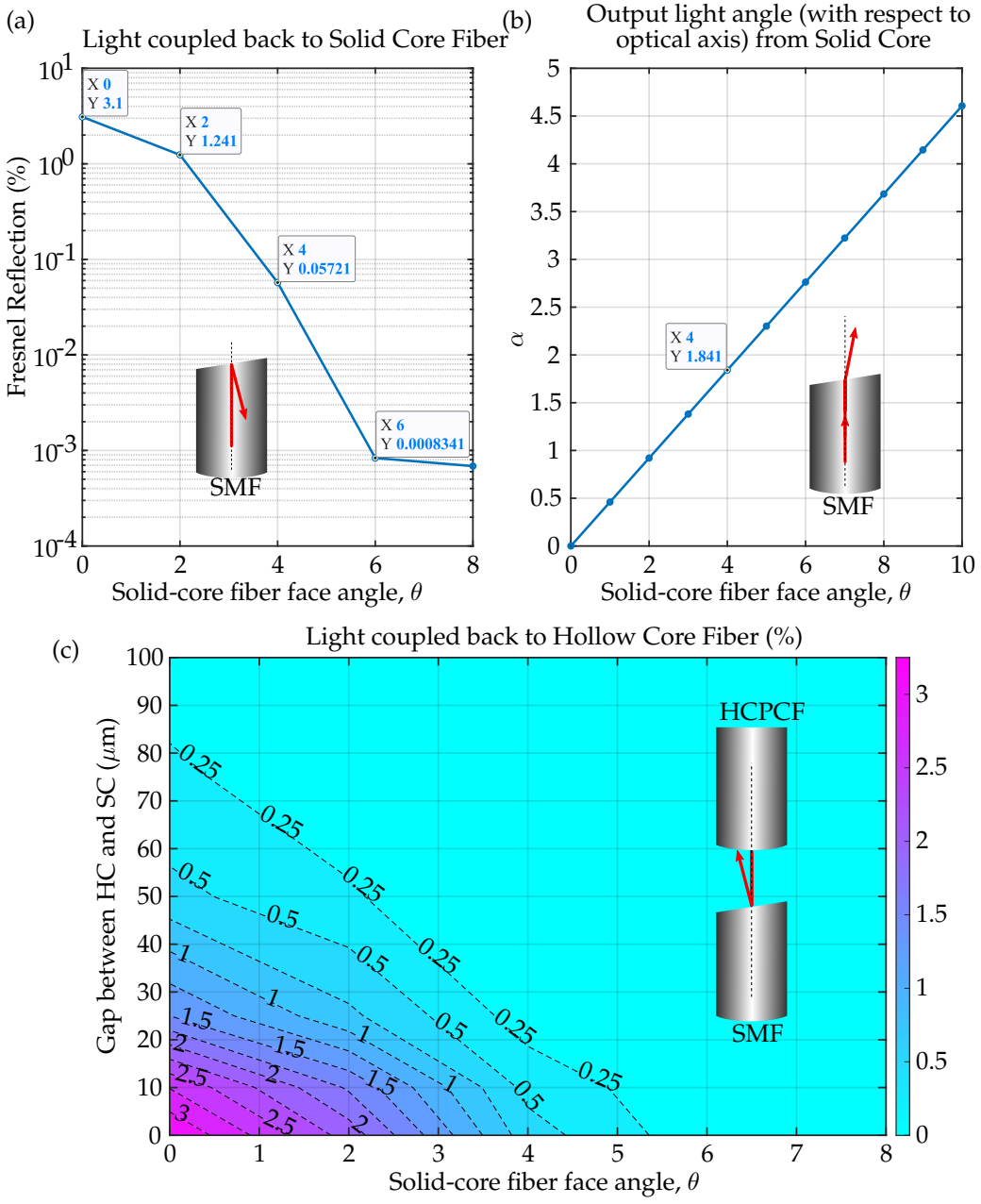

FIGURE 2.14: Fresnel back reflection (a) and outgoing refracted light angle α (b) vs solid-core fiber cleave angle θ using Lumerical simulation. (c) Reflected guided light in the hollow-core fiber as a function of solid-core cleave angle θ and gap between the fiber faces.

Coupling between fibers

The coupling efficiency (η) between two fibers depends on mode-field diameters, optical axis alignment, fiber cleave angle and distance between fibers. In general, butt coupling yields maximum coupling of light. However, for this application, an additional goal is to minimize the Fresnel reflection to avoid an unwanted standing wave inside the hollow-core fiber. Therefore an optimization needs to be done to get moderately high coupling efficiency along with minimum back reflection. As discussed in the previous section, this can be achieved by cleaving the SMF at a certain angle (θ) or rotating the SMF axis at an angle relative to the hollow-core fiber axis (ϕ) or a combination of both. To investigate the effect of θ and/or ϕ on the coupling efficiency between hollow-core and solid-core fiber, Lumerical FDTD simulation is done and the result is depicted in Figure 2.15. In Figure 2.15 (a), hollow-core to solid-core fiber coupling efficiency as a function of distance between fibers is

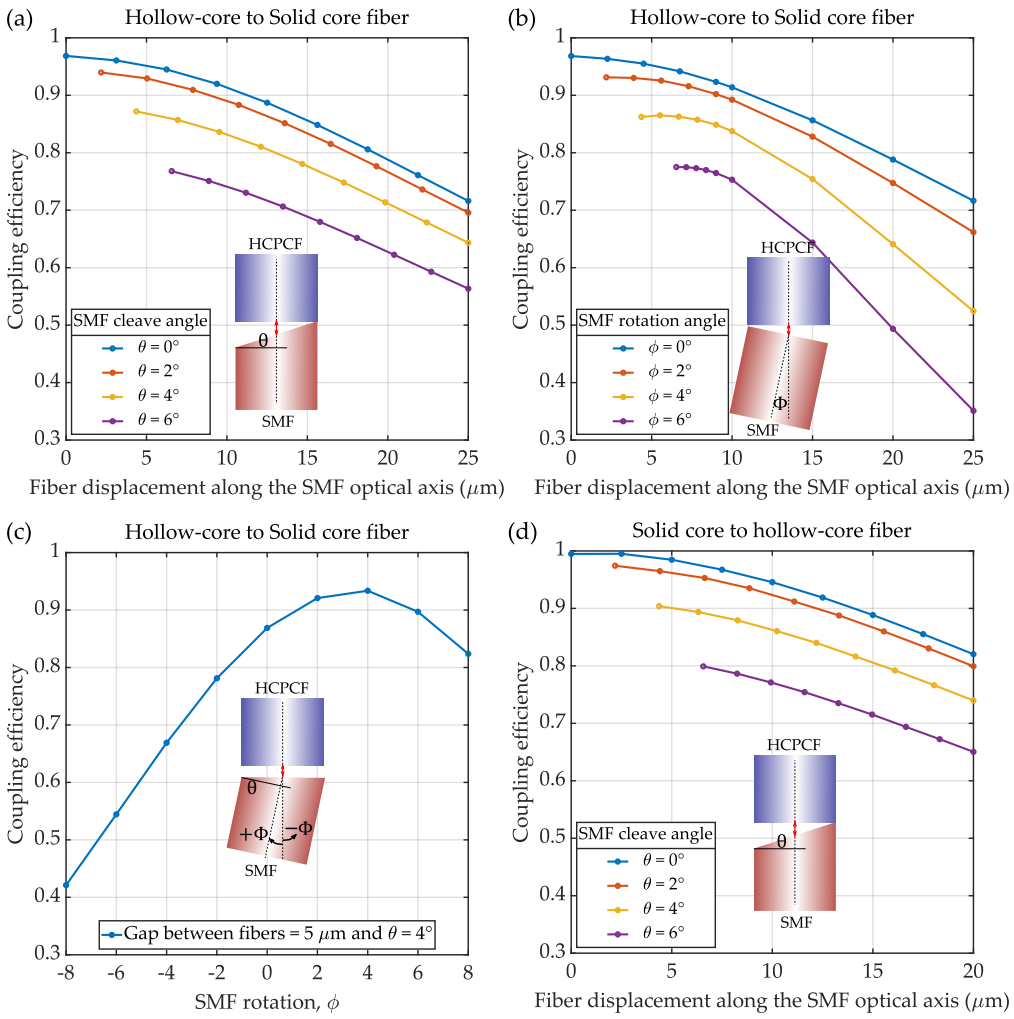

FIGURE 2.15: (a,b) Hollow-core to solid-core fiber coupling efficiency as a function of distance between fibers for different values of θ and ϕ respectively. (c) A combined effect of θ and ϕ for a fixed value of $\theta = 4°$ and variable ϕ. (d) Solid-core to hollow-core fiber coupling efficiency as a function of distance between fibers for different values of θ. The efficiency is ≈3.3% higher compared to (a) because of no Fresnel reflection as $n_{eff} \approx 1$.

illustrated for different θ values. Maximum possible efficiency (>96%) can be achieved for $\theta = 0^\circ$ and distance = 0µm, and then it drops as the distance between fibers increases. For nonzero θ, the maximum efficiency is lower, e.g. $\approx$ 87% for $\theta = 4^\circ$, and it decreases with distance. It is worth mentioning that for $\theta > 0$, the minimum distance starts at a value >0, e.g. minimum distance = 4.4 µm for $\theta = 4^\circ$, because of the angled cleave of the fiber face as illustrated in the inset. Similar simulation is done for hollow-core to SMF coupling efficiency as a function of SMF rotation. Though the maximum efficiency is similar for same angle, it drops quickly with distance compared to the previous scenario. This is because the optical axis is not aligned here unlike previous case. A combined effect of θ and ϕ is depicted in Figure 2.15 (c) for a fixed value of $\theta = 4^\circ$ and variable ϕ. The efficiency starts at $\approx$ 87% for no rotation and increases for positive rotation (clockwise) of the SMF. It reaches to the maximum for $\phi = 4^\circ$, however, at this point the two fiber faces are parallel and that abolishes the original goal to minimize the back reflection in the hollow-core fiber. On the other hand, for the negative rotation (counter clockwise) the efficiency drops significantly. Therefore, either an angled cleaved SMF or a flat cleaved SMF with rotation can be considered for this application but not both at the same time. Lastly, a simulation was done for the coupling efficiency from SMF to hollow-core fiber as a function of distance for different θ values (Figure 2.15 (d)). The efficiency plot is very similar to Figure 2.15 (a) except the efficiency is $\approx$3.3% higher as there is no Fresnel reflection from the hollow-core fiber face ($n_{eff} \approx 1$ as the core is air or vacuum). It is worth mentioning that the practical efficiency can vary depending on the fiber used, however, the analysis can be taken as a relative comparison among different scenarios as it investigates the geometric effects on coupling efficiency.

To summarize, a comparison is presented in Table 2.2 for different cases. A hollow-core fiber butt coupled to a flat faced solid-core fiber is taken as the reference point, and then the effect of θ and/or ϕ is depicted. Considering high coupling efficiency (87%) along with significant reduction of back reflection (>5 times improvement compared to the reference point) and less dependence on axial movement, solid-core fiber cleaved at $\theta = 4^\circ$ is a good choice for this application. The precise angle cleave can be achieved by using an automated glass processor.

TABLE 2.2: Hollow-core to solid-core fiber coupling efficiency and Fresnel reflection for different θ and ϕ.

	Gap	**Reference**	$\theta = 2^\circ$	$\theta = 4^\circ$	$\theta = 6^\circ$	$\phi = 2^\circ$	$\phi = 4^\circ$	$\phi = 6^\circ$	$\theta = 4^\circ$ at 0 µm	
η^*	0 µm	**96%**	94%	87%	77%	93%	86%	78%	$\phi = -4^\circ$	67%
	10 µm	**91%**	89%	83%	74%	89%	84%	75%	$\phi = 0^\circ$	87%
	20 µm	**79%**	77%	71%	63%	75%	64%	49%	$\phi = 4^\circ$	93%
Fresnel reflection to HCPCF at 0 gap		**3.3%**	2.1%	0.6%	0.08%	2.1%	0.6%	0.08%	$\phi = 8^\circ$	82%
Fresnel reflection to SMF at 0 gap		**3.3%**	1.2%	0.06%	0.0008%	3.3%	3.3%	3.3%		

*The efficiency may not reflect the practical scenario as it depends on type of fiber used. However, the values can be taken as relative comparison.

Outlook

Inclusion of the on-chip fiber coupler can significantly increase (4-5 times) the coupling efficiency between hollow-core fiber and the external optics setup. Additional modification is also proposed to minimize Fresnel back reflection to the hollow-core and solid-core fibers which can be useful in some applications.

2.7 Application: Fiber integrated cavity

Several notable demonstrations of strong light-matter interactions and nonlinear optical processes at low light levels in hollow-core fibers have been reported in recent years. They include all-optical switching with few-hundred photons[40] and stationary light pulses[41] in hollow-core photonic crystal fibers (HCPCFs) loaded with laser-cooled atoms, as well as cross-phase modulation with few photons[42] and single-photon broadband quantum memory[43] in HCPCFs filled with room temperature alkali atoms. At the same time, there is potential to further enhance such processes by integrating a cavity into the hollow-core fiber, which would broaden the new horizons already opened by the hollow-core fiber platform.

High-finesse cavities have been reported with reflective coatings deposited on the ends of a solid-core fiber piece[44]. Additionally, cavities in solid-core photonic-crystal fibers were earlier realized by pressing mirrors against the cleaved ends of a fiber section[45]. Unfortunately, sealing the face of a HCPCF with a multilayer reflective coating or with a mirror would make it impossible to introduce gases into the fiber core after the cavity has been formed.

Metallic and dielectric metasurfaces, formed by large two-dimensional arrays of nanoscale patterns, have been extensively explored in the past decade due to their capabilities to manipulate light in previously unimaginable ways[46–48]. Metasurfaces realized by perforating dielectric membranes, also known as photonic crystal slabs[49] or high-contrast gratings[50], offer the additional advantage of being permeable by gases and liquids[51] and thus make an almost obvious choice as a technology for forming a cavity inside a HCPCF. The first demonstration of experimentally realized cavity with metasurface mirror integrated with HCPCF was reported by Flannery et. al. [52]. Though the reported finesse was ~ 11 and Q factor was $\sim 4.5 \times 10^5$, much higher values should be achievable with improved fabrication procedures. The schematic of the hollow-core fiber integrated cavity and experimental setup is depicted in Figure 2.16.

Direct coupling of SMFs on both sides of the mirror-mounted HCPCF can provide better coupling efficiency which can lead to new fiber integrated lasers, enhanced gas spectroscopy device, studies of fundamental light-matter interactions and nonlinear optics. As a particular example, we aim to fabricate a fiber integrated UV laser where the cavity is formed by photonic crystal mirrors designed for UV wavelength mounted on a HCPCF and SMFs are integrated using the on-chip splicer for input/output coupling. Additionally, we also intend to take the similar approach to fabricate a gas sensor at telecom wavelength. For insertion of gas inside the hollow-core region of the fiber, a small gap between HCPCF and SMF can be kept at the cost of a small reduction in coupling efficiency. Last but not the least, a fiber integrated cavity can significantly improve the interaction probability between photon and atom in the cold-atom setup mentioned in the previous section.

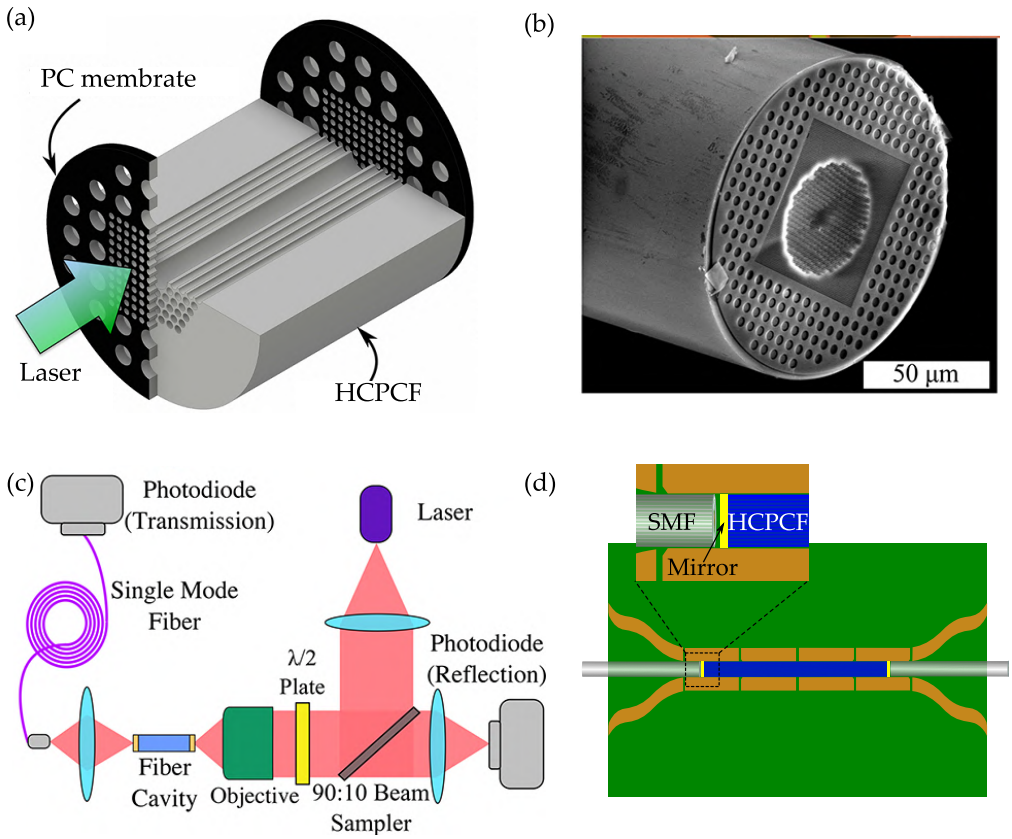

FIGURE 2.16: (a) HCPCF-integrated Fabry-Pérot cavity. The fiber serves as the cavity medium and confines light in the transverse direction, while a pair of dielectric metasurfaces (PC membranes) mounted on the ends of the fiber segment confine light longitudinally. (b) SEM image of the PC membrane attached to the tip face of a HCPCF segment. The center square lattice of PC holes in the membrane covers the entire PC region of the underlying HCPCF. (c) Optical setup used to inject light into the fiber-cavity from free space and to measure the transmission and reflectivity spectrum. A half-wave ($\lambda/2$) plate is used to align the polarization of the input light with the slow and fast axis of the birefringent HCPCF. ((a-c) are from [52]) (d) Schematic of the proposed fiber integrated cavity setup.

2.8 Conclusion

The on-chip fiber splicer offers an excellent alternative to fusion splicing for applications where a connection between solid-core fiber and HCPCF is needed, such as fiber-integrated cavities and spectroscopy cells and cold atomic ensemble in a HCPCF. The maximum observed efficiencies from a SC SMF to HCPCF is 90% and from a HCPCF to a SC SMF is 80%. Efficiency between conventional SMFs can be as high as $\sim$100% with the inclusion of index matching liquid at the joint region. Additionally, a relatively high coupling efficiency is maintained even when a gap is introduced between the two fiber ends and the coupling in the presence of a gap could be further improved by fabricating a lens at the fiber tip. Having such gap can be potentially utilized for lab-on-a-chip applications [53, 54] in which the gap would be combined with microchannels to introduce liquids or gases into the HCPCF or anti-resonant reflecting optical waveguide (ARROW) for probing by tightly-confined guided light.

Chapter 3

High Efficiency Fiber-Coupled Single-Photon Source Based on Quantum Dot Embedded in a Semiconductor Nanowire

3.1 Introduction

Quantum photonics, as the name suggests, is the study of the generation, manipulation and detection of single quanta of light (i.e. photons). Though we are far from the ideal scenario, scientists and researchers across the globe are constantly trying to solve bits and pieces of the big puzzle to reach the said goal. To realize the full potential of quantum photonics, three main technologies are essential: an ideal single photon source (SPS), linear and non-linear photonic circuits and fast and efficient single photon detectors. While the last two technologies are out of scope for this chapter, we will discuss briefly about different aspects of single photon sources and streamline our discussion towards the main focus of this chapter.

Ideal Single Photon Source: An ideal single photon source should posses three main characteristics [55–57]:

- **Single Photon Purity:** The light pulse should contain only a single photon instead of multiple photons. Purity of the source is the most fundamental metric and can be determined by the second order correlation function $g^2(0)$ measured by a Hanbury Brown and Twiss experiment. A light pulse with only a single photon leads to $g^2(0) = 0$, whereas $g^2(0) = 1$ for coherent light (laser) and $g^2(0) > 1$ for non-coherent light.
- **Deterministic or On-demand:** A deterministic light source should generate only a single photon following an input trigger, optical or electrical, to the desired quantum channel without any vacuum component. However, this definition needs to be clarified as different nomenclature is adopted in different literature. Photon emission probability depends on the source efficiency and repetition rate. Source efficiency refers to the fraction of applied triggers with which a single photon is collected from the source (unity in the ideal case) and repetition rate indicates the maximum rate at which the source can emit single photons (typically in the MHz range), sometimes referred to as saturation excitation. The source efficiency η can further be divided into the generation efficiency η_g and the extraction efficiency η_{ext} as $\eta = \eta_g * \eta_{ext}$ [58]. Generation efficiency states the probability of the single photon emission from the source per trigger under saturation excitation. Extraction efficiency refers to the probability of collecting the

emitted photon to an external component, for example, just after the physical source, at the first lens, at the output of the single mode fiber (SMF) and so on. This is because the optical components are not loss-free and coupling to different components induces some loss.

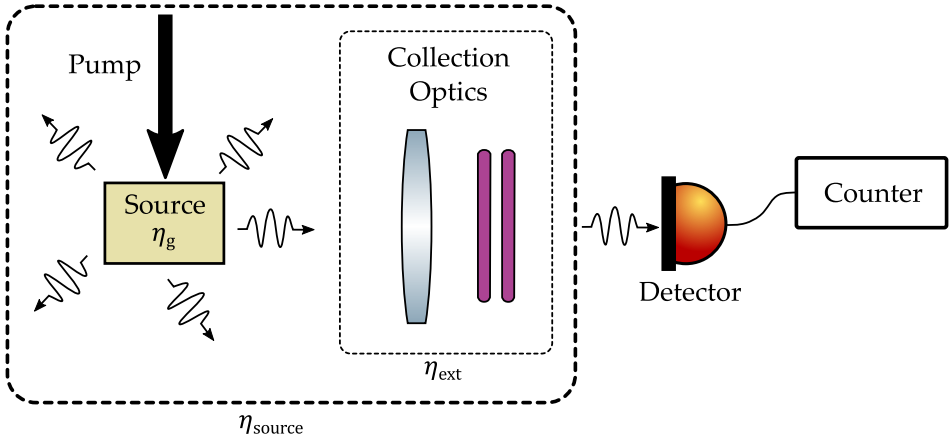

FIGURE 3.1: Single photon source efficiency [58].

- **Indistinguishability:** Indistinguishability indicates that successive single photons are identical in terms of polarization, spatial mode and temporal mode which are requirements for quantum interference. Hong-Ou-Mandel (HOM) interference measurements can be used to determine the indistinguishability of the photons.

Additional characteristics for an ideal single photon source includes high repetition rate (GHz range is desirable), tunable wavelength, electronic trigger and photon emission into a Gaussian mode for high efficiency fiber coupling.

3.2 Single Photon Sources

Single photons can be obtained from various schemes including attenuated lasers, nonlinear frequency conversion, and spontaneous emission of single quantum emitters. The attenuated laser is low cost and readily available, however, having the disadvantages of being non-deterministic and characterized by $g^2(0) \geq 1$ does not make it an ideal source. In nonlinear frequency conversion, also known as spontaneous parametric down conversion (SPDC), a photon incidents on a nonlinear crystal is converted into two photons. Though this process is robust and works at room temperature, it has the drawbacks of being non-deterministic and generates photon pairs at a linear rate with the pump field intensity, which prohibits it becoming an ideal candidate for a single photon source. The spontaneous emission from a two-level quantum emitter is inherently single-photon like. Early demonstrations of single-photon emission were based on atoms [18], ions [19] and molecules [20], and followed by demonstrations with artificial atoms in a solid-state environment. Unlike attenuated lasers or SPDC sources, the deterministic nature of these sources can be intrinsically decoupled from the single-photon purity. A plethora of systems for solid-state single photon emitters have been investigated over the past decade, the most promising ones being the atomic defects (color centers) in bulk 3D or 2D materials and quantum dots (QDs). Among the

various color center platforms, defects in diamond including nitrogen–vacancy (NV) or silicon–vacancy (SiV) are the most studied. The major challenge of the diamond platform is only a fraction of photons are emitted in the zero-phonon line even at cryogenic temperature and collection of emitted light is complicated due to high refractive index contrast. A quantum dot is a 0D material (dimensions are in nm scale) which acts as a two-level artificial atom and can emit single photons. Taking into consideration the three main characteristics of an ideal single photon source, the source technology that at present comes closest to meeting all of the expectations is the semiconductor quantum dot [56, 59, 60]. The semiconductor QDs are typically fabricated using III-V semiconductors, for example in this work using InP/InAsP. A low energy gap QD (InAsP) is embedded in a slightly higher energy gap bulk material (InP). Tight quantum confinement in the QD leads to discrete energy levels for both electrons and holes. Each discrete energy level can contain at most two electrons (in conduction band) or holes (in valence band) due to Pauli exclusion principle. Following the right trigger pulse, a bound state of electron and hole pair is generated (known as an exciton). Due to small spatial scale in QD, Coulomb interaction comes in to play and creates excitons rather than free electron and hole pairs. Depending on different spin configurations and filled (or empty) state, different excitonic states are possible in a QD as depicted in Figure 3.2.

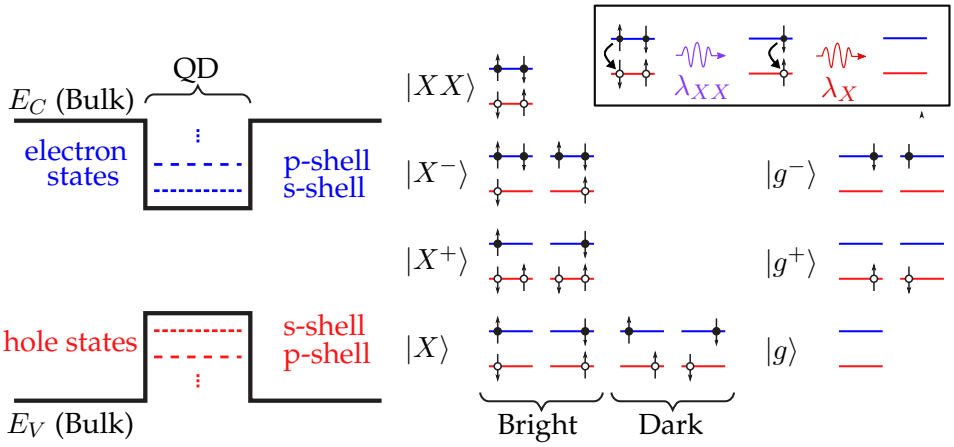

FIGURE 3.2: (left) Schematic energy band diagram for a QD embedded in a bulk host semiconductor where E_C is the conduction band and E_V is the valence band energy. (middle) exciton configurations (exciton $|X\rangle$, charged excitons $|X^{\pm}\rangle$ and biexciton $|XX\rangle$) of the s-shell discrete energy levels. Filled and empty circles represent electrons in conduction band and holes in valence band, respectively. Arrows represent the up or down spin state. (right) ground states (charged $|g^{\pm}\rangle$ and neutral $|g\rangle$) corresponding to recombination of the excitons. (inset) radiative recombination of carriers in biexciton configuration by successively emitting photons in a cascade. The last two emitted photons in a neutral exciton cascade are emitted at different wavelengths (λ_{XX} and λ_X) because of Coulomb interaction [61].

In quantum communication, entangled photon sources with high fidelity and high efficiency are often required for secure communication. The entanglement fidelity is a measure of how well the entanglement between two photons is preserved in a quantum process. For practical Quantum Key Distribution (QKD) using BB84 protocol, the bit error rate (BER) has to be less than 11% for secure communication. However, a quantum light source combining both high entanglement fidelity and on-demand bright emission has been elusive. Two of

the mostly used single photon sources for such applications are SPDCs and QDs. A comparison of the state of the art performance from these sources are depicted in Figure 3.3 [62, 63]. The squares and circles represent the SPDC sources and QD sources respectively. Here, the photon-pair source efficiency is defined as the probability of collecting a photon pair per excitation pulse into the first lens (for QDs) or fiber (for SPDCs). For the SPDCs, the entanglement fidelity has a mutual dependence on the photon-pair source efficiency due to the probabilistic nature of the pair generation efficiency. Therefore, these sources cannot have near-unity photon-pair source efficiency while maintaining a high fidelity. It approaches to 0.5 as the pair source efficiency approaches to 100% [63]. In contrast, since quantum dot sources are deterministic and can emit photon pairs on demand, they have the potential to reach near-unity source efficiency without negatively influencing the entanglement fidelity. However, it's worth mentioning that the data shown on the plot for QD sources are measured at the first lens, coupling it to a SMF adds other losses occurred from collection and coupling optics. In this work, we focus on improving the quantum dot source efficiency by enhancing the photon extraction efficiency.

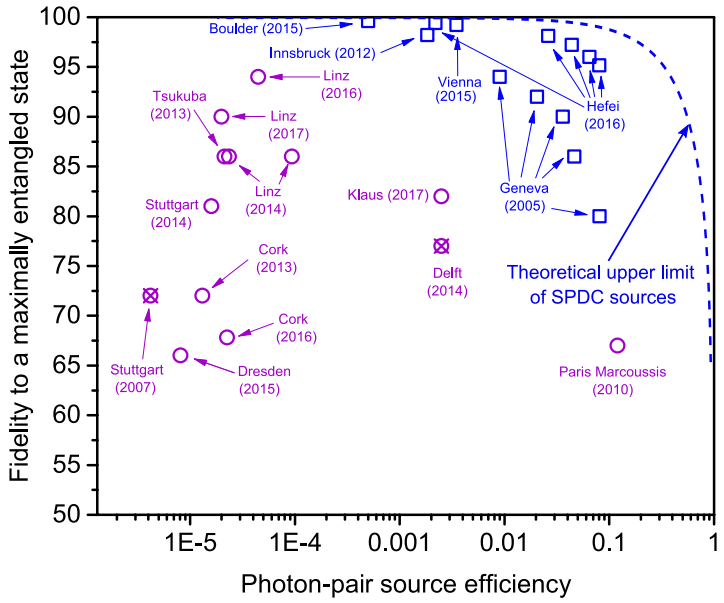

FIGURE 3.3: Comparison of the entanglement fidelity and photon-pair source efficiency of different SPDC sources (squares) and quantum dot-based (circles) entangled photon-pairs sources [62]. A theoretical upper limit for the SPDC sources are shown from [63].

3.3 Objective of this work

Despite demonstrating excellent progress by semiconductor QD single photon sources [56, 59, 60], all of the aforementioned criteria to be an ideal single photon source have not yet met simultaneously in a QD device. One of the major challenges, inter alia, remains the overall collection efficiency of the emitted photon into a SMF (η_{ext} in Figure 3.1) due to high refractive index contrast between the III-V semiconductors and air. Several schemes have been proposed to overcome this challenge where nanophotonic structures including micropillar

cavities [22, 23], Bragg gratings [24] and photonic nanowires [25] were used. Nevertheless, due to directionality of the emitted photon, reflection at the high refractive index boundary, very high numerical aperture (NA) of the output mode and loss in the optical components, overall collection efficiency at the SMF is very low compared to the theoretical limit. In this work, we propose a complete scheme for high efficiency light coupling from an InP/InAsP quantum dot to a single mode fiber. The QD is embedded in a tapered nanowire waveguide (QD-NW) [21] where the geometry of the NW is optimized to have Gaussian output mode along with relatively low NA. A lithographically defined alignment structure is designed to house the collection fiber, where a graded index multimode fiber lens (GRIN-lens) in combination with a core-less fiber and an SMF is designed for high efficiency coupling of light from the nanowire into the fiber. The schematic of the proposed scheme is illustrated in Figure 3.4.

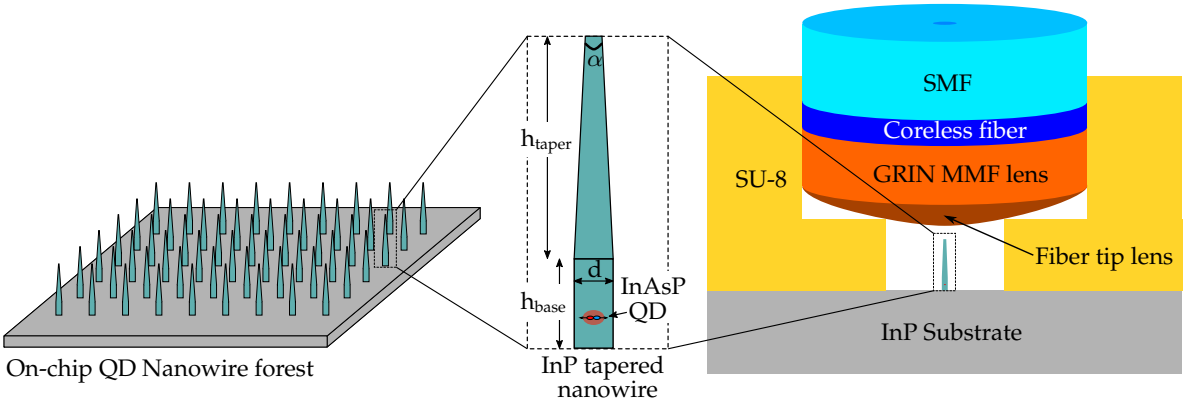

FIGURE 3.4: Schematic diagram of the proposed design (not to scale). The tapered nanowire waveguide is made of InP, the QD is made of InAsP, d and h_{base} are the diameter and height of the nanowire at the base, respectively, α is the full taper angle at the tip and h_{taper} is the height of the tapered region. A single mode fiber is spliced with a core-less fiber spliced with a GRIN multimode fiber which acts as a lens, and the tip of the GRIN fiber is melted to act as an additional lens. The fiber structure is being held by a lithographically defined alignment structure made of SU-8 photoresist.

3.4 Design

The overall design of this system can be divided into three segments, QD nanowire design for desired Gaussian mode output, fiber integrated lens design for efficient collection of light and alignment structure design to hold the fiber.

3.4.1 Nanowire design

Nanowire waveguide (NW) has to be such that the emitted photons from the QD couple efficiently to the guided mode of the waveguide and the output light from the nanowire has to have a Gaussian profile with relatively low NA for low coupling loss to the SMF. Therefore, the NW consists of a cylindrical base, where the QD is placed, and a slowly tapered tip for adiabatic expansion of the guided mode. As the emission profile from the QD strongly depends on the position of the QD, NW diameter, taper angle and taper height, the waveguide

geometry is optimized for $\lambda = 890\,nm$ using finite difference time domain (FDTD) simulations in Lumerical software. This wavelength will be used throughout the chapter unless otherwise stated.

Nanowire diameter

Number of guided modes in the waveguide depends on the wavelength and the nanowire diameter (D), with our target being single mode waveguide at desired wavelength. To simulate the structure, we used the refractive index for InP as n_{InP}=3.4. The result is depicted in Figure 3.5. The diameter is varied from 120 nm to 500 nm which corresponds to D/λ= 0.112 to 0.562. There is no guided mode in the waveguide for D < 133 nm and for D > 211 nm higher order modes (TE_{01}, TM_{01} and so on) start guiding, therefore the diameter has to be a value between these two boundaries. To efficiently couple the emitted photons from the NW to the SMF, the output light should ideally possess a Gaussian profile with low NA. We used 3D FDTD simulations to investigate the effect of NW diameter on the output light profile. For this simulation, the parameters used are, $h_{base} = 1.5\,\mu m$, $h_{taper} = 5\,\mu m$, $h_{QD} = 408\,nm$,

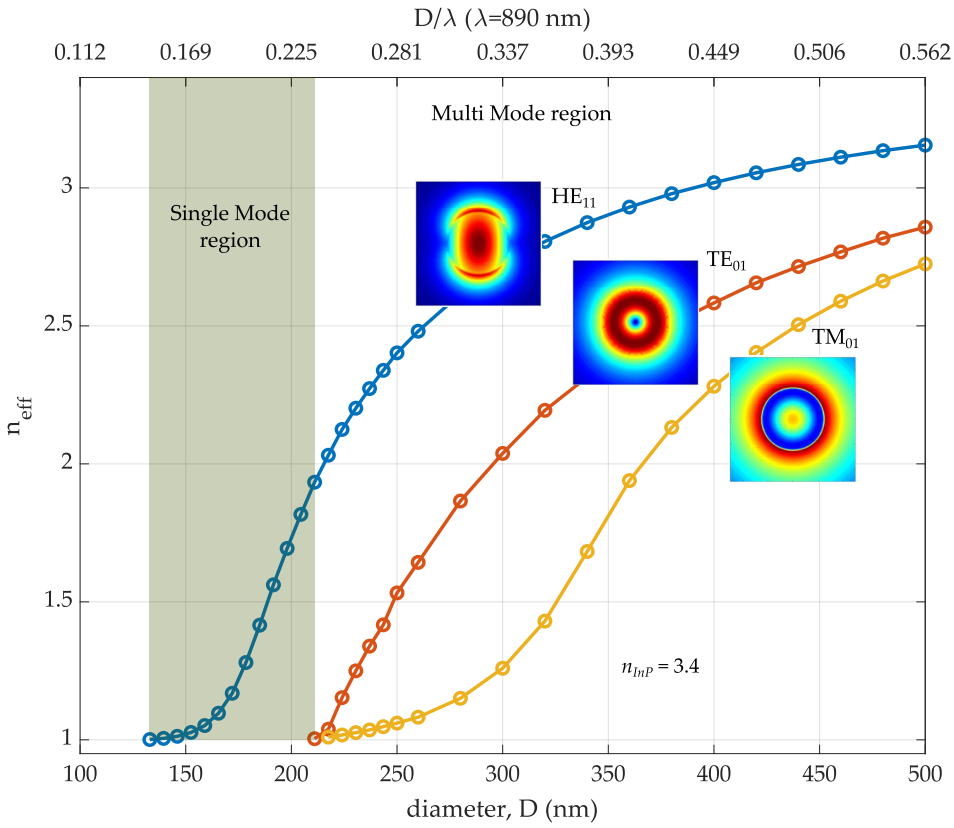

FIGURE 3.5: Nanowire waveguide modes at varying nanowire diameter. For D/λ below 0.237 (D < 211 nm) the nanowire supports only a single guided mode (HE_{11}, though there are two degenerate modes, only one is shown. The other mode looks similar but rotated 90°) and becomes a multimode waveguide for higher diameters. The first two higher order modes: TE_{01} and TM_{01} are shown. The spatial distribution of the electric field of the modes inside the waveguide is also shown.

$\alpha = 1°$. It is worth mentioning that, these parameters are not all optimized, some are taken from literature [2], however that won't affect the output light qualitatively. The results are depicted in Figure 3.6. Diameters are chosen such that the NW guides single mode to multimode and the evolution of the emitted light shows the overlap with Gaussian for all of them is >95%, however the spreading of the light changes significantly. As shown in the inset, the NA is minimum for 200 nm diameter and in the multimode region, it increase rapidly. As for the diameter of $d = 200nm$, the overlap is 98.6% and the NA is minimum, we choose this value for the NW base diameter.

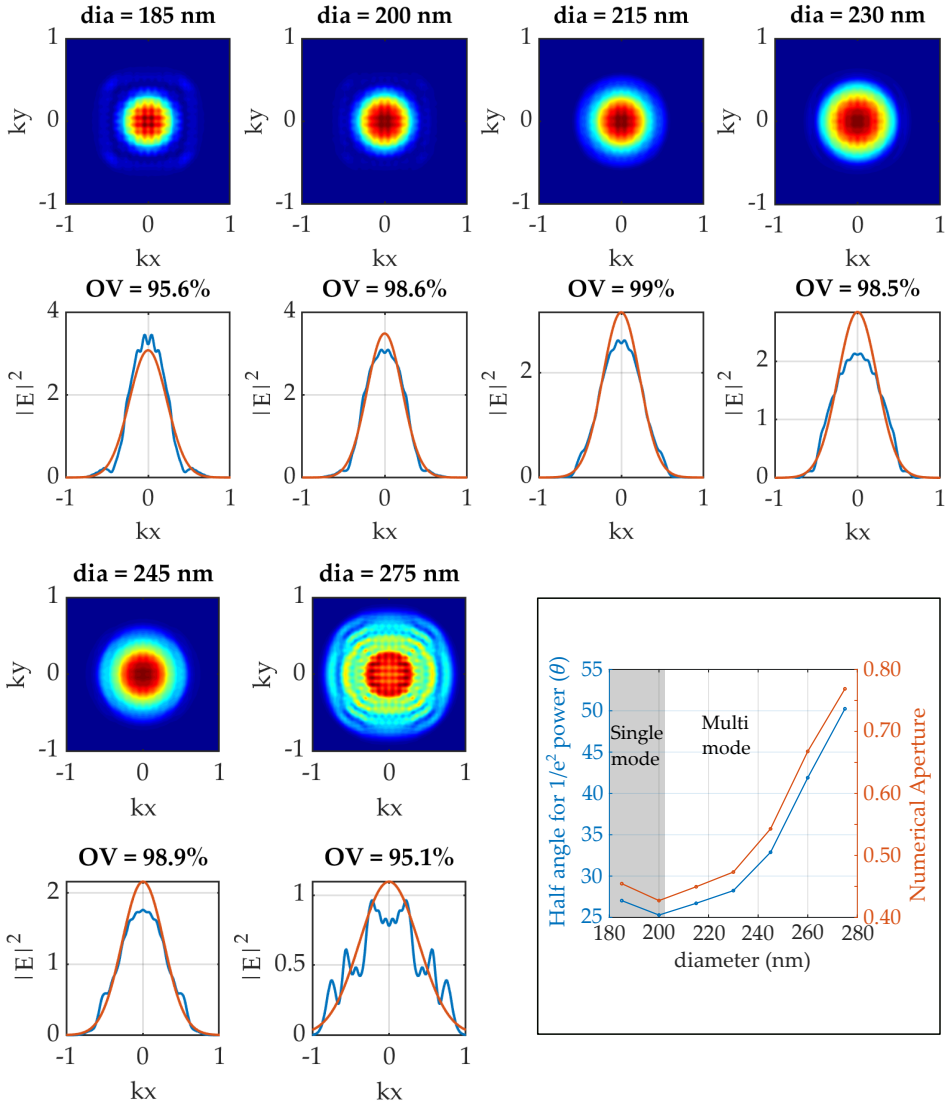

FIGURE 3.6: Evolution of the emitted light profile vs diameter of the nanowire is illustrated. The diameters are chosen such that the NW guides single mode to multimode, and the intensity profile is measured at 5 µm from the tip of the nanowire. Overlap integral is calculated for intensity profile ($|E|^2$). (inset) Half angle for $1/e^2$ power (θ) and NA vs diameter is shown. θand NA is minimum for d = 200 nm which is single mode guiding.

Quantum Dot position

The QD has to be at the optical axis of the waveguide, in this case at the center of the waveguide cross section. However, the height of the QD along the axis should be chosen carefully because of the reflected light interference. Reflection from the nanowire-air interface would have negligible effect due to adiabatic tapering of the nanowire. On the other hand, reflection from the nanowire-substrate interface due to the refractive index mismatch can interfere constructively or destructively depending on the position of the QD. For constructive interference, the source must be placed at an anti-node so that the light propagates a half-integer multiple of the wavelength (i.e. $(n+\frac{1}{2})\lambda$ where $n = 0, 1, 2, ...$) which, combined with the π phase shift on reflection, means total phase shift is $2(n+1)\pi$. The wavelength in this case is the effective wavelength in the waveguide and the anti-node heights which allow for constructive interference can be written as:

$$h_{anti-node} = \frac{\lambda}{2n_{eff}}(n+\frac{1}{2}); \text{where } n = 0, 1, 2, ... \tag{3.1}$$

For NW diameter of 200 nm, $n_{eff} = 1.73$ (given $\lambda = 890\,nm$), and using the above equation the calculated heights of the anti-node in the NW are, $h_{anti-node} = 129\,nm$, $386\,nm$, $643\,nm$, $900\,nm$, ... Now, if we assume an infinitely long cylindrical waveguide and place a QD at the optical axis, light propagating in upward and downward direction will be equally split. However, for the tapered nanowire on the substrate, we can assume no reflection from the tapered side and some reflection from the nanowire-substrate interface which can be calculated using Fresnel equation as, $R = [(n_{sub} - n_{nw})/(n_{sub} + n_{nw})]^2 = [(3.4 - 1.73)/(3.4 + 1.73)]^2 = 10.6\%$. To verify this theoretical calculation, numerical simulation has been carried out in Lumerical and the result is depicted in Figure 3.7. The Purcell factor and the transmission are defined in the Lumerical as:

$$Purcell factor = \frac{dipole power(f)}{source power(f)} \tag{3.2}$$

$$T(f) = \frac{\frac{1}{2}\int real(P(f)^{monitor}) \cdot dS}{source power(f)} \tag{3.3}$$

Here, $dipole power(f)$ is the power emitted by a dipole source in the environment at frequency f, $source power(f)$ is the power emitted by the dipole in a homogeneous environment (bulk material), $T(f)$ is the transmission through the monitor, $P(f)$ is the Poynting vector normal to the surface and dS is the surface normal. Therefore, the transmission has to be normalized by the Purcell factor to get the correct result. As can be seen from the figure, upward and downward transmissions both vary in a sinusoidal fashion depending on the position of the QD. The maximum upward transmission is $\approx 57\%$ at the QD height of $\approx 385\,nm$ which matches with our prediction.

Nanowire base height

As we decided on the diameter of the NW and the axial QD position inside the NW, next step is to check if the height of the cylindrical base has any effect or not. The simulation is done with the parameters, $d = 200\,nm$, $h_{taper} = 5\,\mu m$, $h_{QD} = 408\,nm$, $\alpha = 1°$ and variable base height. As we can see from the results shown in Table 3.1, for a change in the base

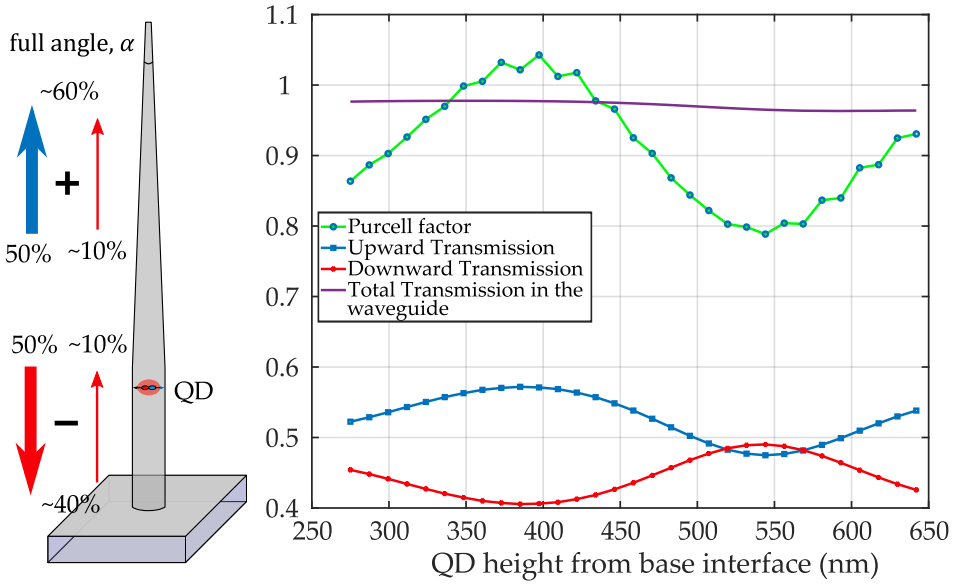

FIGURE 3.7: Simulated structure is illustrated at the left. The parameters for the simulation are, d = 200 nm, h_{base} = 1.5µm, h_{taper} = 4µm, full taper angle α= 2°. Purcell factor, upward and downward transmission follow a sinusoidal pattern depending on the QD height in the nanowire. For QD height of $\approx 385\,nm$, the upward transmission is maximum ($\approx 57\%$) and the downward transmission is minimum ($\approx 41\%$). Total transmission is the summation of both upward and downward transmission which is almost constant.

height while the diameter and the QD position is fixed, the changes in different parameters are insignificant. Therefore we choose the base height to be, h_{base} = 1.5µm.

TABLE 3.1: Simulation result for varying base height of the nanowire

Base height (µm)	Purcell factor	Upward Transmission	Overlap with Gaussian	half-angle, θ	NA
1.5	1.22	0.52	0.99	25.29	0.43
2.0	1.21	0.52	0.98	26.39	0.44
2.5	1.22	0.52	0.98	24.43	0.41
3.0	1.23	0.51	0.99	25.66	0.43
3.5	1.24	0.51	0.97	24.95	0.42
4.0	1.24	0.50	0.99	24.60	0.42

Nanowire taper angle and height

The purpose of the taper region of the NW is to adiabatically transform the mode profile to prevent reflection from the nanowire-air interface and to get a desired Gaussian output profile with low NA for efficient coupling to the SMF. The structure was simulated for d = 200 nm, h_{base} = 1.5 µm, h_{QD} = 408 nm, α= [0.5°, 1°, 2°] and h_{taper} = 0 µm to 10 µm and the result is illustrated in Figure 3.8. For low taper heights, though the upward transmission should be close to 50%, the low upward transmission is due to small simulation region in

FDTD simulation. At these heights, the NA of the emitted light is large which requires a large simulation region to collect the light and therefore increases the simulation time significantly. However, the NA is correct as it is measured at $1/e^2$ power. For 2° taper, the small dip in NA is due to a simulation artifact. Looking at the general trend, it shows that lower taper angle and longer taper height yield lower NA. Therefore, our target is h_{taper} = 10 µm and α= 0.5° (or as close as possible).

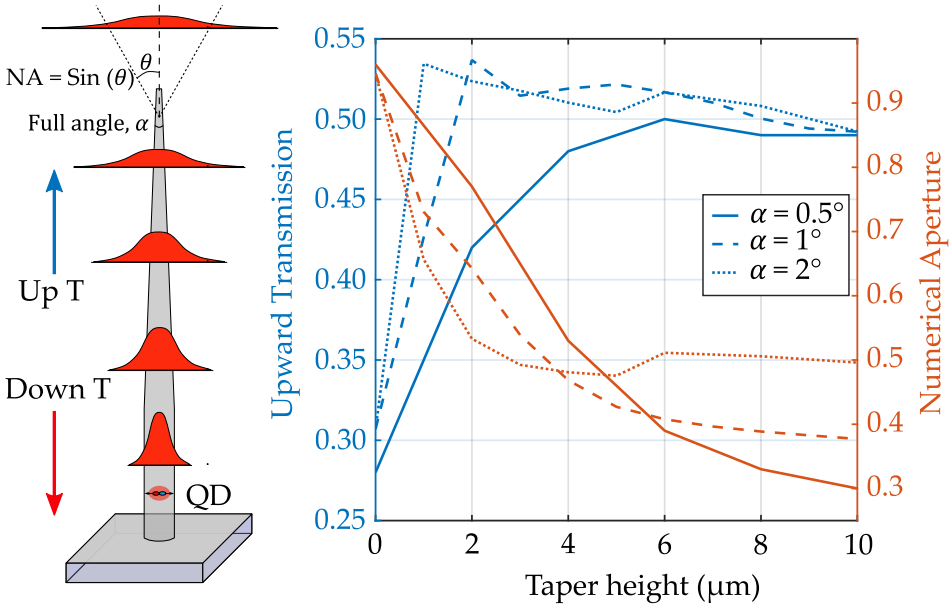

FIGURE 3.8: Upward transmission and NA vs. taper height for different taper angles are depicted. For low taper heights, the low upward transmission is due to small simulation region in FDTD simulation, otherwise the simulation time increase significantly. In this case, the upward transmission should be close to 50%. However, the NA is correct as it is measured at $1/e^2$ power. For 2° taper, the small dip in NA is due to simulation artifact. Looking at the general trend, is shows that lower taper angle and longer taper height yield lower NA.

3.4.2 GRIN fiber lens

In the graded index multimode fiber, the core has a non-uniform refractive index unlike conventional step index fiber. The index of refraction can be expressed as:

$$n(r) = n_0\sqrt{(1 - g^2r^2)} \tag{3.4}$$

$$g = \frac{\sqrt{2(n_0 - n_{clad})}}{r_{core}} \tag{3.5}$$

Where n_0 is the maximum core index at the center, g is the focusing parameter, r is the distance from the center of the core towards cladding and r_{core} is the fiber core radius. This type of refractive index profile is also called a square-law medium. In the square-law medium, light bends in an oscillatory fashion as it propagates through the medium. Therefore, graded index in the core causes lensing effect inside the fiber as if multiple convex lenses are cascaded one after another. Thus, carefully chosen length of a GRIN fiber can be used as a

convex lens with a desired focal distance. The integrated GRIN fiber lens has several advantages over conventional lenses including i) small size ii) low-cost and iii) stable fiber-lens interface. The addition of GRIN lens improves the collection efficiency by increasing the numerical aperture. It also reduces the lateral and longitudinal misalignment sensitivity by expanding the beam, although, at the same time increases the angular misalignment sensitivity. However, the overall advantages surpass the disadvantages [64].

In this work, an SMF is spliced with the GRIN MMF and then the GRIN fiber is cleaved at a desired length (optionally a segment of core-less fiber can be inserted between SMF and GRIN fiber depending on the desired mode at the output). Focal distance and waist of the lens can be calculated using a transfer matrix method [64–66].

Analysis of Fiber integrated GRIN lens

For this application, paraxial approximation can be used for the Gaussian beam propagating through the fibers. Therefore, the ABCD law can be utilized for propagating Gaussian beams through the optical system and for designing the fiber integrated GRIN lens. The complex q parameter for Gaussian beam can be defined as:

$$q(z) := z + iz_0 \tag{3.6}$$

Here, z is measured from the beam focus and z_0 is the Rayleigh length defined as $z_0 = \pi w_0^2/\lambda$, w_0 is the beam waist radius at the focus in which the field (intensity) amplitude falls to $1/e$ ($1/e^2$) of its axial value. The q parameter is a compact form from which the entire geometry of the Gaussian beam can be determined. The inverse of q gives a more useful form:

$$\begin{gathered}\frac{1}{q(z)} = \frac{1}{z+iz_0} = \frac{z-iz_0}{z^2+z_0^2} = \frac{z}{z^2+z_0^2} - i\frac{z_0}{z^2+z_0^2} \\ \boxed{\frac{1}{q(z)} = \frac{1}{R(z)} - \frac{i\lambda}{\pi w^2(z)}} \\ \text{where,} \quad R(z) = z[1+(z_0/z)^2] \\ w(z) = w_0\sqrt{[1+(z/z_0)^2]}\end{gathered} \tag{3.7}$$

Here, $R(z)$ and $w(z)$ are the radius of curvature and beam waist radius at z, respectively, and λ is the wavelength in the medium. The transformation of $q(z)$ from an input plane to an output plane can be found from:

$$q_2 = \frac{Aq_1 + B}{Cq_1 + D} \qquad \text{where,} \quad M = \begin{bmatrix} A & B \\ C & D \end{bmatrix} \tag{3.8}$$

Here, M is the transfer matrix from input plane to output plane. This transfer matrix can be obtained from a product of transfer matrices where each matrix represents a small segment of the overall optical system. This approach is applied to an optical system consisting of SMF–Core-less fiber–GRIN fiber as depicted in Figure 3.9. Different interfaces are marked

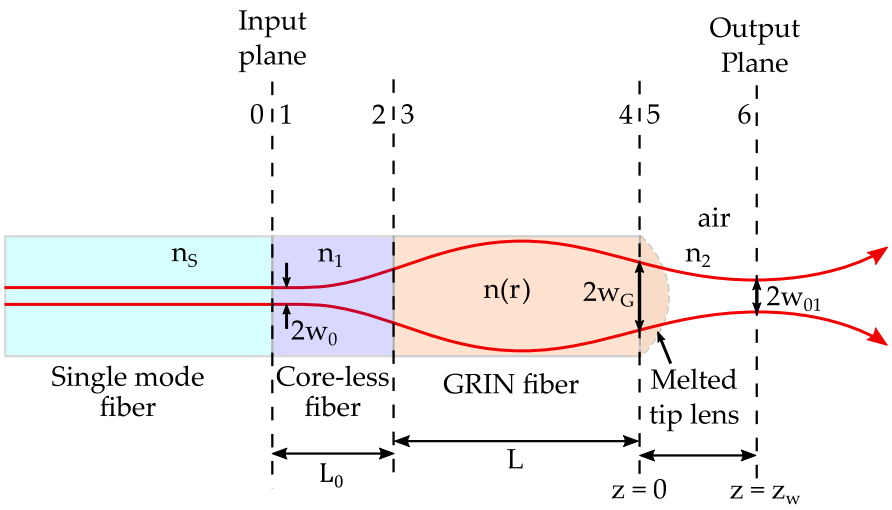

FIGURE 3.9: Optical system consists of SMF–Core-less fiber–GRIN fiber. Different interfaces are marked with dashed lines, n_x is the index of refraction, $n(r)$ is the variable core index of GRIN fiber which is a function of radius, w_0 is the waist radius just after SMF, w_{01} is the waist radius at the output plane, L_0 and L are lengths of core-less fiber and GRIN fiber respectively, z_w is the final waist location relative to the GRIN lens end face. Core-less fiber and melted tip lens are optional.

with dashed lines, n_x is the index of refraction, $n(r)$ is the variable core index of GRIN fiber which is a function of radius, w_0 is the waist radius just after SMF, w_G is the waist radius at the GRIN fiber output face, w_{01} is the waist radius at the output plane, L_0 and L are lengths of core-less fiber and GRIN fiber respectively, z_w is the final waist location relative to the GRIN lens end face. Core-less fiber and melted tip lens are optional.

The overall transfer matrix from input plane to output plane can be written as the product of individual matrices as following (melted tip lens is not considered):

$$M = \begin{bmatrix} A & B \\ C & D \end{bmatrix} = M_{56}M_{45}M_{34}M_{23}M_{12} \tag{3.9a}$$

where,

$$M_{12} = \begin{bmatrix} 1 & L_0 \\ 0 & 1 \end{bmatrix} \qquad M_{23} = \begin{bmatrix} 1 & 0 \\ 0 & n_1/n_0 \end{bmatrix}$$

$$M_{34} = \begin{bmatrix} \cos(gL) & \frac{1}{g}\sin(gL) \\ -g\sin(gL) & \cos(gL) \end{bmatrix} \tag{3.9b}$$

$$M_{45} = \begin{bmatrix} 1 & 0 \\ 0 & n_0/n_2 \end{bmatrix} \qquad M_{56} = \begin{bmatrix} 1 & z_w \\ 0 & 1 \end{bmatrix}$$

Performing the multiplication of set of equations from 3.9b and combining with equation 3.9a yields the following matrix elements:

$$A = \cos(gL) - \frac{n_0}{n_2} z_w g \sin(gL) \tag{3.10a}$$

$$B = \left(L_0 + \frac{n_1}{n_2} z_w\right) \cos(gL) + \left(\frac{n_1}{ng} - \frac{ngL_0 z_w}{n_2}\right) \sin(gL) \tag{3.10b}$$

$$C = \frac{-ng}{n_2} \sin(gL) \tag{3.10c}$$

$$D = \frac{-ngL_0}{n_2} \sin(gL) + \frac{n_1}{n_2} \cos(gL) \tag{3.10d}$$

Using the parameter values from equation 3.10 into the equation 3.8 and then equating the imaginary parts with equation 3.7 yields the waist size at the output plane:

$$w_{01} = w_0 \left(\frac{n_1}{n_2} \frac{A^2 + a^2 B^2}{AD - BC}\right)^{1/2} \quad \text{where,} \quad a = \frac{\lambda}{\pi w_0^2 n_1} = \frac{a_0}{n_1} \tag{3.11}$$

By equating the real parts and using the condition $R \to \infty$ at the beam waist yields:

$$AC + a^2 BD = 0 \tag{3.12}$$

Solving equation 3.12 gives z_w and then substituting z_w in equation 3.11 gives w_{01}. Thus, both the position and the size of the output beam is determined. First the simple case without the core-less fiber, $L_0 = 0$, is considered. The light coming from SMF is injected into the GRIN lens and depending on the length of the GRIN fiber, the output parameters z_w, w_{01} and w_G varies (the parameters are defined in Figure 3.9). The plot of these parameters' analytical values are depicted in Figure 3.10 where 780HP fiber ($w_0 = 5 \pm 0.5\,\mu m$ at 850 nm, NA $= 0.13$) is used for SMF and GIF625 graded index multi-mode fiber (Core Diameter $= 62.5 \pm 2.5\,\mu m$, NA $= 0.275 \pm 0.015$) is used for GRIN lens. As we can see in the figure, all the parameters vary periodically with the length of the GRIN fiber, as if multiple lenses are cascaded together. Negative and positive z_w values mean the fiber acts as a diverging and converging lens respectively. This can also be seen from w_{01} and w_G. In the converging region w_{01} decreases with the increase of length until a minimum point after which the lens enters into the diverging region again. Though the parameter w_G is the beam waist at the end face of the GRIN fiber, plotting it against the length of the GRIN fiber shows the actual beam waist inside the fiber. Care has to be taken to design the lens so that w_G does not exceed the fiber core radius.

Similar plots with core-less fiber segment are also depicted in Figure 3.10 ((middle) and (bottom)) for $L_0 = 200\,\mu m$ and $L_0 = 400\,\mu m$. Addition of core-less fiber segment offers several advantages including longer focal length (higher value for z_w) and tighter focal spot (smaller value for w_{01}). However, the length of the core-less fiber should be less than the limit where the beam size becomes equal to the GRIN fiber core size, which is $\sim 400\mu m$ for the fibers considered here. As can be seen from the plot, insertion of a core-less fiber increases the focal distance z_w and output beam waist w_{01}.

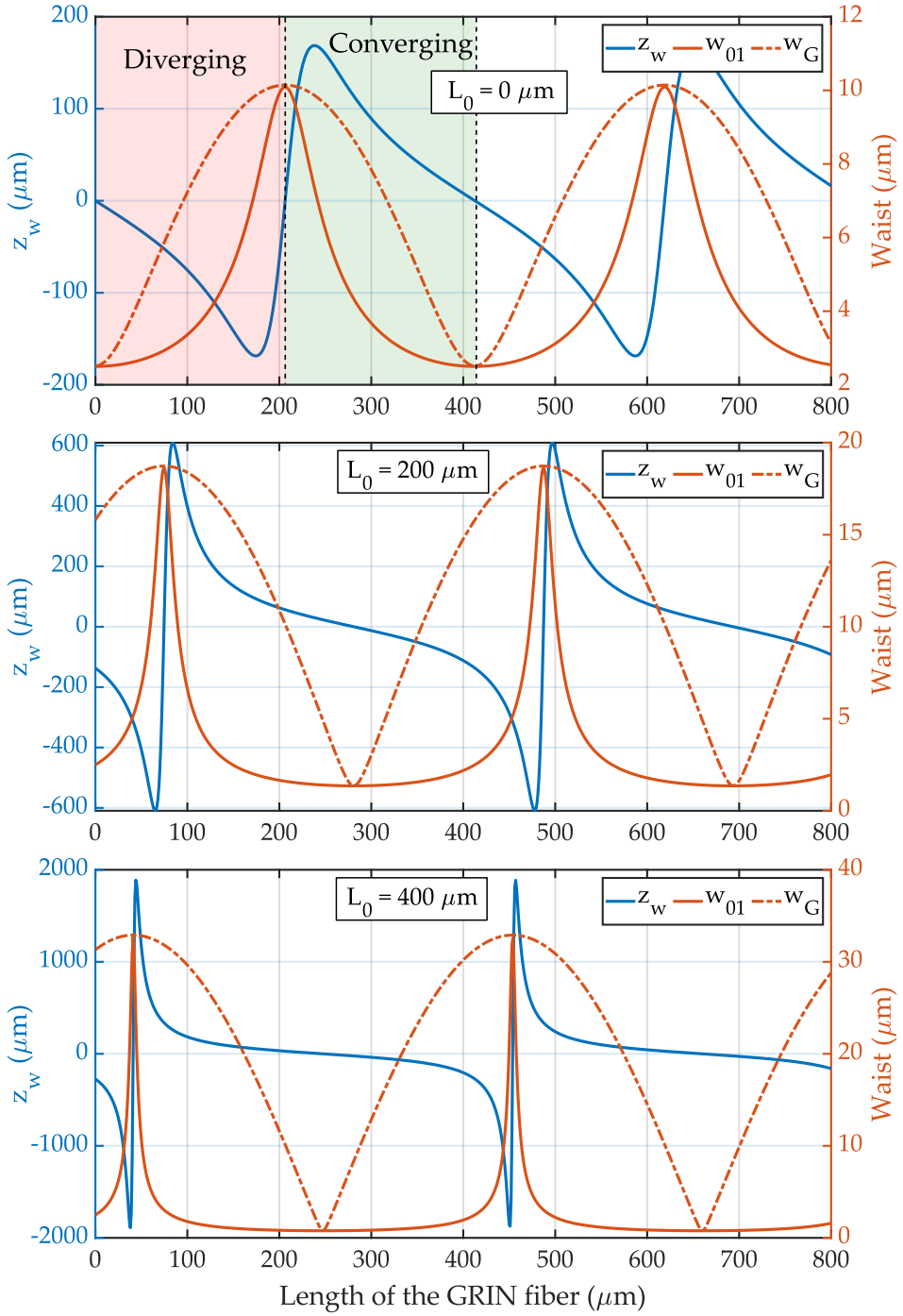

FIGURE 3.10: Output beam waist location z_w, radius w_{01} and beam radius at GRIN lens end face w_G are plotted against the length of the GRIN fiber for: without core-less fiber (top), 200 μm and 400 μm long core-less fiber (middle) and (bottom) respectively. The parameters vary periodically with the length of the GRIN fiber. Initially it acts as a diverging lens and then acts as a converging lens and the pattern continues. In the converging region: z_w is positive, initially increases until a maximum point and then decreases, w_{01} decreases monotonically until a minimum point after which the lens enters into the diverging region. Addition of core-less fiber segment offers longer focal length (higher value of z_w) and tighter focal spot (smaller value of w_{01}).

For a better understanding of how the changes occur, a plot of maximum possible focal distance $z_{w\,max}$ and output beam waist at that focus w_{01} is illustrated in Figure 3.11 (left). As can be seen from the top x axis, the length is taken such that the expanded beam is just below the GRIN fiber core radius. Both of these parameters increase monotonically with the length of the core-less fiber. Though the higher focal distance is desirable, at the same time lower waist size might be necessary for higher collection (or coupling) efficiency. Depending on the application, i) it might be required to design the fiber integrated lens system for a desired output waist size at a certain focal distance, or ii) it might be required to have a very tightly focused beam irrespective of focal distance. An example of such requirements is plotted in Figure 3.11 (right). Focal distance for $w_{01} = 5\,\mu m$ is plotted at the left and minimum possible output beam waist (at $z_w \approx 0$) is plotted at the right. As can be seen from the plot, more than half millimeter focal distance for 5 µm beam waist and sub-micron focal spot for very short focal distance is achievable.

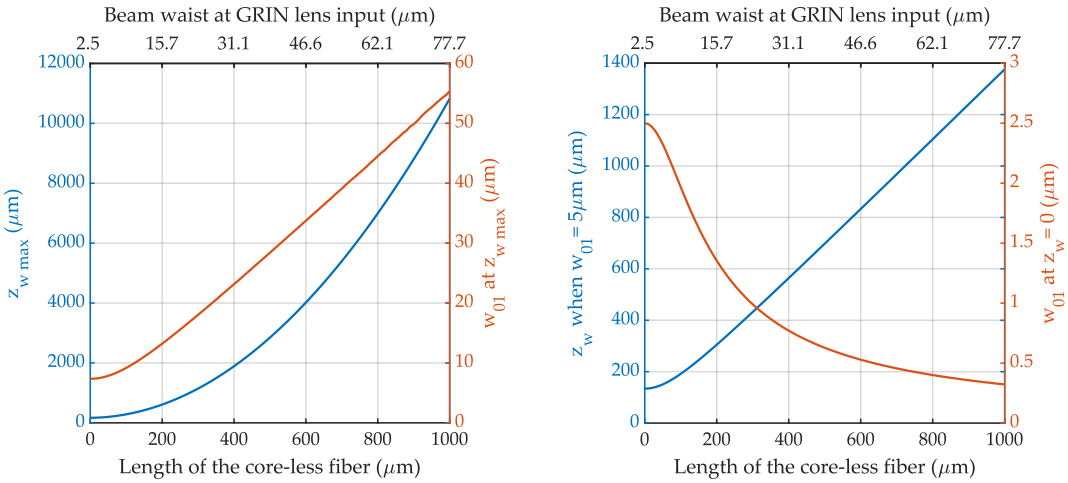

FIGURE 3.11: (left) Maximum possible focal distance z_{wmax} and output beam waist at that focal distance w_{01} vs. Length of the core-less fiber. Expanded beam waist at the GRIN fiber input side, after the core-less fiber segment, is shown at the top x axis. (right) Focal distance for $w_{01} = 5\,\mu m$ and minimum possible output beam waist (at $z_w \approx 0$) vs. Length of the core-less fiber. More than half millimeter focal distance for 5 µm beam waist and sub-micron focal spot for very short focal distance is achievable.

So far the calculation shown is done for a particular graded index fiber, GIF625, used as a GRIN lens. It's worthwhile to explore the possibilities of using other graded index fibers as lens. Graded index fibers are mainly characterized by their focusing parameter, defined as $g = \sqrt{2\Delta}/r$ where $\Delta = (n_{core-axis} - n_{clad})$ and r is the radius of the core, which physically means the index contrast between core-axis and cladding and optically relates how quickly it can focus or defocus a beam. To investigate the effect of g on lens performance, various parameters including focal distance z_w, output beam waist w_{01} and quarter pitch length is plotted against g in Figure 3.12. All the parameters are calculated both without core-less fiber ($L_0 = 0$) and with core-less fiber ($L_0 = 200\,\mu m$ and $L_0 = 400\,\mu m$). In Figure 3.12(a), maximum possible focal distance $z_{w,\,max}$ and beam waist w_{01} at this focal distance vs. g is illustrated. With the increase of g, both $z_{w,\,max}$ and w_{01} decrease, however, insertion of a core-less fiber shifts the number to a higher value. The g value for fiber GIF625 is marked with a vertical line and intersections are marked with red circles. In Figure 3.12(b), focal distance for

a certain output beam waist ($w_{01} = 5\,\mu m$) is plotted at the left and minimum possible output beam waist (at $z_w \approx 0$) is plotted at the right. Addition of a core-less fiber can increase the focal distance and decrease the minimum spot size. Lastly, quarter pitch length of the lens as a function of g is illustrated in Figure 3.12(c). The pitch of the lens is the length required for a full sinusoidal oscillation of the propagating beam waist in the lens, e.g. a lens with a pitch of 0.25 (quarter pitch, $L_{1/4}$) has a length equal to $1/4$ of a sine wave, which would collimate a point source located at the surface of the lens. The pitch is an inherent property of the GRIN lens which doesn't change with input beam location, unlike the focal distance and output beam waist, which can also be seen from the plot. For the GIF625 fiber, the minimum length required to collimate a point source is $L_{1/4} \approx 200\,\mu m$, however, other lengths can also be use that satisfies the condition $(2m+1)L_{1/4}$ where $m = 0, 1, 2, \ldots$.

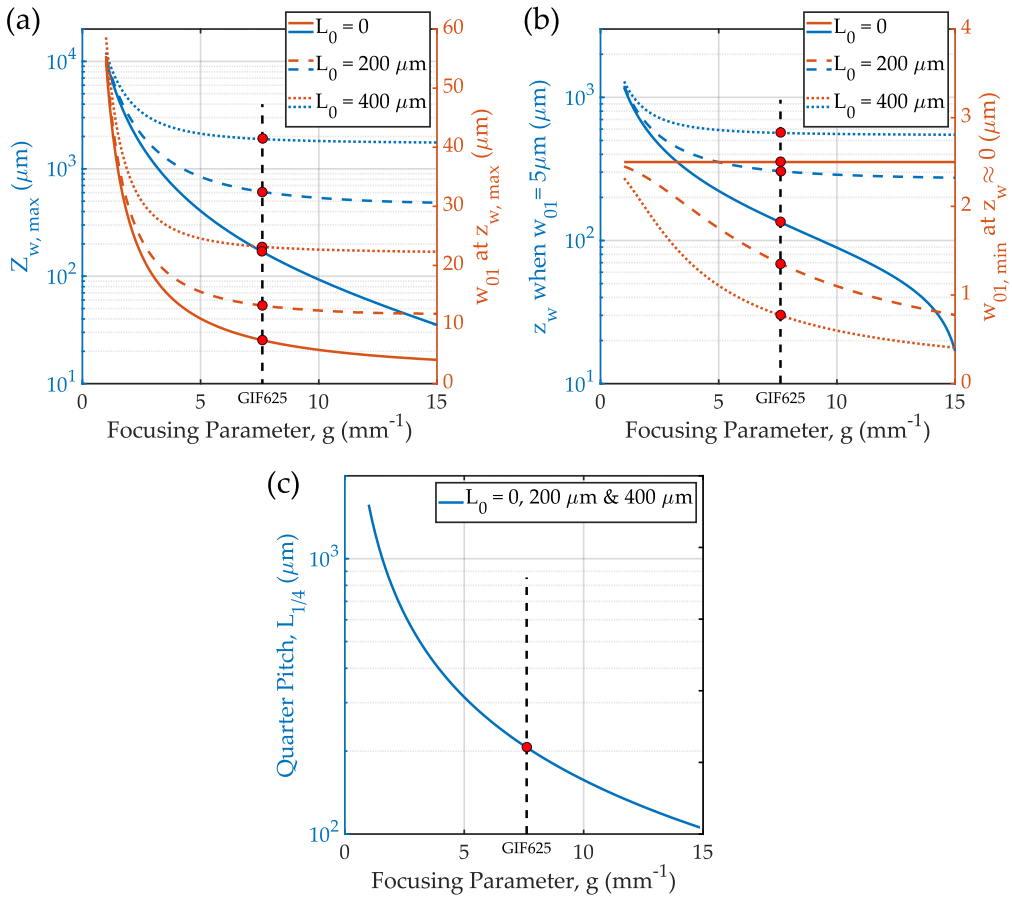

FIGURE 3.12: (a) Maximum possible focal distance $z_{w,\,max}$ and output beam waist at this focal distance w_{01} vs. focusing parameter g. Solid, dashed and dotted lines represent without core-less fiber, with $200\,\mu m$ and $400\,\mu m$ core-less fiber respectively. With the increase of g, both $z_{w,\,max}$ and w_{01} decrease, however, insertion of a core-less fiber shifts the number to a higher value. The focusing parameter for fiber GIF625 is marked with a vertical line ($g = 7.613\,mm^{-1}$) and intersections are marked with red circles. (b) Focal distance for $w_{01} = 5\,\mu m$ and minimum possible output beam waist (at $z_w \approx 0$) vs. g. More than half millimeter focal distance for 5 µm beam waist and sub-micron focal spot for very short focal distance is achievable. (c) Quarter pitch length $L_{1/4}$ vs. g. The pitch doesn't change with input beam location, i.e. with or without core-less fiber it remains unchanged.

3.5 Coupling (collection) efficiency analysis

The coupling efficiency for photons emitted from a nanowire being coupled to the fiber integrated GRIN lens can be written as:

$$\eta = \eta_{SG} \times \eta_{fres} \times \underbrace{\eta_{\alpha} \times \eta_{T} \times \eta_{V}}_{\eta_{OV}} \times \eta_{nw} \tag{3.13}$$

Where,

- η_{SG} : Coupling efficiency from SMF to GRIN fiber. The loss occurs if the core-less fiber length is such that the beam expands beyond the diameter of the GRIN fiber. However, this is often necessary to have a large diameter input beam at the GRIN fiber input for tight focusing at the output.
- η_{fres} : Fresnel reflection due to air-glass interface, which is $\sim 3.5\%$.
- η_{α} : Overlap integral between lens' beam waist and nanowire beam waist while they are on the same plane and possess the same optical axis.
- η_{T} : Efficiency loss due to transverse misalignment of the two beams.
- η_{V} : Efficiency loss due to vertical misalignment of the two beam waists. This misalignment can be due to GRIN fiber length precision and for photoresist thickness variation. For this application, the former has negligible effect, however, the latter might have some noticeable effect.

  η_{α}, η_{T} and η_{V} can be combined into the overlap integral with necessary modification.
- η_{nw} : Efficiency due to percentage of photons going upward, which is $\sim 50 - 55\%$ for the design parameters. However, using a reflective surface like gold at the bottom can increase it to near unity[21].

Fresnel reflection can be minimized by anti-reflection coating, however, considering the complexity over efficiency gain, it is not considered here. Nanowire upward transmission efficiency, η_{nw}, is dependent on the quantum dot nanowire growth. η_{SG} and η_{α} can be optimized by carefully designed fiber integrated GRIN lens. η_{T} and η_{V} can be optimized by developing high precision fabrication technique for fiber holding structure.

Overlap integral

The mode profile for both the nanowire and the GRIN fiber lens can be approximated as Gaussian profile. The electric field can be written as:

$$E(r,z) = E_0(z) \exp\left[-\left\{\frac{r-\Delta}{w(z)}\right\}^2\right] \exp\left[-i\frac{k(r-\Delta)^2}{2R(z)}\right] \exp[-i(kz-\omega t)] \tag{3.14}$$

$$\text{where,} \quad w(z) = w_0\sqrt{[1+(z/z_0)^2]} = \text{beam waist}$$

$$R(z) = z[1+(z_0/z)^2] = \text{radius of curvature}$$

Here, Δ = transverse misalignment and $E_0(z)$ is the z-dependent amplitude. The collection efficiency can be calculated using overlap integral and is given by the following formula:

$$\eta_{OV} = \frac{\left|\int_{-\infty}^{\infty} E_1(r,z)E_2^*(r,z)dr\right|^2}{\int_{-\infty}^{\infty} E_1(r,z)E_1^*(r,z)dr \int_{-\infty}^{\infty} E_2(r,z)E_2^*(r,z)dr} \tag{3.15}$$

Substituting equation 3.14 into equation 3.15 and performing the integral [67]:

$$\eta_{OV} = \frac{\eta_0}{\sqrt{1+\gamma}} \exp\left[-\left\{\frac{\frac{w_2(z)}{w_1(z)}\eta_0 + 2\gamma}{1+\gamma}\right\}\frac{\Delta^2}{w_2^2(z)}\right] \tag{3.16}$$

$$\text{where,} \quad \eta_0 = \frac{2w_1(z)w_2(z)}{w_1^2(z)+w_2^2(z)}$$

$$\gamma = \left[\frac{\pi n}{\lambda}\left\{\frac{1}{R_1(z)} + \frac{1}{R_2(z)}\right\}\right]^2 \left\{\frac{w_1(z)w_2(z)\eta_0}{2}\right\}^2$$

Here, $w_1(z)$, $R_1(z)$ = fiber beam parameters and $w_2(z)$, $R_2(z)$ = nanowire beam parameters, $n = n_{air} = 1$ is the refractive index of the medium.

For convenience, the nanowire beam can be assumed at its waist, i.e. $w_2(z) = w_{20}$ and $R_2(z) = \infty$. If the distance between GRIN fiber edge and w_{20} is z, and the distance between GRIN fiber edge and the focal plane is z_w, then equation 3.16 can be modified as:

$$\eta_{OV} = \frac{\eta_0}{\sqrt{1+\gamma}} \exp\left[-\left\{\frac{\frac{w_{20}}{w_1(z-z_w)}\eta_0 + 2\gamma}{1+\gamma}\right\}\frac{\Delta^2}{w_{20}^2}\right] \tag{3.17}$$

$$\text{where,} \quad \eta_0 = \frac{2\,w_1(z-z_w)\,w_{20}}{w_1^2(z-z_w)+w_{20}^2}$$

$$\gamma = \left[\frac{\pi\,\eta_0\,w_1(z-z_w)\,w_{20}}{2\,\lambda\,R_1(z-z_w)}\right]^2$$

When $z = z_w$, both the focal planes from fiber and nanowire overlap on the axial axis, and when $\Delta = 0$, they also maximally overlap on the transverse plane. In any case, equation 3.17 can be used to calculate the expected collection efficiency from quantum dot nanowire to fiber.

Extract nanowire beam (emitted photon) parameters

Emitted photons from the quantum dot nanowire can be approximated as a Gaussian beam. During the FDTD simulation, output beam intensity is measured at the near field at two different locations separated by a gap (d). Waist of the beam at these locations can be measured

and then the remaining beam parameters can be extracted as following:

$$w(z) = w_0\sqrt{\left[1 + (z/z_0)^2\right]}$$

$$w^2(z) = \frac{\lambda}{\pi}\left[z_0 + \frac{z^2}{z_0}\right] \quad \text{where,} \quad w_0 = \sqrt{\lambda z_0/\pi}$$

$$\therefore w^2(z_1) = w_1^2 = \frac{\lambda}{\pi}\left[z_0 + \frac{z_1^2}{z_0}\right] \quad \text{and} \quad w^2(z_1+d) = w_2^2 = \frac{\lambda}{\pi}\left[z_0 + \frac{(z_1+d)^2}{z_0}\right]$$

Assuming, $x = z_0, \quad y = z, \quad a = w_1^2\pi/\lambda, \quad b = w_2^2\pi/\lambda$

$$x^2 - ax + y^2 = 0 \tag{3.18a}$$

$$x^2 - bx + (y+d)^2 = 0 \tag{3.18b}$$

Solving equation 3.18 gives Rayleigh length ($z_{0,\,nw}$) and distance between waist and measurement plane (z_{nw}), also the waist ($w_{0,\,nw}$) can be obtained from $z_{0,\,nw}$. An example simulation setup and result is depicted in Figure 3.13. First monitor is placed 1 µm from the nanowire tip and second monitor is placed 10 µm from the tip. Beam waist at these two locations are calculated and then the beam parameters are extracted. In this calculation, the reference point ($z = 0$) is taken at the tip of the nanowire, and from the plot it is observed that the waist is located below the physical tip of the nanowire.

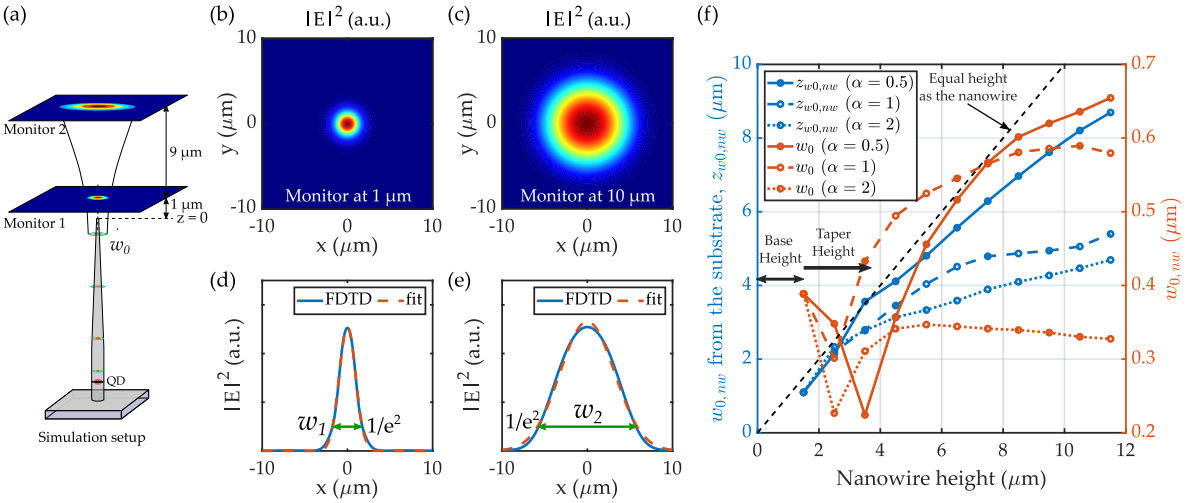

FIGURE 3.13: Nanowire beam parameter extraction. (a) simulation setup: two monitors placed above the nanowire tip, 1 µm and 10 µm from the tip. (b, c) Simulated intensity profile at monitor 1 and 2. (d, e) Intensity cross section at $y = 0$, from simulation and Gaussian fit. FWHM is shown with green arrow. (f) Nanowire emitted photon waist location $z_{w0,\,nw}$ and size $w_{0,\,nw}$ vs. nanowire height (base height + taper height) for different α. Black dashed line shows the condition $z_{w0,\,nw}$ = nanowire height.

GRIN Lens parameter library

A library of fiber lens' waist size at the focal plane and focal distance as a function of length of the core-less fiber and length of the GRIN fiber is proposed as illustrated in Figure 3.14 (for

fiber pair 780HP and GIF625). For better visualization, inverse of the waist is plotted. This library can be used for a quick search of the desired parameters. The length of the core-less fiber is limited up to 1000 µm because after this point the expanded beam waist in the core-less fiber compared to the radius of the GRIN fiber core is such that <30% of the power is contained at the GRIN fiber core. Four vertical dashed lines at [263 µm, 405 µm, 683 µm, 953 µm] show the limit for core-less fiber length below which more than [99%, 86%, 50%, 30%] power is contained in the core. The solid black line shows the minimum values of $w_{0,\,lens}$ (maximum in the plot due to inversion) against the core-less fiber length.

For efficient collection of the emitted photons, the fiber lens' focal plane has to be at the same location as $w_{0,\,nw}$ and the waist size $w_{0,\,lens}$ should be as close as possible. Once $w_{0,\,nw}$ is known, the library can be used to find the desired $w_{0,\,lens}$ and corresponding $L_{core-less}$ and L_{GRIN} can be obtained. Then using the library again z_w can be determined. For example, if the target is to design for $w_{0,\,nw} = w_{0,\,lens} = 1\,\mu m$, from the library $L_{core-less} \approx 300\,\mu m$ and $L_{GRIN} \approx 250\,\mu m$. However, there is a wide range of values to choose from for a particular $w_{0,\,lens}$.

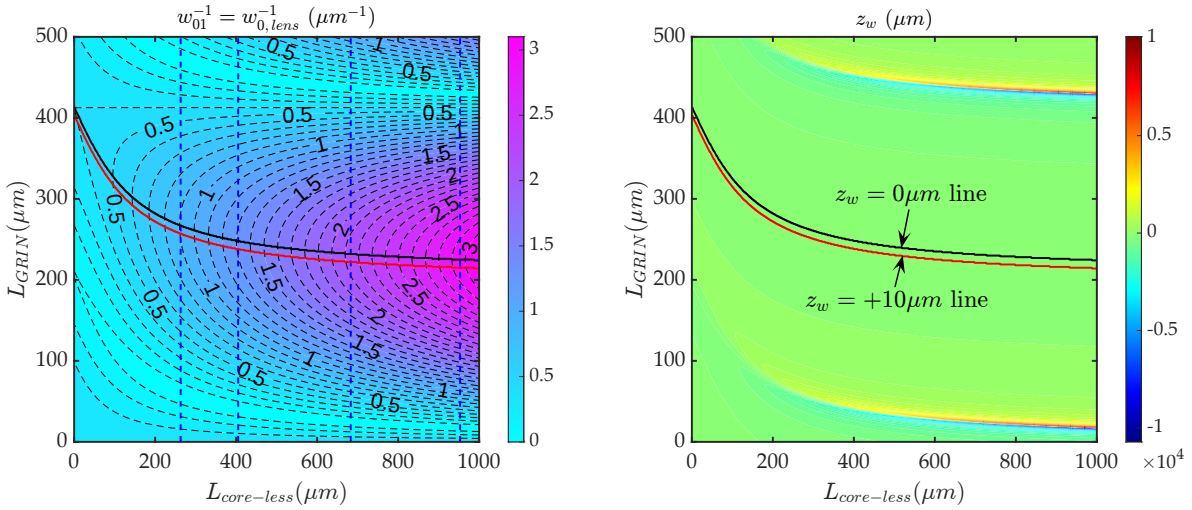

FIGURE 3.14: GRIN Lens parameter library for fiber pair 780HP and GIF625. $w_{0,\,lens}$ and z_w is illustrated as a function of length of the core-less fiber and GRIN fiber. For better visualization, inverse of the waist is plotted. Vertical dashed lines at [263 µm, 405 µm, 683 µm, 953 µm] show the limit for core-less fiber length below which more than [99%, 86%, 50%, 30%] power is contained in the core. Black solid line shows minimum $w_{0,\,lens}$ and $z_w = 0$ line. Red solid line shows $z_w = +10\,\mu m$ line.

η_{SG} and η_α optimization

At first glance it seems to maximize η_α by matching the waists of the nanowire and lens is the first priority to maximize the overall collection efficiency. However, as the nanowire beam waist is very small ($< 1\,\mu m$), trying to match it with fiber integrated lens' beam waist causes several practical issues that might cause the overall efficiency to go down. First of all, achieving very small waist at the lens output requires large diameter lens, which is constrained by the core diameter ($62.5\,\mu m$ for GIF625 or $100\,\mu m$ for F-MLD) of the GRIN lens. Secondly, if the input beam waist from the SMF to the GRIN fiber gets larger, tighter focus at

the output can be achieved at the cost of losing power by the core-cladding aperture. Which means η_α would be increased at the cost of decreasing η_{SG}. Thirdly, the structure would be very sensitive to fabrication variation and overall efficiency will decay very rapidly for small misalignment.

Considering the above mentioned practical issues, it is wise to maximize $\eta_{SG} \times \eta_\alpha$, rather than individual optimization. To do so, the following steps are followed:

1. Find the beam waist of the nanowire, $w_{0\,nw}$.
2. Find the closest match with the lens waist from the library. There might be several occurrences, however, it is looked up along the minimum $w_{0,\,lens}$ line (solid black line in $w_{0,\,lens}$ and z_w library). This is the point where $z_w = 0$. Therefore, corresponding lengths of the core-less fiber (L_{c0}) and GRIN fiber (L_{G0}) is known. L_{c0} generally is a large value ($> 500\,\mu m$) for the designed nanowire.
3. Starting from L_{c0}, the length of the core-less fiber is swept down to $250\,\mu m$ (an arbitrary value where $> 99\%$ power is coupled), while the length of the GRIN fiber is always $10\,\mu m$ smaller than the minimum $w_{0,\,lens}$ line (solid red line in $w_{0,\,lens}$ and z_w library).
4. η_α is found from equation 3.17 for the condition $\Delta = 0$ and $z = z_w$ and η_{SG} is found from:

$$\eta_{SG} = 1 - exp\left[-\frac{2\rho^2}{w^2(z)}\right] \tag{3.19}$$

   Here, ρ = radius of the GRIN fiber and $w(z)$ = input beam waist to the GRIN fiber corresponding to the length of the core-less fiber. The product of these two parameters, $\eta_{SG} \times \eta_\alpha$, is taken and the maximum point is selected.

An example is illustrated in Figure 3.15 where the maximum point is marked with red dot.

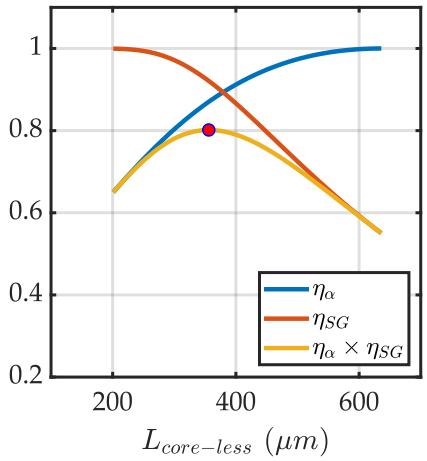

FIGURE 3.15: $\eta_{SG} \times \eta_\alpha$ optimization. As can be seen in the plot, instead of maximizing η_α or η_{SG} alone, maximizing their product, $\eta_{SG} \times \eta_\alpha$, yields higher efficiency. The maximum point is marked with red dot.

Overall collection efficiency

The expected overall collection efficiency can be found from equation 3.13 for $\eta_T = \eta_V = 1$, i.e. perfect alignment between nanowire and fiber. Different stages of overall coupling efficiency optimization is graphically illustrated in Figure 3.16(a-c) against the length of the nanowire. The expected overall efficiency can be as high as $\sim 40\%$. In Figure 3.16(d), the distance between GRIN fiber edge to the substrate is depicted. This is the height of the fiber holding structure. The dashed black line shows where the gap is equal to the nanowire height. The required length of the core-less fiber and GRIN fiber is illustrated in Figure 3.16(e-f) respectively.

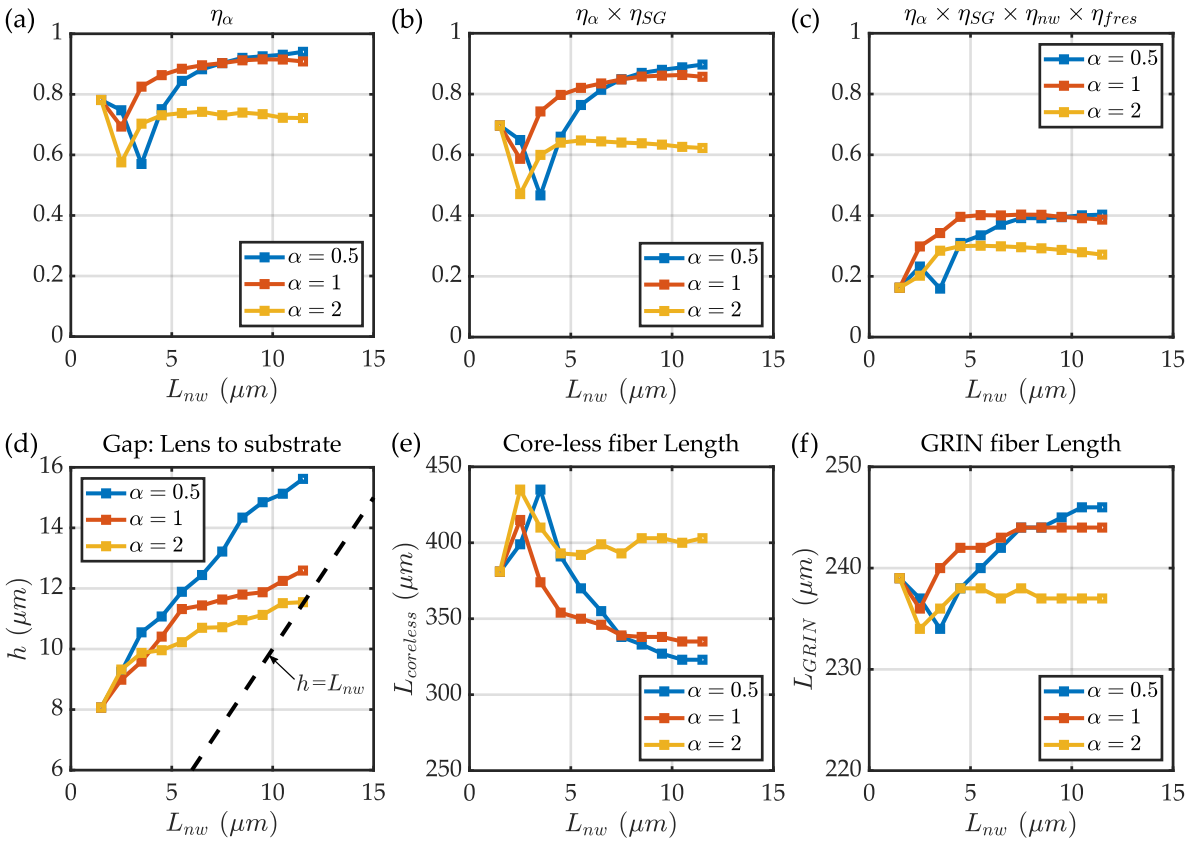

FIGURE 3.16: (a-c) Collection efficiency calculation steps for $\eta_T = \eta_V = 1$. Overall expected collection efficiency can be as high as $\sim 40\%$. (d) The distance between GRIN fiber edge to the substrate, which is the height of the fiber holding structure. The dashed black line shows the condition $h = L_{nw}$. (e, f) Length of the core-less fiber and GRIN fiber, respectively.

Fabrication variation consideration

Several types of fabrication variation can happen including length of the GRIN fiber or core-less fiber variation, height of the fiber holding structure deviation or transverse misalignment between optical axis of fiber and nanowire. The variation can be divided into

two categories: transverse misalignment and vertical misalignment, with the respective efficiency components η_T and η_V. To predict the fabrication variation effect on overall collection efficiency, the information on relative waist size between lens and nanowire ($w_{0,\,ratio} = w_{0,lens}/w_{0,nw}$) is necessary which can be obtained from the design parameters. The ratios for different nanowire lengths and α are depicted in Figure 3.17(a). As can be seen from the figure, the ratio lies between 1.5 to 2.5 for most parts. Including these values in equation 3.17 along with transverse (Δ_T) and vertical (Δ_V) misalignment can predict the effect of fabrication variation on η_α, which can then be used in equation 3.13 to predict the overall efficiency. Two sample calculations showing the effect of Δ_T and Δ_V on η_α for $w_{0,\,ratio}$ =1.5 and 2.5 are depicted in Figure 3.17(b-e). For smaller ratio, the maximum efficiency is higher, however, it decays rapidly. On the contrary, for larger ratio the situation is opposite. Also, due to the Gaussian nature of the beams and relatively small spot size, the efficiency is more tolerant to the vertical misalignment and very sensitive to the transverse misalignment. The design parameters should be adjusted depending on the achievable precision of the nano-fabrication.

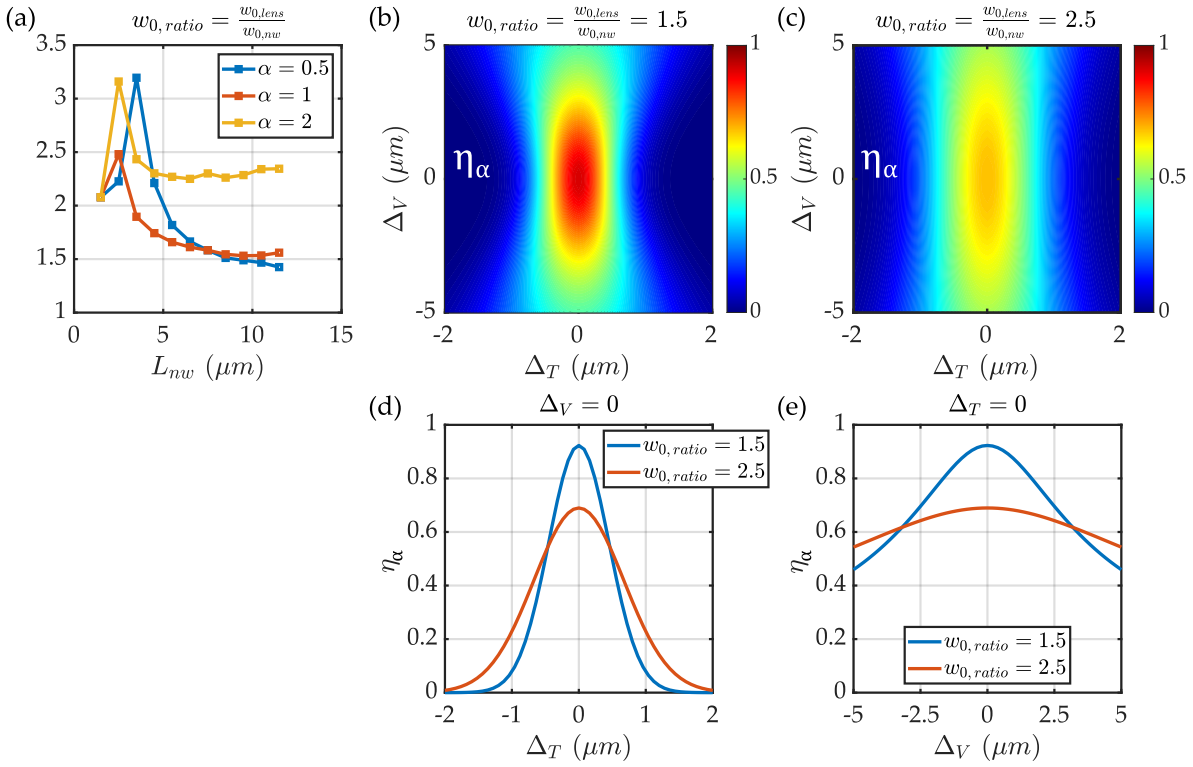

FIGURE 3.17: Fabrication variation effect on efficiency (η_α). (a) Relative waist size between fiber lens and nanowire, $w_{0,\,ratio} = w_{0,lens}/w_{0,nw}$. $w_{0,\,ratio}$ varies between 1.5 to 2.5 for most parts. (b, c) Variation in η_α due to transverse and vertical misalignment for $w_{0,\,ratio}$ =1.5 and 2.5. (d, e) Effect of transverse misalignment and vertical misalignment only. For smaller ratio, the maximum efficiency is higher, however, it decays rapidly. On the contrary, for larger ratio the situation is opposite. Due to the Gaussian nature of the beams and relatively small spot size, the efficiency is more tolerant to the vertical misalignment and very sensitive to the transverse misalignment.

3.6 Design protocol

The design parameters for quantum dot nanowire and fiber integrated lens and the expected photon collection efficiency is discussed in details in the previous segments. Using the results obtained, a complete design protocol is proposed below:

1. **Step 1:** Nanowire design

   Nanowire design procedure is discussed in section 3.4.1 and the steps involved in the procedure is listed below. The final parameters obtained are also given in the parentheses:

   (a) Material for nanowire (InP)
   (b) Nanowire diameter, usually single mode guiding (200 nm)
   (c) Nanowire base height (1.5 µm)
   (d) Quantum dot height, constructive interference is desired (408 nm)
   (e) Nanowire taper angle, Gaussian output profile is desired (α = [0.5°, 1°, 2°])
   (f) Nanowire taper height, Gaussian output profile is desired (few µm to ∼10 µm)

   The last two parameters are not fixed in the design due to fabrication constraints. Therefore, a range of values is considered to predict the fabrication variations and the summary result is illustrated in Figure 3.8.

2. **Step 2:** Extract nanowire beam (emitted photon) parameters

   As discussed in section 3.5.

3. **Step 3:** Fiber integrated lens parameters

   Length of the core-less fiber and GRIN fiber, using the library and the efficiency optimization from section 3.5.

4. **Step 4:** Quantum dot nanowire growth

5. **Step 5:** Examine the fabricated nanowire

   Cross-check the design dimensions and the fabricated nanowires, e.g. using SEM.

6. **Step 6:** Necessary modification in the fiber integrated lens parameters.

7. **Step 7:** Optimize fabrication technique

   For fiber integrated lens and fiber holding structure.

8. **Step 8:** Integrate the fiber lens and the quantum dot.

3.7 Fabrication outlook

The overall fabrication process can be divided into three segments: i) quantum dot nanowire growth ii) on-chip fiber alignment structure and iii) fiber integrated GRIN lens.

3.7.1 Quantum dot nanowire growth

Quantum dot embedded in semiconductor nanowire is grown by our collaborator in National Research Council of Canada. After we provide them the desired fabrication parameters, they can grow quantum dot nanowires as per specifications.

3.7.2 Fiber integrated GRIN lens

For the integration of SMF with core-less fiber with GRIN lens, at first a core-less fiber is spliced with a SMF (780HP) using Vytran glass processor and then the core-less fiber is cleaved at the desired length. For the splicing, electric arc discharge is used to melt the fiber tips and then pressure is applied to splice the fibers. The process is optimized for a smooth low-loss joint. For cleaving the core-less fiber at a desired length, the same tool is used for precision cleaving where the length precision of $\pm 5\,\mu m$ is achievable, which is adequate for the this application. Same procedure is repeated with GRIN multimode fiber (GIF625). A sample fabricated structure with SMF-GRIN fiber pair is illustrated in Figure 3.18.

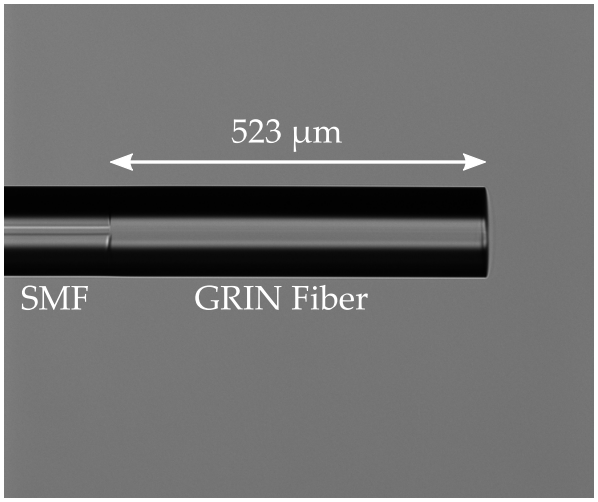

FIGURE 3.18: A GRIN fiber segment is spliced with a SMF.

3.7.3 On-chip fiber alignment structure

On-chip fiber alignment structure for quantum dot nanowire requires a two-step structure, the bottom step would hold the tip of the fiber at a certain distance from the tip of the nanowire (vertical alignment) and the top step would align the fiber axis with nanowire axis (transverse alignment). As the nanowire height is at the order of $\sim 10\,\mu m$, the fiber tip would be $10-20\,\mu m$ from the substrate. Apart from that, the top layer has to be significantly thick, at the order of $\sim 100\,\mu m$, to firmly hold the fiber. Though conventional photoresists yield micron range coating thickness, some photoresists like SU-8 or AZ series are capable of providing $10-100\,\mu m$ thickness in a single coat depending on the viscosity. For the two-step alignment structure, negative tone SU-8 photoresist is chosen as the resist material. For the bottom (thin) layer, low viscosity SU-8 3010 was used for $10\,\mu m$ thick layer. The pattern was exposed but not developed. For the top (thick) layer, high viscosity SU-8 50 was chosen as it can provide more than $100\,\mu m$ thick coating in a single step. Both layers were aligned using

alignment markers. After exposure of the second layer, the sample was developed. The technique used here is multi-layer exposure developed with a single development step, which provides several advantages [68]. First of all, the low viscous bottom layer would act as a protective layer for the nanowire during the processing of very high viscosity top layer. Secondly, due to the geometry of the structure, any other options like double exposure would make the process unnecessarily complicated. Anyway, the schematic of the fiber lens integrated nanowire structure and a bi-layer SU-8 alignment structure is depicted in Figure 3.19. The bi-layer structure has $10\,\mu m$ thick bottom and top layer, to show the proof of concept.

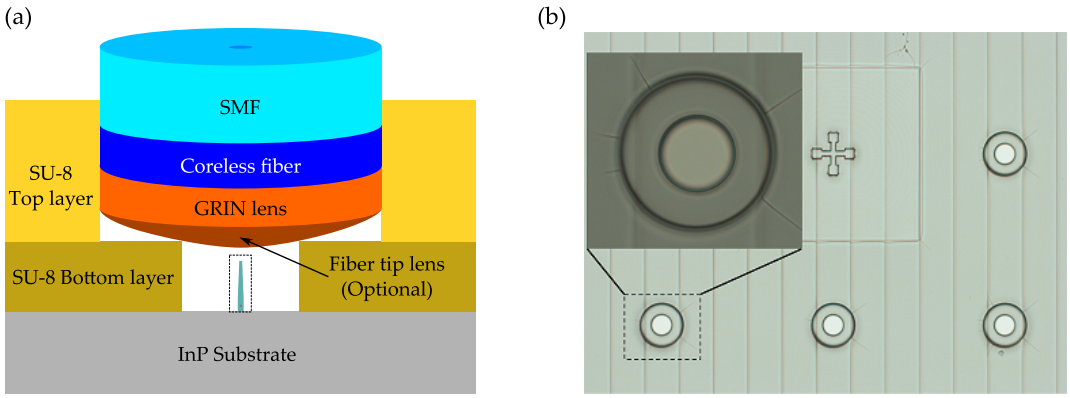

FIGURE 3.19: (a) Schematic of the fiber lens integrated nanowire structure. (b) Bi-layer SU-8 alignment structure, where $10\,\mu m$ thick bottom and top layer is used to show the proof of concept.

3.8 Conclusion and Outlook

In this work, we propose a complete design protocol for fiber coupled single photon source based on quantum dot embedded in a semiconductor nanowire. The expected overall collection efficiency to the SMF can be as high as 40%. Possible fabrication variations, their effect on the collection efficiency and necessary measures to minimize them was also discussed. We also report the fabrication progress towards the proof of concept device. Successful demonstration can be a significant improvement towards a fiber integrated single photon source.

Chapter 4

Solid state optical power limiter integrated with optical filter

4.1 Introduction

Photonic integrated circuits (PIC) are getting increased attention due to their ultrahigh speed, wide bandwidth and lower energy loss which has the potential to break some of the bottlenecks incurred by the present semiconductor-based electronic integrated circuits, including the well known interconnect issue. In addition to that, PICs also explore areas that were not previously probed by electronics, for example quantum-photonics based quantum cryptography. However, as we have a mature electronic industry based on CMOS platform and photonic integrated circuits are still in a relatively early stage, an inherent benchmark is to mimic or achieve an equal or better performance by PICs in practical cases. In recent years, many photonic integrated devices have been demonstrated as counterparts of the basic functionalities in electronic circuit, including all-optical logic gates [69], optical random access memory (RAM) [70, 71], optical comparator [72], optical differentiator [73–76], optical integrator [77–79], as well as all-optical ordinary differential equation (ODE) solvers [80–82]. Apart from the logic or mathematical operations, one of the important components being used in electronic circuits is the current limiter (to protect the circuitry from excess current), whose analog in photonics is the optical power limiter (OPL). The OPL is getting more and more attention in different areas of photonics. Of particular interest for us was the use of a power limiter as a tool to prevent so called 'blinding' attacks in a QKD system [3, 4]. Different schemes have been demonstrated for optical power limiting including use of third-order nonlinear material as a cavity layer in Bragg mirror cavity [26–28], cavities with phase-changing materials [29, 30], exploiting intensity induced thermal effect in silicon photonic crystal cavity [31] or in silicon micro-ring resonator [32].

The basic idea behind nonlinear cavity OPL or thermally induced size change OPL is the shift of resonance peak (usually red shift) with the increased intensity of the incoming light. In most cases, these devices should work fine to act as an optical limiter, however, there might be some instances where someone might maliciously intend to exploit the loophole in the limiting performance of the OPL. One way this can be done is to slightly red detune the pump signal, which will cause the red shift of the resonance peak, and slowly increase the wavelength at the same rate of the device's cavity resonance. At the same time, it would be possible to send another probe signal at the cavity resonance wavelength with high enough intensity to sabotage the device protected by the OPL. The possible attack on a single nonlinear cavity is illustrated in Figure 4.1. In quantum cryptography, hacking of the quantum protocol has been demonstrated by Lydersen et. al. and Makarov et. al. [3, 4] using high

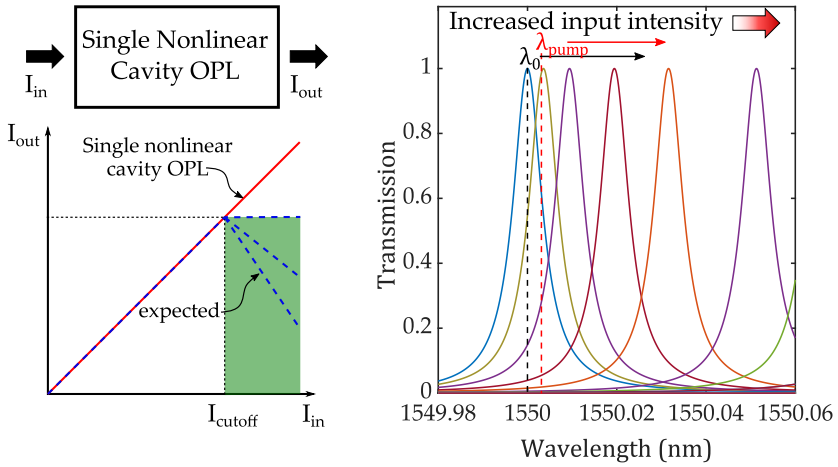

FIGURE 4.1: The possible attack on a device protected by a single nonlinear cavity OPL. Increasing the input intensity causes the cavity resonance (λ_0) to red shift (towards higher wavelengths). Therefore, one way to do this is to start with a slightly red detuned pump ($\lambda_{pump} > \lambda_0$) signal, which will cause a red shift of the cavity resonance peak, and then slowly increase the wavelength at the same rate of the device's cavity resonance. At the same time, send another probe signal at the cavity resonance wavelength with high enough intensity to sabotage the device protected by the OPL. A schematic plot of I_{out} vs. I_{in} of an OPL shows that even after the cut-off intensity, it's possible to send more light through the device consisting of a single nonlinear cavity. The desired region for I_{out} when I_{in}>I_{cutoff} is marked with green shaded region.

intensity laser light induced damage to the photo detectors. To protect devices against this kind of attack requires specially designed OPL. In this work we propose an OPL integrated with an optical filter that can limit the power without any loophole to send more power through the device.

4.2 Design

The proposed design is an integration of OPL and optical filter in the same device. The device is a three mirrors Fabry-Pérot interferometer with two cavities, one consists of linear material and the other one is made of nonlinear material. The nonlinear cavity acts as a power limiter and the linear cavity acts as the filter. The mathematical model for this device is presented in the following section.

4.2.1 Theory

We start with the analysis of a two mirrors cavity and then extend our analysis to the three mirrors cavity system. Assume that we have a cavity enclosed by two partially transparent mirrors as illustrated in Figure 4.2. E_i^+ is the amplitude of the electric field vector on the left-hand side of mirror i for a field propagating to the right, E_i^- is the amplitude on the left-hand side of mirror i for a field traveling to the left, r_i and t_i are the amplitude reflection and transmission coefficients for mirror i, the distance between mirror i to mirror $(i+1)$ is L_i

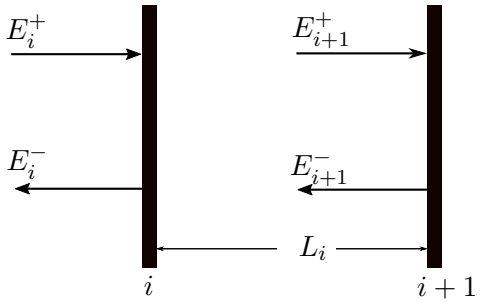

FIGURE 4.2: **E** field amplitude in a two mirror cavity.

and the corresponding phase length is $\Phi_i = 2\pi L_i/\lambda$. Assuming no absorption or scattering and using the Stoke's relation, we can write the relation among the electric fields as [83]:

$$
\begin{aligned}
E_{i+1}^+ e^{-i\Phi_i} &= t_i E_i^+ + r_i E_{i+1}^- e^{+i\Phi_i} \\
E_i^+ &= \frac{1}{t_i} E_{i+1}^+ e^{-i\Phi_i} - \frac{r_i}{t_i} E_{i+1}^- e^{+i\Phi_i} && \text{(rearranging)} \qquad (4.1) \\
&and \\
E_i^- &= -r_i E_i^+ + t_i E_{i+1}^- e^{+i\Phi_i} \\
E_i^- &= -\frac{r_i}{t_i} E_{i+1}^+ e^{-i\Phi_i} + \frac{r_i^2}{t_i} E_{i+1}^- e^{+i\Phi_i} + t_i E_{i+1}^- e^{+i\Phi_i} && \text{(substituting } E_i^+\text{)} \\
E_i^- &= -\frac{r_i}{t_i} E_{i+1}^+ e^{-i\Phi_i} + \frac{r_i^2 + t_i^2}{t_i} E_{i+1}^- e^{+i\Phi_i} \\
E_i^- &= -\frac{r_i}{t_i} E_{i+1}^+ e^{-i\Phi_i} + \frac{1}{t_i} E_{i+1}^- e^{+i\Phi_i} && \text{(Stoke's relation)} \qquad (4.2)
\end{aligned}
$$

Rearranging the equations 4.1 and 4.2 in matrix form:

$$
\begin{bmatrix} E_i^+ \\ E_i^- \end{bmatrix} = 1/t_i \begin{bmatrix} e^{-i\Phi_i} & -r_i e^{+i\Phi_i} \\ -r_i e^{-i\Phi_i} & e^{+i\Phi_i} \end{bmatrix} \begin{bmatrix} E_{i+1}^+ \\ E_{i+1}^- \end{bmatrix}
$$

In a more general case, for a series of N mirrors:

$$
\begin{aligned}
\begin{bmatrix} E_1^+ \\ E_1^- \end{bmatrix} = \frac{1}{t_1 t_2 \dots t_{N-1}} &\begin{bmatrix} e^{-i\Phi_1} & -r_1 e^{+i\Phi_1} \\ -r_1 e^{-i\Phi_1} & e^{+i\Phi_1} \end{bmatrix} \begin{bmatrix} e^{-i\Phi_2} & -r_2 e^{+i\Phi_2} \\ -r_2 e^{-i\Phi_2} & e^{+i\Phi_2} \end{bmatrix} \dots \\
&\begin{bmatrix} e^{-i\Phi_{N-1}} & -r_{N-1} e^{+i\Phi_{N-1}} \\ -r_{N-1} e^{-i\Phi_{N-1}} & e^{+i\Phi_{N-1}} \end{bmatrix} \begin{bmatrix} E_N^+ \\ E_N^- \end{bmatrix} \qquad (4.3)
\end{aligned}
$$

$$
\begin{bmatrix} E_1^+ \\ E_1^- \end{bmatrix} = \frac{1}{t_1 t_2 \dots t_{N-1}} \begin{bmatrix} A & B \\ C & D \end{bmatrix} \begin{bmatrix} E_N^+ \\ E_N^- \end{bmatrix} \qquad (4.4)
$$

To determine the amplitude transmission of such a stack of N mirrors, where there is only outgoing field and no incoming field, the equation can be modified as:

$$\begin{bmatrix} E_1^+ \\ E_1^- \end{bmatrix} = \frac{1}{t_1 t_2 \dots t_{N-1} t_N} \begin{bmatrix} A & B \\ C & D \end{bmatrix} \begin{bmatrix} E_{N+1}^+ \\ 0 \end{bmatrix} \tag{4.5}$$

$$\begin{aligned} t &= \frac{E_{N+1}^+}{E_1^+} \\ &= \frac{t_N E_N^+}{E_1^+} \\ &= \frac{t_1 t_2 \dots t_{N-1} t_N E_N^+}{A E_N^+ + B E_N^-} && \text{(substituting } E_1^+ \text{ from 4.4)} \\ &= \frac{t_1 t_2 \dots t_{N-1} t_N}{A + B E_N^- / E_N^+} \\ &= \frac{t_1 t_2 \dots t_N}{A - r_N B} \end{aligned} \tag{4.6}$$

Two mirror single cavity

The amplitude and intensity transmission coefficient can be written from equations 4.3, 4.4 and 4.6 as:

$$t = \frac{t_1 t_2}{e^{-i\Phi_1} + r_1 r_2 e^{+i\Phi_1}}$$

$$T = tt^* = \frac{t_1^2 t_2^2}{1 + r_1^2 r_2^2 + 2 r_1 r_2 \cos(2\Phi_1)}$$

The transmission through the cavity is depicted in Figure 4.3 for two cases:

i) $r_1 = r_2$: as we can see from the figure, increasing values of $r_1 = r_2$ yield narrower linewidth or high-Q cavity.

ii) $r_1 \neq r_2$: maximum transmission decreases from 1.

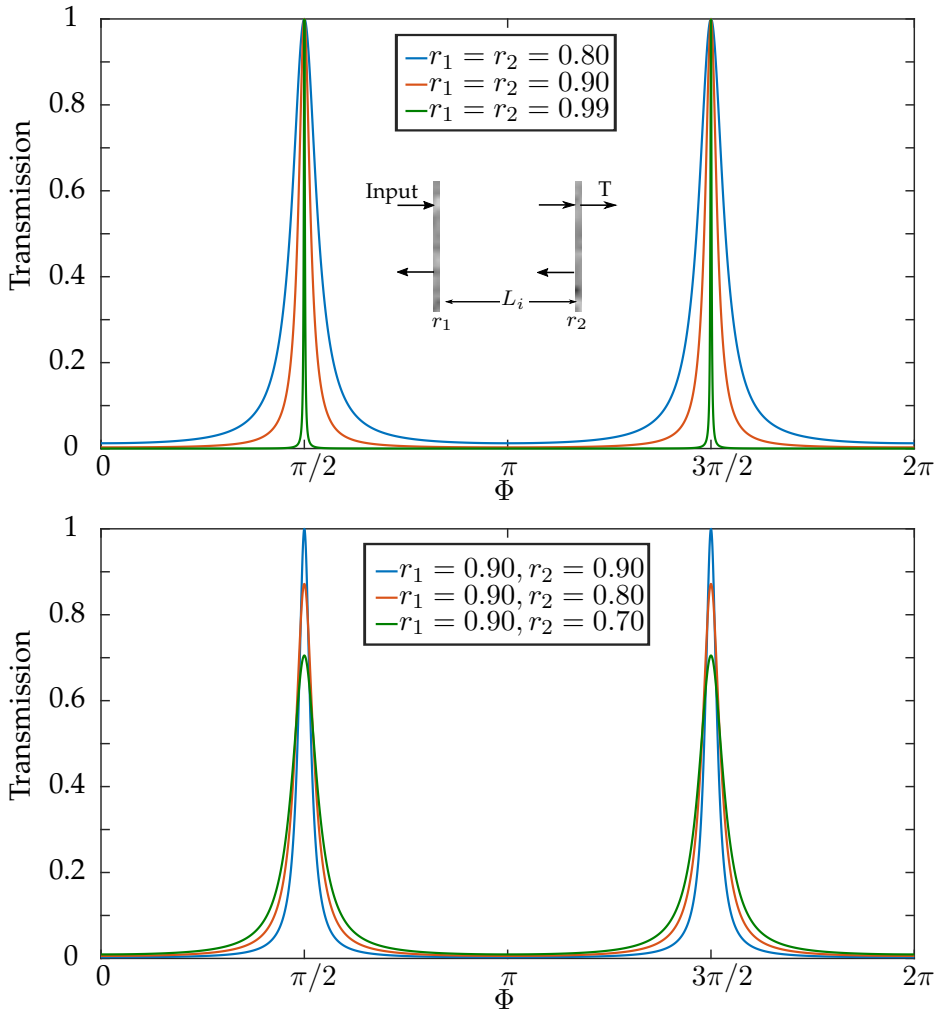

FIGURE 4.3: Transmission for single cavity enclosed by two mirrors. $R = r^2$, $T = t^2$. (top) $r_1 = r_2$: increasing values of $r_1 = r_2$ yield narrower linewidth or high-Q cavity. (bottom) $r_1 \neq r_2$: maximum transmission decreases from 1.

Three mirror double cavity

The amplitude and intensity transmission coefficient can be written from 4.3, 4.6 as:

$$t = \frac{t_1 t_2 t_3}{e^{-i\Phi_1 - i\Phi_2} + r_1 r_2 e^{+i\Phi_1 - i\Phi_2} + r_2 r_3 e^{-i\Phi_1 + i\Phi_2} + r_1 r_3 e^{+i\Phi_1 + i\Phi_2}}$$

$$T = tt^* = \frac{(t_1 t_2 t_3)^2}{\begin{array}{r} 1 + (r_1 r_2)^2 + (r_2 r_3)^2 + (r_1 r_3)^2 \\ +2r_1 r_2(1 + r_3^2)\cos(2\Phi_1) + 2r_2 r_3(1 + r_1^2)\cos(2\Phi_2) \\ + 2r_1 r_3 \cos(2\Phi_1 + 2\Phi_2) + 2r_1 r_2^2 r_3 \cos(2\Phi_1 - 2\Phi_2) \end{array}} \tag{4.7}$$

Depending on different values of r (amplitude coefficients are r, t and intensity coefficients are R, T) and Φ, there can be many cases. Here we demonstrate the cases relevant to this work.

i) Case 1: $r_1 = r_2 = r_3 = r$ and $\Phi_1 = \Phi_2 = \Phi$: For this condition, 4.7 can be simplified as:

$$T = \frac{(1 - r^2)^3}{(1 - r^2)^3 + [r(1 + r^2) + 2r\cos(2\Phi)]^2} \tag{4.8}$$

In this case, as depicted in Figure 4.4 (a), the transmission peak splits into two peaks compared to the single cavity case and $T_{max} = 1$.

ii) Case 2: $r_1 = r_3 \neq r_2$ and $\Phi_1 = \Phi_2 = \Phi$: For this condition, 4.7 can be simplified as:

$$T = \frac{(1 - r_1^2)^2(1 - r_2^2)}{(1 - r_1^2)^2(1 - r_2^2) + [r_2(1 + r_1^2) + 2r_1\cos(2\Phi)]^2} \tag{4.9}$$

For the condition of $R_2 = 4R_1/(1+R_1)^2$, transmission profile has a single peak and $T_{max} = 1$. For $R_2 < 4R_1/(1 + R_1)^2$, transmission profile has two peaks and $T_{max} = 1$. For $R_2 > 4R_1/(1 + R_1)^2$, transmission profile has a single peak and $T_{max} < 1$. These three conditions are illustrated in Figure 4.4 (b).

iii) Case 3: $r_1 = r_3 \neq r_2$ and $\Phi_1 \neq \Phi_2$: For this condition, 4.7 can be simplified as:

$$T = \frac{(1 - r_1^2)^2(1 - r_2^2)}{\begin{array}{r} 1 + 2r_1^2 r_2^2 + r_1^4 + 2r_1 r_2(1 + r_1^2)[\cos(2\Phi_1) + \cos(2\Phi_2)] \\ + 2r_1^2\cos(2\Phi_1 + 2\Phi_2) + 2r_1^2 r_2^2 \cos(2\Phi_1 - 2\Phi_2) \end{array}} \tag{4.10}$$

Equation 4.10 is illustrated in Figure 4.4 (c) for a set of values of R_1, R_2 and R_3 but varying the ratio of Φ_2/Φ_1. For $\Phi_2 = \Phi_1$ we get a single peak and maximum transmission equal to 1. However, for other values of Φ_2, the peak starts to split and the maximum transmission decreases below 1.

We can combine case 2 and case 3 to our advantage in the following manner. We can design the three mirror cavity for a set of ($R_1 = R_2 \neq R_3$) and ($\Phi_1 = \Phi_2$) such that the transmission has single peak and $T_{max} = 1$. However, if we put a $\chi^{(3)}$ nonlinear material in one of the cavities, the refractive index (n) of that cavity will be intensity dependent. If the intensity goes above a certain threshold, n will change, which means one of the single-pass propagation phases will change, and the T_{max} will continue to decrease with the increase of intensity.

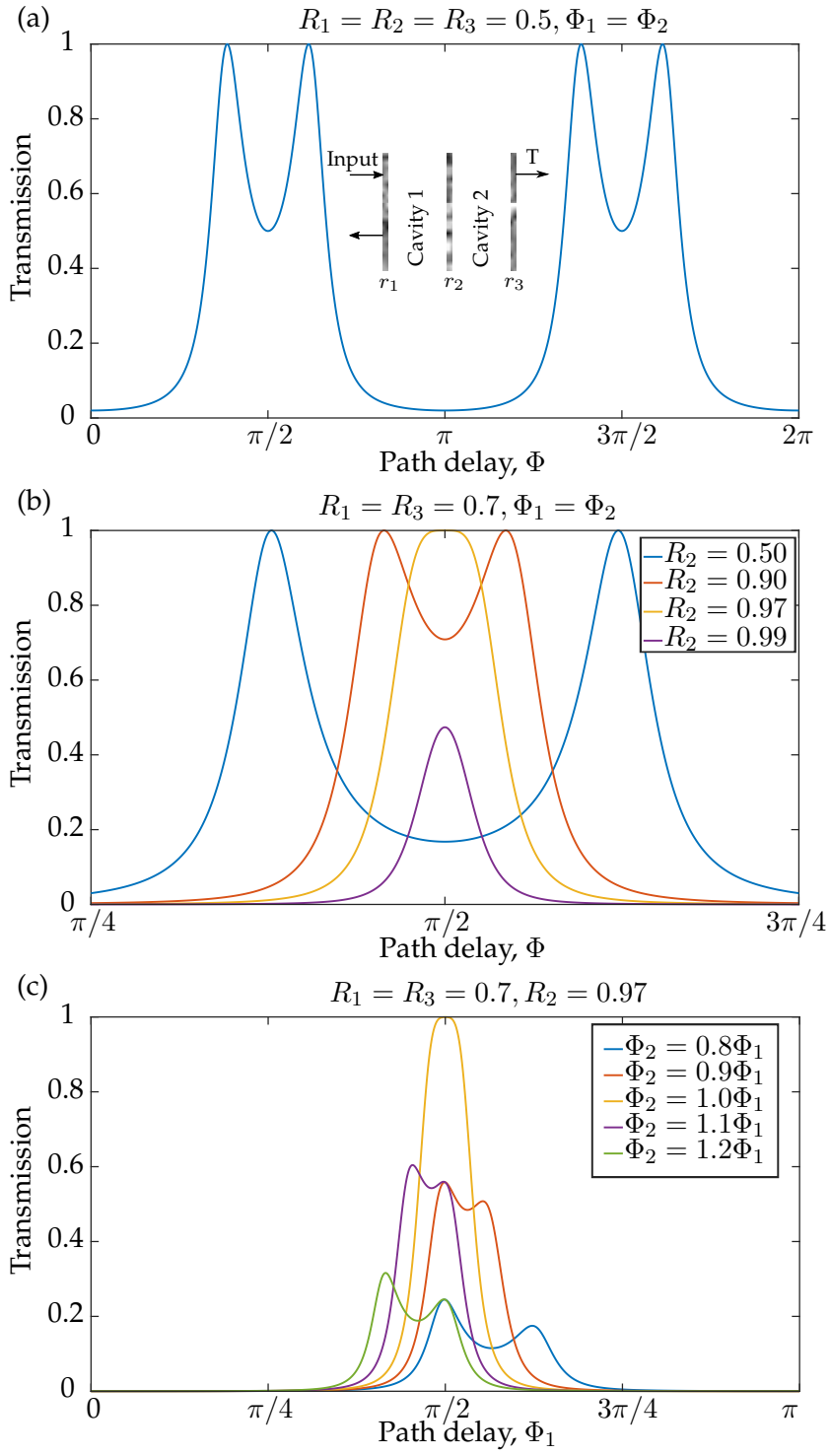

FIGURE 4.4: Transmission for double cavity enclosed by three mirrors. $R = r^2$, $T = t^2$. (a) Case 1: $R_1 = R_2 = R_3$ and $\Phi_1 = \Phi_2$: The transmission peak splits into two peaks compared to the single cavity case and $T_{max} = 1$. (b) Case 2: $R_1 = R_3 \neq R_2$ and $\Phi_1 = \Phi_2$: For a particular value of $R_2 = 4R_1/(1+R_1)^2$, transmission is single peak and $T_{max} = 1$. For $R_2 < 4R_1/(1+R_1)^2$, transmission has two peaks and $T_{max} = 1$. For $R_2 > 4R_1/(1+R_1)^2$, transmission has a single peak and $T_{max} < 1$. (c) Case 3: $R_1 = R_3 \neq R_2$ and the ratio of Φ_2/Φ_1 is varied: For $\Phi_2/\Phi_1 = 1$, transmission is single peak and $T_{max} = 1$. For other values of Φ_2/Φ_1, transmission starts to split and $T_{max} < 1$.

4.3 Background on nonlinear refractive index

If an external electric field ($\mathbf{E}$) is incident upon a dielectric material, it causes the bound charges (electrons and nuclei) inside the material to slightly separate and induce a local electric dipole moment. The total electric field inside the material under external field is defined as:

$$\mathbf{D} \equiv \varepsilon_0 \mathbf{E} + \mathbf{P} \tag{4.11}$$

Here, $\mathbf{D}$ is the electric displacement field, ε_0 is the vacuum permittivity and $\mathbf{P}$ is the polarization density. The polarization density is defined as:

$$\mathbf{P} = \varepsilon_0 \boldsymbol{\chi} \cdot \mathbf{E} \tag{4.12}$$

Here, $\boldsymbol{\chi}$ is the electric susceptibility of the medium which is a complex number tensor for the anisotropic medium, the most general case. The symbol "$\cdot$" is the tensor product. When the intensity of the incident field is strong (this is a relative term, depends on the material under consideration), the polarization does not always depend linearly on the field, rather some nonlinear phenomena is observed. In general, the electric polarization can be expanded into a power series to account for the linear and nonlinear response to the field:

$$\mathbf{P} = \varepsilon_0 \boldsymbol{\chi}^{(1)} \cdot \mathbf{E} + \varepsilon_0 \boldsymbol{\chi}^{(2)} : \mathbf{EE} + \varepsilon_0 \boldsymbol{\chi}^{(3)} \vdots \mathbf{EEE} + \cdots \tag{4.13}$$

Here, $\boldsymbol{\chi}^{(1)}$ is the linear susceptibility and $\boldsymbol{\chi}^{(2)}$ and $\boldsymbol{\chi}^{(3)}$ are the second and third order nonlinear susceptibilities, respectively. Higher order terms are not shown here. The symbols "$\cdot$", "$:$" and "$\vdots$" are second, third and fourth rank tensors, respectively. For a homogeneous isotropic medium, $\boldsymbol{\chi}$ can be assumed as a scalar quantity, $\mathbf{P}$ and $\mathbf{E}$ as vector quantities and the equation simplifies to:

$$\mathbf{P} = \varepsilon_0 \chi^{(1)} \mathbf{E} + \varepsilon_0 \chi^{(2)} |\mathbf{E}| \mathbf{E} + \varepsilon_0 \chi^{(3)} |\mathbf{E}|^{\mathbf{2}} \mathbf{E} + \cdots \tag{4.14}$$

Substituting equation 4.14 in equation 4.11 yields:

$$\begin{aligned} \mathbf{D} &= \varepsilon_0 \mathbf{E} + \varepsilon_0 \chi^{(1)} \mathbf{E} + \varepsilon_0 \chi^{(2)} |\mathbf{E}| \mathbf{E} + \varepsilon_0 \chi^{(3)} |\mathbf{E}|^{\mathbf{2}} \mathbf{E} + \cdots \\ &= \varepsilon_0 \left(1 + \chi^{(1)} + \chi^{(2)} |\mathbf{E}| + \chi^{(3)} |\mathbf{E}|^{\mathbf{2}} + \cdots \right) \mathbf{E} \\ &= \varepsilon_0 \left(1 + \chi^{(1)} \right) \mathbf{E} + \varepsilon_0 \left(\chi^{(2)} |\mathbf{E}| + \chi^{(3)} |\mathbf{E}|^{\mathbf{2}} + \cdots \right) \mathbf{E} \end{aligned} \tag{4.15}$$

Here, the first term is the linear response of the material proportional to the applied electric field and the second term is all the nonlinear responses combined together. The susceptibility in general is a function of frequency and is a complex number.

For the linear materials, the complex permittivity can be written as (single prime (‘) is for real part, double prime (‘’) is for imaginary part and (˜) is for complex number):

$$\begin{aligned}\tilde{\varepsilon} &= \varepsilon_0 \left[1 + \chi^{(1)}(\omega)\right] \\ &= \varepsilon_0 \left[1 + \chi^{(1)'}(\omega) + i\chi^{(1)''}(\omega)\right] \\ &= \varepsilon_0 \left[\varepsilon_r'(\omega) + i\varepsilon_r''(\omega)\right] \\ &= \varepsilon_0 \varepsilon_r(\omega)\end{aligned} \tag{4.16}$$

Where $\varepsilon_r(\omega)$ is the relative permittivity of the material. From now on, the ω will be omitted unless otherwise stated. The complex refractive index is defined as:

$$\tilde{n} = n + i\kappa = \sqrt{\frac{\tilde{\varepsilon}}{\varepsilon_0}} = \sqrt{\varepsilon_r} = \sqrt{\varepsilon_r' + i\varepsilon_r''} \tag{4.17}$$

Where, n and κ is generally referred as refractive index and extinction coefficient, respectively. If we ignore the extinction coefficient (lossless material) and denote the real part of the refractive index by n_0, then the linear refractive index of the material is:

$$n = n_0 = \sqrt{\varepsilon_r'} = \sqrt{1 + \chi^{(1)'}} \tag{4.18}$$

For the nonlinear materials, a wide range of nonlinear optical effects are possible depending on the material properties and electric field strength. A few examples are listed below:

- *Optical Kerr effect (mainly depends on $\chi^{(3)}$):* the refractive index of the material changes as a function of field intensity.
- *Nonlinear absorption (mainly depends on $\chi^{(3)}$):* absorption in the material depends on the field intensity, and can increase or decrease with the increase of intensity depending on the material.
- *Multiwave mixing (mainly depends on $\chi^{(2)}$ and $\chi^{(3)}$):* two or more incident fields can generate new field(s) with a frequency that was not in the original fields, but is a linear combination of the original fields.
- *Stimulated Raman scattering (mainly depends on $\chi^{(3)}$):* a laser beam enters the medium and interacts with the molecules of the medium to generate a series of scattered light at different frequencies by stimulated radiation.
- *Optical bistability (mainly depends on $\chi^{(3)}$):* when a laser beam with the intensity I_{in} enters a Fabry-Pérot cavity containing a nonlinear medium, it can produce two possible transmitted light intensities I_{out1} and I_{out2}. The characteristic curve is a hysteresis loop curve, and the output depends on the path the input light was following.
- *Nonlinear optical limiting:* when a laser beam passes through an optical device containing a nonlinear material, its transmittance may decreases with increase of optical intensity. When the output intensity decreases with the increase of input intensity, it can act as an optical limiter device.
- *All-optical switch (mainly depends on $\chi^{(3)}$):* when one optical signal is used to control another optical signal, it can act as a switch. However, having no charge, photons can

not interact with each other directly and need a medium. Nonlinear materials are used as the medium using which photons can interact.

In this work, we are only interested in the optical Kerr effect where nonlinear refractive index is dependent on the input intensity. Therefore it's worthwhile to explore this phenomena in more details. The Kerr effect can be divided into two types: i) self-phase modulation: a single frequency high power signal enters into the medium and changes the refractive index relying on its own intensity, ii) cross-phase modulation: a weak power signal light together with a high power pump light both enter the nonlinear medium, the pump light generates the optical Kerr effect and drives the refractive index change of the medium, and thus induces the phase modulation of the signal light. For the application under consideration, the former is relevant.

4.3.1 Nonlinear refractive index

In self phase modulation, a strong signal light enters into the nonlinear medium. Assuming a non-lossy medium and considering only the first order linear and third order nonlinear polarization:

$$\begin{aligned}\mathbf{P} &= \mathbf{P}^{(1)} + \mathbf{P}^{(3)} \\ &= \varepsilon_0 \chi^{(1)'} \mathbf{E} + 3\varepsilon_0 \chi^{(3)'} |\mathbf{E}|^2 \mathbf{E}\end{aligned} \tag{4.19}$$

Here, the factor 3 is the degeneration factor, further details can be found in section 2.2.2 of [84]. The dielectric coefficient and refractive index of the material can be written as:

$$\begin{aligned}\varepsilon &= \varepsilon_0 \left(1 + \chi^{(1)'} + 3\chi^{(3)'} |\mathbf{E}|^2\right) \\ n &= \sqrt{\varepsilon/\varepsilon_0} = \left[1 + \chi^{(1)'} + 3\chi^{(3)'} |\mathbf{E}|^2\right]^{1/2} \\ n &= \left[n_0^2 + 3\chi^{(3)'} \frac{2I}{c\,\varepsilon_0 n_0}\right]^{1/2} \quad \text{where, } n_0 = \sqrt{1+\chi^{(1)'}} \text{ and } I = \frac{1}{2} c\,\varepsilon_0 n_0 |\mathbf{E}|^2 \\ &= n_0 \left[1 + \frac{6\chi^{(3)'}}{c\,\varepsilon_0 n_0^3} I\right]^{1/2}\end{aligned} \tag{4.20}$$

In the second term of the equation, the numerator is much smaller than the denominator and from Taylor series expansion only the first two terms are sufficient:

$$\begin{aligned} n = n_0 \left[1 + \frac{6\chi^{(3)'}}{c\,\varepsilon_0 n_0^3} I\right]^{1/2} &\approx n_0 \left[1 + \frac{1}{2}\frac{6\chi^{(3)'}}{c\,\varepsilon_0 n_0^3} I\right] = n_0 + \frac{3\chi^{(3)'}}{c\,\varepsilon_0 n_0^2} I \\ = n_0 + n_2 I \quad \text{where,} \quad n_2 &= \frac{3\chi^{(3)'}}{c\,\varepsilon_0 n_0^2} \\ &\boxed{n = n_0 + n_2 I}\end{aligned} \tag{4.21}$$

Because of the nonlinearity, the phase of the field inside the medium can be written as:

$$\phi = \phi_0 + \Delta\phi = k_0 z + \Delta k z = \frac{2\pi z}{\lambda_0} n_0 + \frac{2\pi z}{\lambda_0} n_2 I$$
$$\boxed{\Delta\phi = \frac{2\pi z}{\lambda_0} n_2 I} \tag{4.22}$$

4.4 Optical power limiter integrated with optical filter: with two Fabry-Pérot cavities using Bragg Mirror

The above mentioned design methodology can be implemented using a Bragg mirror based cavity. By controlling the number of layers in the Bragg mirror, the required reflectivity condition can be met. The schematic of the device is depicted in Figure 4.5. We employ three materials: one low-index material and one high-index material for the alternating layers, and a high-index nonlinear material as spacer in the nonlinear cavity. In this chapter, we assume GaAs as the nonlinear material, due to its availability and good optical nonlinearity ($n_2 = 3.3 \times 10^{-13} m^2/W$), but other materials could work as well. The number of periods in the mirrors are (N_1+0.5), N_2 and (N_3+1) which corresponds to reflectivity R_1, R_2 and R_3. The layers are quarter wavelength stacks, and the cavities are one wavelength wide. For normally incident plane wave, a transfer function for this geometry can be found using transfer matrix method as following:

$$T_{total} = T_{02} T^{N_1} T_2 T_{23} T_3 T_{32} T^{N_2} T_2^4 T_{21} T_1 T_{12} T^{N_3} T_2 T_{20} \tag{4.23}$$

$$where,\ T = T_2 T_{21} T_1 T_{12}$$
$$T_{ij} = \frac{1}{t_{ij}} \begin{bmatrix} 1 & r_{ij} \\ r_{ij} & 1 \end{bmatrix}; \quad r_{ij} = \frac{n_i - n_j}{n_i + n_j},\ t_{ij} = \frac{2n_i}{n_i + n_j}$$
$$T_m = \begin{bmatrix} e^{ik_m z} & 0 \\ 0 & e^{-ik_m z} \end{bmatrix}; \quad k_m = \frac{2\pi n_m}{\lambda}$$

Matrix T_{ij} refers to the crossing of interface between two refractive indices, matrix T_m refers to the propagation in a single layer, and r_{ij} and t_{ij} are the amplitude reflection and

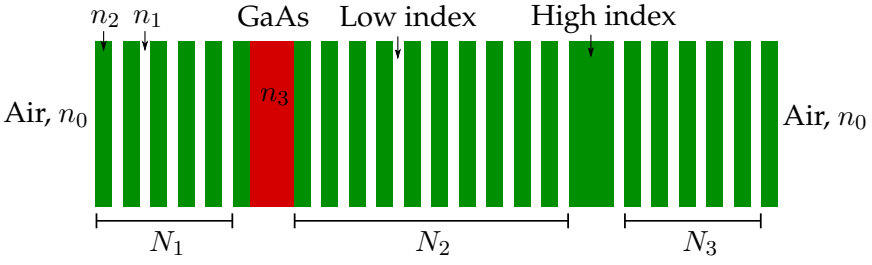

FIGURE 4.5: Schematic of two Fabry-Pérot cavities using Bragg Mirror.

transmission coefficient respectively. Using corresponding matrices in equation 4.23 and doing some algebra:

$$T_{total} = \frac{-i}{2\, n_2\, a^{N_1+N_2+N_3+1}} \begin{bmatrix} p + n_2^2 q & -p + n_2^2 q \\ p - n_2^2 q & -p - n_2^2 q \end{bmatrix} \tag{4.24}$$
$$where,\ a = \frac{n_1}{n_2},\ p = a^{2(N_1+N_3+1)},\ q = a^{2N_2}$$

The intensity reflection coefficient R is:

$$R = \left| \frac{p - n_2^2 q}{p + n_2^2 q} \right|^2 = \left| \frac{(p/q) - n_2^2}{(p/q) + n_2^2} \right|^2 \tag{4.25}$$

For T = 1, R = 0:

$$\begin{aligned} \frac{p}{q} &= n_2^2 \\ a^{2(N_1-N_2+N_3+1)} &= n_2^2 \\ 2(N_1 - N_2 + N_3 + 1) &= \log_a n_2^2 \\ N_1 - N_2 + N_3 + 1 &= \log_a n_2 \end{aligned}$$

The way we defined the transfer matrix in equation 4.23, the number of periods for mirror 1, 2 and 3 are $(N_1+0.5)$, N_2 and (N_3+1) respectively. For the condition of $R_1 = R_3$, $N_3+1 = N_1$.

$$\boxed{N_2 = 2N_1 - \log_a n_2\,; \quad a = \frac{n_1}{n_2}} \quad \text{(condition for unity transmission)} \tag{4.26}$$

For the mirror design, different material combinations can be chosen. Some commonly used material combinations are given in Table 4.1. Any material can be paired with air, or other combinations are also fine. We have to take the nearest integer value for N_2 calculation.

TABLE 4.1: Values of $\log_a n_2$ for common materials @ 1550 nm.

	Si	TiO_2	SiN	SiO_2	Air
Si (3.48)	-	-3.77	-2.25	-1.41	-1
TiO_2 (2.5)	-	-	-4.11	-1.66	-1
SiN (2)	-	-	-	-2.11	-1
SiO_2 (1.44)	-	-	-	-	-1

Reflectivity of a Bragg mirror depends on the number of periods in alternating layers. The formula for reflectivity is:

$$R = \left[\frac{1 - \left(\frac{n_2}{n_1}\right)^{2N}}{1 + \left(\frac{n_2}{n_1}\right)^{2N}} \right]^2 \tag{4.27}$$

For the combination of Si/Air and SiN/SiO_2, reflectivity vs. number of periodics is depicted in Figure 4.6. For $R > (95\%, 99\%, 99.9\%)$, (2, 3, 4) periods are needed for Si/Air and (7, 10, 13) periods are needed for SiN/SiO_2. The effect of different number of periods for these two combinations are depicted in Figure 4.7 using equation 4.23. For this work, the goal is to have a narrow linewidth device so that it can work as a power limiter and filter simultaneously. Therefore the layers will be chosen such that $R > 0.999$, or in another word, $N \geq 4$ for Si/Air and $N \geq 13$ for SiN/SiO_2 combination. To investigate the effect of deviation from the unity transmission condition (from equation 4.26), transmission profile for different N_1 and N_2 are depicted in Figure 4.8. As we can see from the figure, change in only 1 period results in a significant effect on the transmission profile due to the high quality factor cavity. Amount of change can be controlled by changing the number of periodic layers.

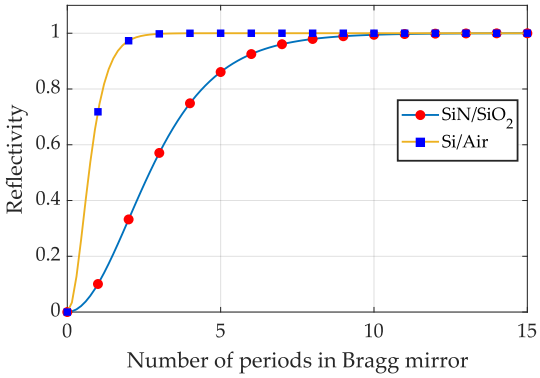

FIGURE 4.6: Effect of number of periods on Reflectivity of a Bragg mirror for SiN/SiO_2 and Si/Air.

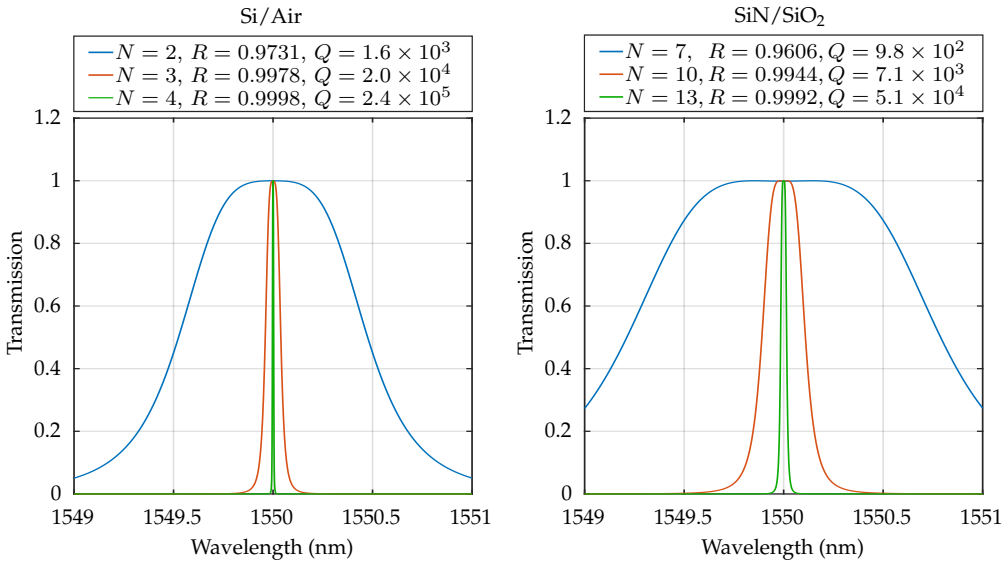

FIGURE 4.7: Three mirror cavities: overall transmission profile for different N. Corresponding reflectivities (for outside mirrors) and Quality factors are also given. (left) Si/Air, here $N_1 = N,\ N_3 = N - 1, N_2 = 2N + 1$. (right) SiN/$SiO_2$, here $N_1 = N,\ N_3 = N - 1, N_2 = 2N + 2$. Difference in N_2 value is from Table 4.1.

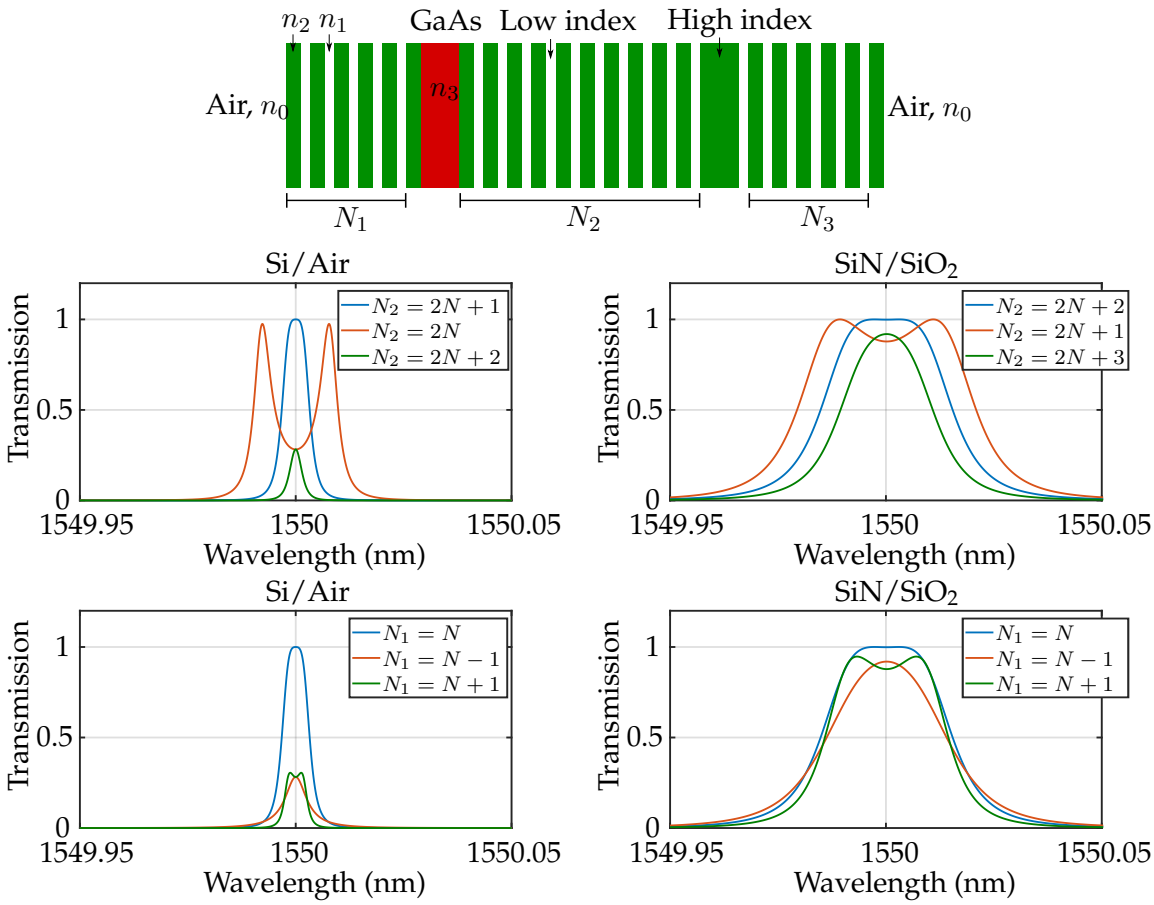

FIGURE 4.8: (top) Effect of changing the value of N_2 (while N_1 and N_3 unchanged) from unity transmission condition. (bottom) Effect of changing the value of N_1 (while N_2 and N_3 unchanged) from unity transmission condition. As Si/Air has higher-Q cavity compared to SiN/SiO$_2$, so the change is also more prominent.

Now, as we have the design parameters and justification for them, we need to analyze the performance of the device as a power limiter and as a filter. First we consider the SiN/SiO$_2$ combination: Bragg mirror periods for unity transmission are $N_1 = (N+0.5)$, $N_2 = (2N+2)$ and $N_3 = (N-1)$. As depicted in Figure 4.9 (a), with the increase of intensity the peak shifts, splits into two peaks and maximum transmission decreases. In Figure 4.9 (b), the maximum transmission at design wavelength (1550 nm) is plotted against input intensity. The cutoff intensity is assumed to be 2×10^8 W/m^2 (for a $500\,nm\times500\,nm$ waveguide with 1mW power, the intensity is 4×10^9 W/m^2, and for this case, 2×10^8 corresponds to 50µW). As we can see from the figure, higher value of N results in earlier cutoff intensity. Output intensity is plotted against input intensity in Figure 4.9 (c). Until the threshold intensity, output power is same as the input power, however, after the threshold intensity the output starts to drop. Similar analysis is also done for Si/air combination as depicted in Figure 4.10. The figure is qualitatively same as Figure 4.9 except some quantitative changes due to the different reflectivity.

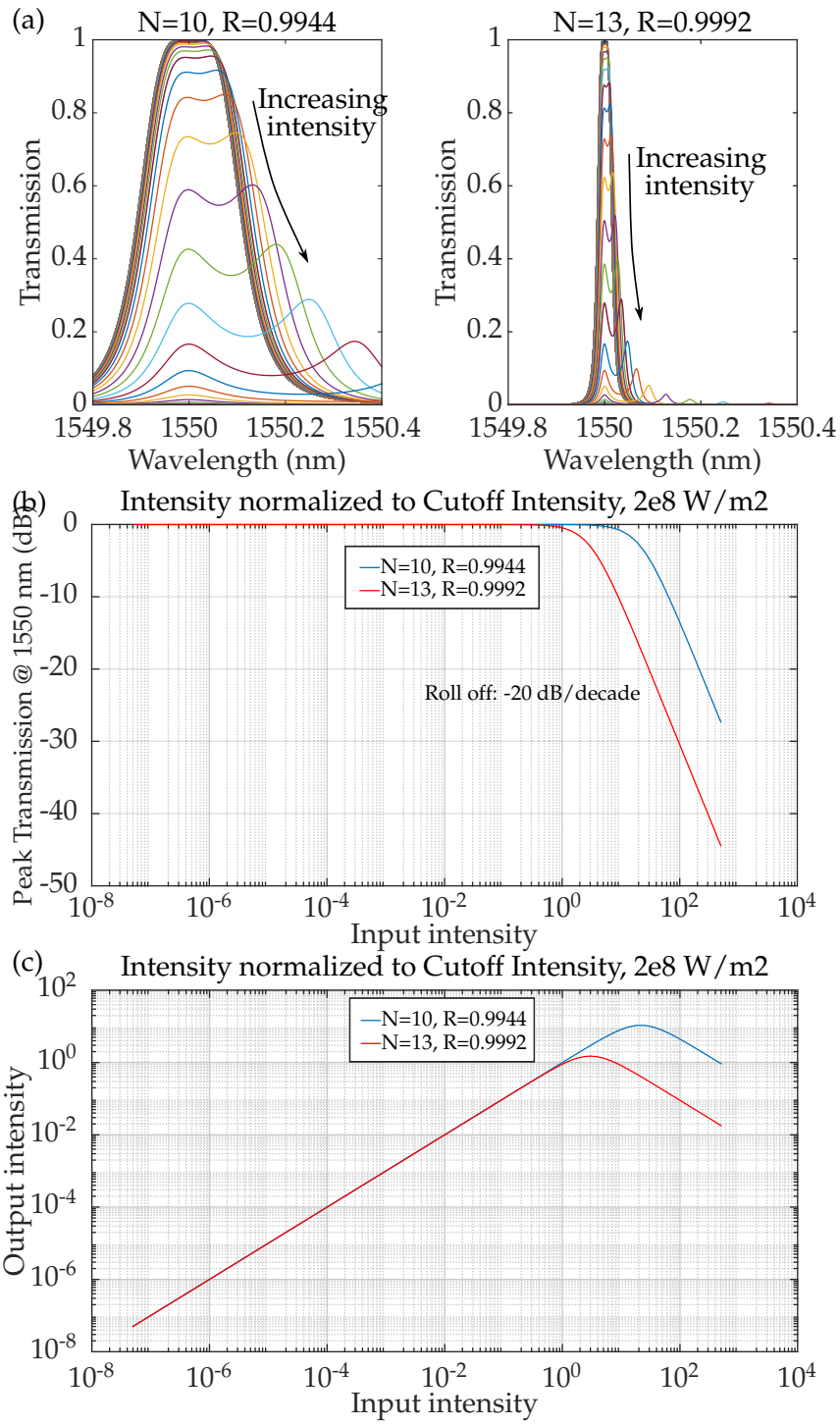

FIGURE 4.9: Expected performance of the device made of SiN/SiO_2. (a) with the increase of input intensity, the peak shifts, splits into two peaks and maximum transmission decreases. With the increase of layer numbers (as well as reflectivity), the FWHM of the transmission decreases. (b) Peak transmission as a function of input intensity. The peak drops sharply after the cut-off intensity. (c) Output intensity vs. input intensity. The output increases linearly with the increase of input until the cut-off and then drops sharply.

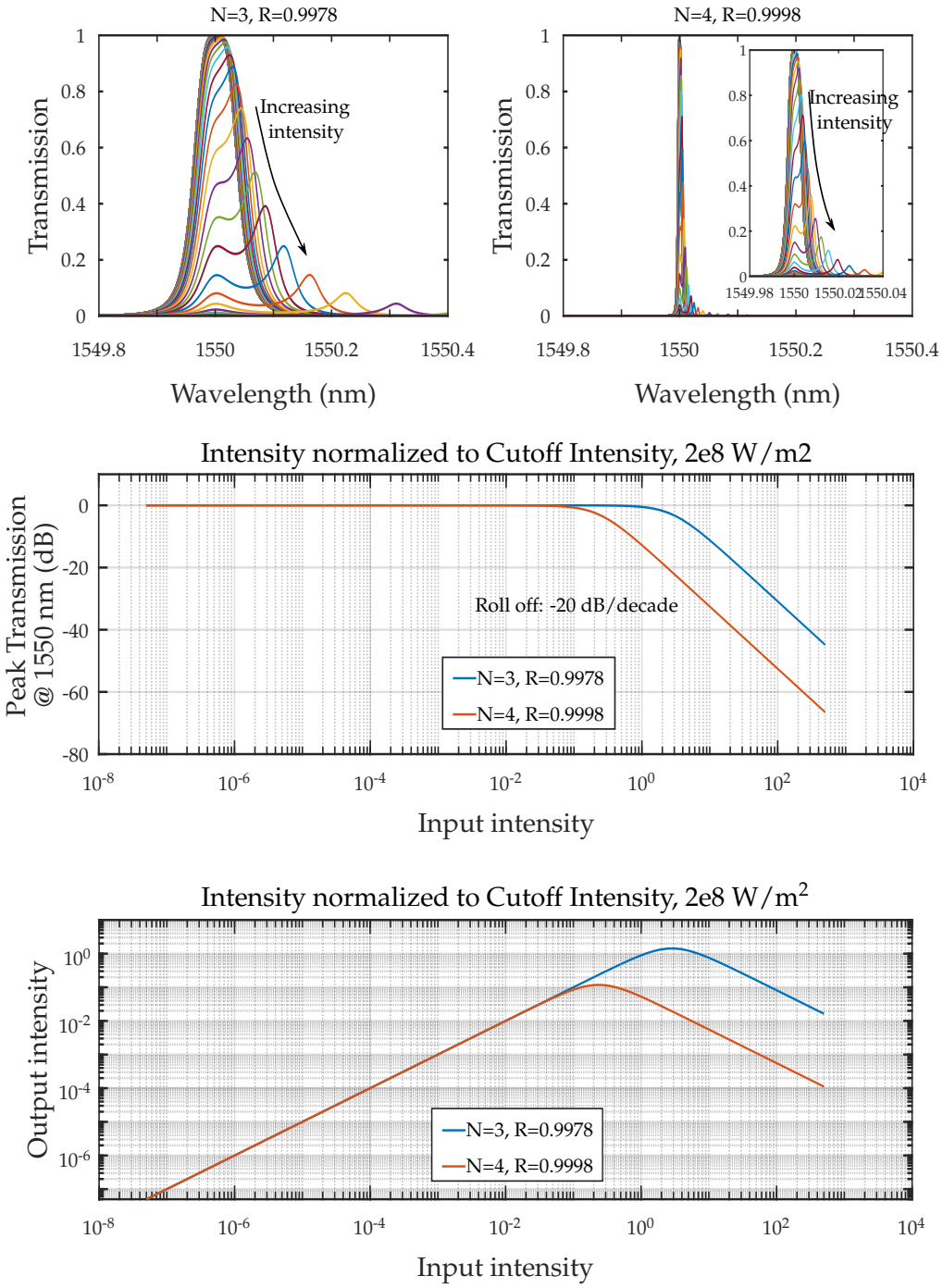

FIGURE 4.10: Expected performance of the device made of Si/air. (a) with the increase of input intensity, the peak shifts, splits into two peaks and maximum transmission decreases. With the increase of layer numbers (as well as reflectivity), the FWHM of the transmission decreases. (b) Peak transmission as a function of input intensity. The peak drops sharply after the cut-off intensity. (c) Output intensity vs. input intensity. The output increases linearly with the increase of input until the cut-off and then drops sharply.

4.5 Fabrication outlook

Combining III-V materials with Si based materials during nanofabrication is often difficult due to several challenges including lattice mismatch (for GaAs/Si this difference amounts to $\approx 4.2\%$) and different thermal expansion coefficient (for GaAs/Si it is $\approx 123\%$) [85]. However, two possible fabrication strategies are proposed for SiN/SiO_2/GaAs and Si/Air/GaAs devices.

4.5.1 SiN/SiO_2/GaAs device

For the device consisting of SiN/SiO_2/GaAs, a vertical stacking approach is proposed [27]. The fabrication starts on a glass wafer, and then Plasma-enhanced chemical vapor deposition (PECVD) can be used to deposit the first Bragg reflector onto the substrate. The exact thickness of the layers would depend on the target wavelength and material refractive index by the Bragg condition, $\lambda/4n$. Then the GaAs cavity layer can be deposited either by RF sputtering or molecular-beam epitaxy (MBE). Though there would be lattice mismatch at the interface, non-linear optical properties and refractive index would not change much as evident from [27]. After depositing the GaAs, the second and third Bragg mirror layers and the in between SiN cavity layer can be deposited using PECVD again. The process flow is depicted in Figure 4.11. This device can be placed perpendicular to the optical axis of propagation and act as a filter integrated with power limiter for the designed wavelength.

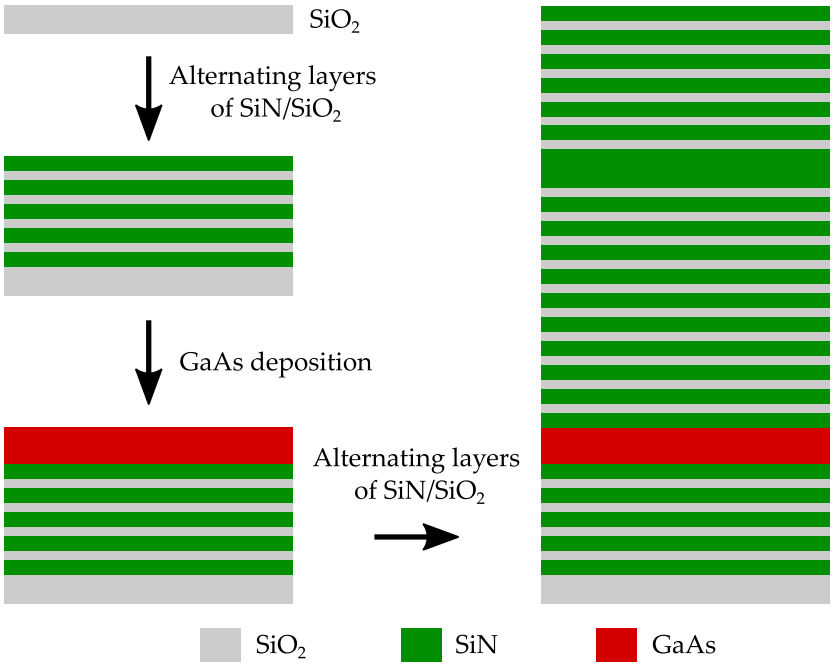

FIGURE 4.11: Proposed fabrication process for SiN/SiO_2/GaAs optical power limiter integrated with filter.

4.5.2 Si/Air/GaAs device

A planar structure is proposed for the device made of Si/Air/GaAs due to material combination. For this device, the fabrication starts with a GaAs film on a Si substrate having SiO_2 as an interface layer. Depositing GaAs films on SiO_2 surface is challenging due to lattice mismatch, however, not impossible and is demonstrated in [27] for GaAs on SiN surface. An interface layer is necessary which has lower refractive index than Si ($n_{Si} \approx 3.48$ at 1550 nm) and GaAs ($n_{GaAs} \approx 3.57$ at 1550 nm) for proper wave guiding through the silicon grating waveguide. Therefore, SiO_2 ($n_{SiO_2} \approx 1.44$ at 1550 nm) can be used as the separation layer and ~micron thick SiO_2 would suffice. An ebeam lithography step followed by a GaAs etch can be used to make strip line for the non-linear cavity layer. After that, Si can be deposited using PECVD, which would be amorphous silicon. Ebeam exposure can be used again for pattering the Si/air Bragg layers. Lastly, Si etch and removal of resist would provide the final device. In/out coupling of this planar device with external optics can be done with grating couplers. The proposed process flow is illustrated in Figure 4.12.

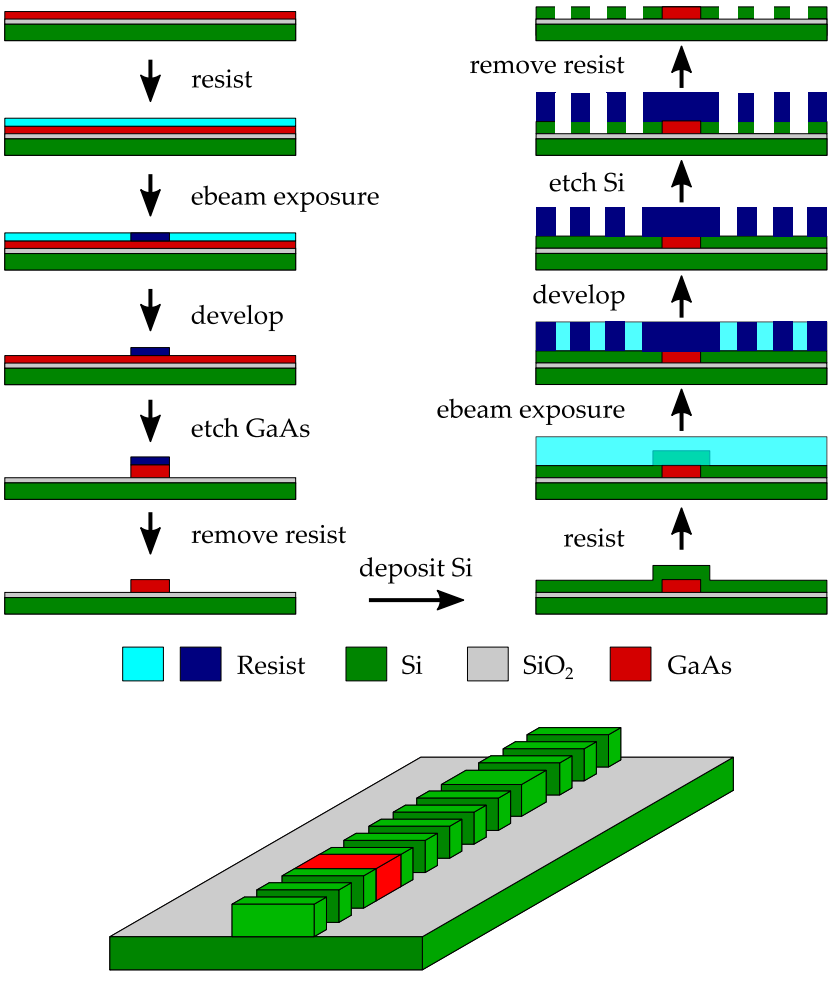

FIGURE 4.12: Proposed fabrication process for Si/Air/GaAs optical power limiter integrated with filter.

4.6 Conclusion

We propose a solid state optical power limiter integrated with optical filter that can be used in specialized applications including quantum cryptography, as well as other areas of photonics which require such functionality. The proposed device's cut-off intensity and bandwidth can be varied by changing the mirror reflectivity, and very narrow bandwidth (sub-nm) can be achieved with highly reflective mirrors. The peak transmission roll off after the cut-off is -20 dB/decade which is independent of the mirror reflectivity. Two possible fabrication plans are proposed, one is with vertical stacking where the optical axis is perpendicular to the device plane and the other one is a planar structure where the optical axis is in plane of the device.

Chapter 5

High Efficiency SNSPDs Evanescently Coupled to DLW Waveguides

5.1 Introduction

When high energy femtosecond laser pulses are focused inside a glass substrate, the refractive index of the focal volume changes. By moving the beam focus, waveguides can be made inside the substrate [33]. These waveguides can have good mode matching with optical fibers, which can be used to increase the efficiency of light coupling from the external source to the chip. Different kinds of passive devices, such as power splitters, directional couplers, interferometers, Bragg gratings, waveguides and waveguide lattices, as well as active devices, such as waveguide amplifiers or lasers, can be made using direct laser writing (DLW) [34]. Additionally, the capability to write 2D and 3D photonic lattices inside glass substrate make it more robust for fabricating on-chip integrated photonic devices and offers a promising platform for on-chip analogue quantum simulator.

Superconducting nanowire single photon detector (SNSPD) or superconducting single photon detector (SSPD), are a highly-promising technology for detecting photons from visible to telecom wavelengths, particularly at wavelengths for which Si absorption starts to drop (>900 nm). SNSPDs offer excellent potential for time correlated single photon counting (TCSPC) at the boiling point of He (4.2 K), a temperature which is easily attainable due to the advancement of the cooling techniques such as closed cycle cooling. In contrast to its competitors, such as Si SPAD for <900 nm and InGaAs SPAD for 900 nm - 1550 nm, SNSPD offers high detection efficiency, wider spectral range from ultraviolet to near-infrared wavelengths and lower dead time (the time after a detection event during which the device is not able to record another event), dark count rate and timing jitter which make it a suitable candidate for single photon detection in a wide range of applications.

Conventional SNSPDs are based on a meandering wire structure (Figure 5.1 (a)) that can also be integrated into a cavity to increase the probability of the photon being absorbed by the superconducting nanowire (Figure 5.1 (b)). The drawbacks of the meandering structures include limits on detection efficiency (from the low thickness of the metal and gaps between the nanowires) and inherently large kinetic inductance (arises from the inertia of electrons, and is proportional to the length and inversely proportional to the cross section of the nanowire. Dead time of the SNSPD increases with kinetic inductance, which in turn decreases the maximum count rate.) of the long wire forming the meander. Recently, SNSPDs have been implemented with superconducting nanowires deposited along on-chip silicon waveguides (Figure 5.1 (c)). This evanescently coupled geometry has a very high coupling

efficiency of photons from the waveguide to the nanowire. In this work, we explore the integration of SNSPDs with DLW waveguides, which could potentially lead to a fully on-chip photonic lattice platform.

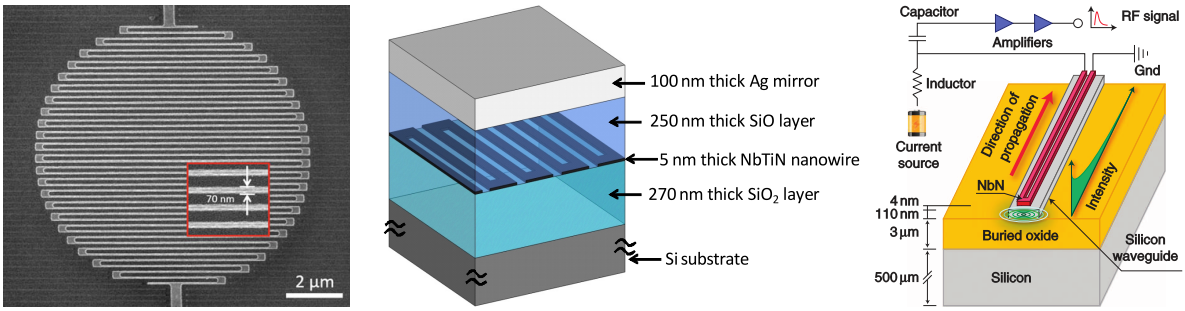

(a) (b) (c)

FIGURE 5.1: (a) Scanning-electron micrograph (SEM) of an SNSPD based on 70-nm wide nanowires. The inset shows a magnified SEM of the nanowires [86]. (b) Schematic configuration of a NbTiN SNSPD integrated into a cavity [87]. (c) Schematic of a NbN SNSPD evanescently coupled to a Si waveguide [88].

5.2 Single-Photon Detectors

The major application areas related to single-photon detection and generation include biotechnology, photonics, physical science, metrology, sensing, medical physics, and quantum information processing (Figure 5.2). Single photon detectors (SPD) are highly sensitive devices which can trigger an output pulse even by the excitation of a single light quanta. The performance of a SPD can be characterized by the following properties:

- **Detection efficiency:** The probability that an output signal is registered when a photon is incident on the detector. The overall system detection efficiency (η_{sde}) can degrade due to various factors, mainly because of inefficient coupling, reflection or transmission in the detector region and failure to record an event after absorption. Light being coupled from single-photon source to the active region of the detector can be lost due to absorption, scattering or reflection in the surrounding environment, which is called the coupling loss (η_{coup}) . However, not all photons hitting the detector are being absorbed, and not all absorbed photons give rise to output signal. These loss mechanisms are called absorption (η_{abs}) loss and registration loss (η_{reg}), respectively. Thus, the system detection efficiency can be defined as:

  $$\eta_{sde} = \eta_{coup} \times \eta_{abs} \times \eta_{reg}$$

  The intrinsic device detection efficiency (η_{dde}), also known as quantum efficiency, depends on absorption and registration efficiency.

  $$\eta_{dde} = \eta_{abs} \times \eta_{reg}$$

- **Dark Count Rate (DCR):** The average number of counts without any incident light, mainly because of stray light and electrical noise.

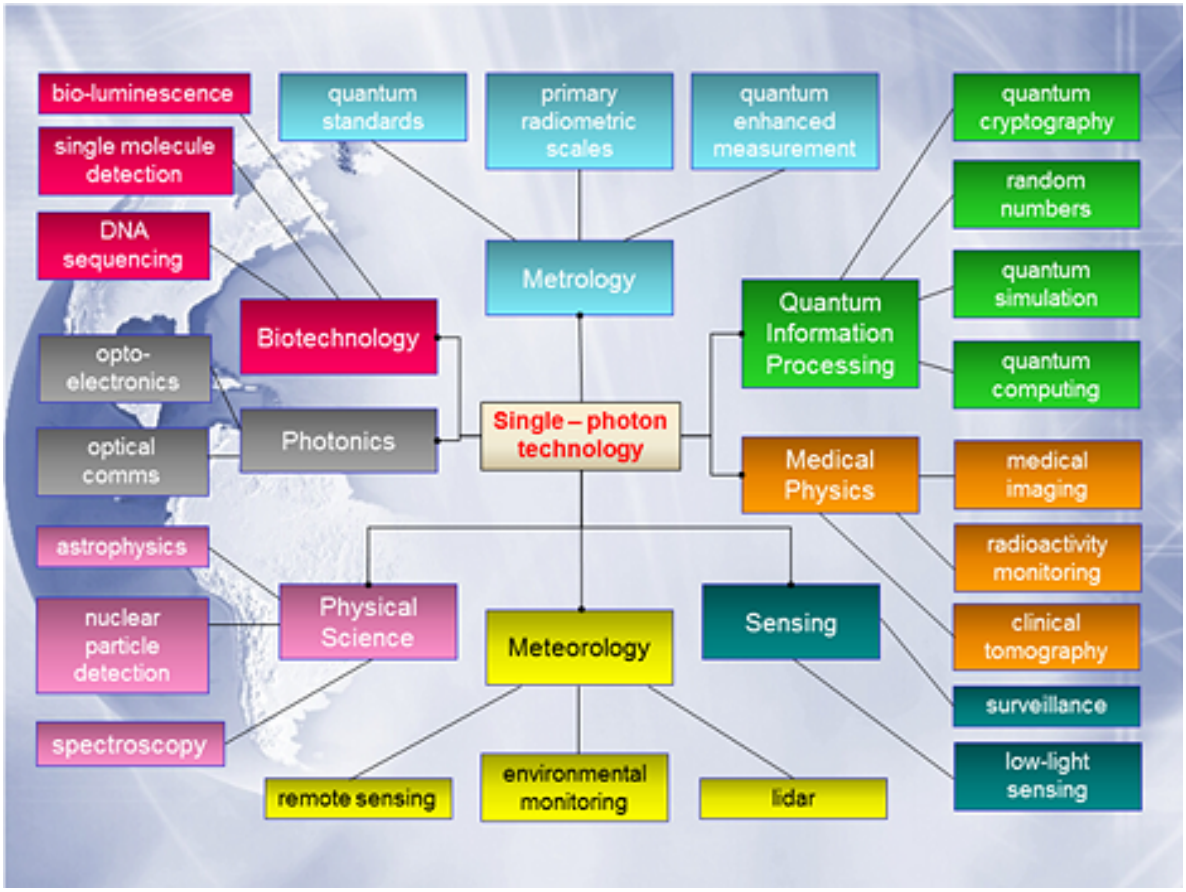

FIGURE 5.2: Applications pertaining to single-photon detection and generation [89].

- **Dead time and Maximum Count Rate (MCR):** After detecting a photon, the detector needs some time to reset to its initial state to prepare itself for the next incident, which is called the dead time. In some SPDs, such as semiconductor SPDs, the dead time is lengthened deliberately to reduce the afterpulsing probability. The maximum count rate is determined by the speed of the detector, mainly limited by the dead time, and/or the corresponding electronics.

- **Timing jitter:** The variation in the time interval between the absorption of a photon and the generation of an output electrical pulse from the detector is referred to as timing jitter. Though the timing uncertainty can be caused by the detector and/or the measuring apparatus, typically the dominant source is the detector. To quantify the timing jitter, a large number of samples is acquired and the full-width-at-half-maximum (FWHM) of the sample histogram is measured.

- **Figure of Merit (FOM):** Comparison of different single-photon detectors can be done in various ways depending on the area of application, taking one or more performance parameters into account. A widely used figure of merit for comparing single-photon

detectors is the following dimensionless quantity:

$$FOM = \frac{\eta}{DCR \times \Delta t}$$

Where, Δt = timing jitter.

5.2.1 Single-photon detector technologies

Photomultiplier Tube (PMT): The photomultiplier tube is the oldest of all photon counting technologies and was first demonstrated in 1949 [90]. A PMT is a sealed evacuated glass tube containing a photocathode, focusing electrodes, an electron multiplier and an anode; often coupled to a scintillator (Figure 5.3). Incident radiation on the scintillator emits comparatively low energy photons and those having more energy than the work function of the photocathode material liberate photoelectrons from the photocathode. Photoelectrons are accelerated and focused by the focusing electrode onto the electron multiplier, consisting of a number of electrodes called dynodes, where they are multiplied by means of secondary emission. Each dynode is held at a more positive potential than the previous one by ≈100 V and emission from the last dynode is collected by the anode.

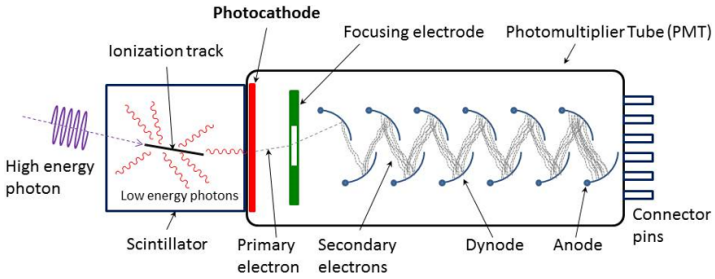

FIGURE 5.3: Schematic of a PMT coupled to a scintillator [91].

A photomultiplier tube offers large active area (≈1 cm diameter) with a wide spectral range from 115 nm to 1700 nm [92], while providing a large variation in the efficiency. It has a maximum efficiency of 40% at a wavelength of 540 nm in GaAsP PMT [93], dark count rate as low as 100 Hz with a typical jitter of 300 ps in the micro-channel plate PMT [92]. The performance at the telecom wavelength of 1550 nm is poor compared to the visible range, having an efficiency of 2% and dark count rate ≈200 kHz [92].

Single-Photon Avalanche Diode (SPAD): SPADs are the most widely used single-photon counter available for visible to near-infrared wavelengths. These solid state devices are based on reversed biased p-n or p-i-n junction operated above the breakdown voltage, known as Geiger mode operation (Figure 5.4 (a)). At this very high electric field in the p-n junction, a generated electron-hole pair by a single-photon absorption can trigger a self-sustaining avalanche which gives rise to a macroscopic steady current in the mA range. The avalanche can be stopped by a simple passive quenching circuit (with a high value load resistor, $\geq$ 100 kΩ) or using a more advanced active quenching circuit where pulling the bias voltage below the breakdown voltage and then pushing it again to the initial biasing state is done by external electronics.

The Silicon SPADs offer high detection efficiency, low dark count rate and high maximum count rate in the visible to near-infrared region (<1000 nm). The geometry of Si-SPADs can

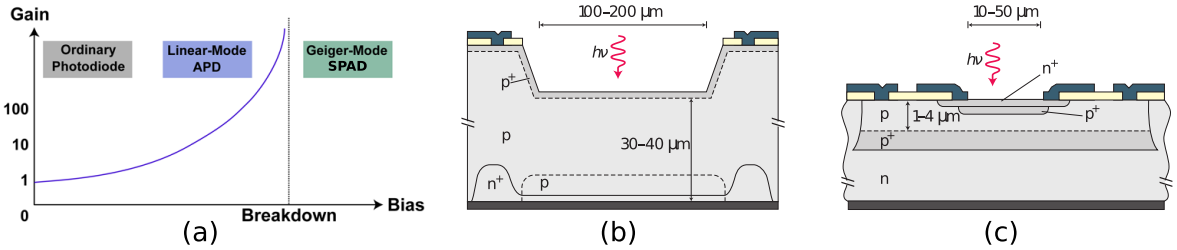

FIGURE 5.4: (a) Operating regions for ordinary, linear-mode and Geiger-mode photodiodes (b) Thick-junction Si-SPAD. (c) Shallow-junction planar Si-SPAD [94, 95].

be broadly categorized into thick-junction and shallow-junction planar devices (Figure 5.4 (b, c)). The thick-junction devices have larger active area (100 µm - 500 µm) compared to the shallow-junction devices (<100 µm), higher detection efficiency and low dark count rate at the expense of higher timing jitter (≈400 ps) and high operating voltage (≈400 V). The shallow-junction planar devices offer very low timing jitter (≈40 ps) operated at low voltage at the expense of reduced detection efficiency. The best commercially available Si-SPAD has a photon detection efficiency of 75% at 670 nm, dark count rate as low as 100 Hz, timing jitter of 350 ps and dead time of 45 ns [96].

As Si absorption drops significantly beyond 1000 nm, to extend the detection of SPAD in the telecom wavelengths (1310 nm and 1550 nm), group III-V heterostructure devices having lower bandgap materials such as InGaAs/InP are used. Owing to material defects and lower bandgap, these devices have higher dark count rate, lower detection efficiency and higher timing jitter compared to Si-SPADs. The best commercially available InGaAs/InP SPAD at 1310 nm has the detection efficiency up to 40%, dark count rate <10 kHz, timing jitter <100 ps (optimized performance for individual parameters) [98] and at 1550 nm, detection efficiency up to 25%, dark count rate <100 Hz and timing jitter of 200 ps [99].

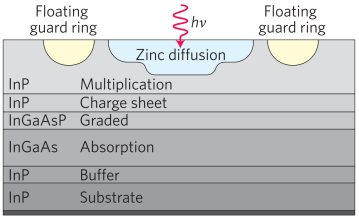

FIGURE 5.5: Schematic of a InGaAs/InP SPAD [95, 97].

Frequency up-conversion: In this technique, photons in the telecommunication wavelengths (1310 nm and 1550 nm) are converted to shorter wavelengths using sum-frequency generation (SFG) so that the high performance Si-SPADs can be used for the detection (Figure 5.6a). In SFG, a weak signal at λ_{in} and a strong pump signal at λ_{pump} are combined using a non-linear optical crystal, such as periodically poled lithium niobate (PPLN), to generate an output signal at λ_{out} with $1/\lambda_{out} = 1/\lambda_{in} + 1/\lambda_{pump}$. Though it seems a nice solution for detecting photons beyond Si absorption, there are several technical difficulties to achieve this. The first one is to achieve the desired field strength at the pump, either through a continuous-wave pump pulse and a build up cavity [100], a coincident pump and signal pulse [101], or by using a waveguide to concentrate the pump power into a small interaction region [102]. Other difficulties include stability of the nonlinear crystal, presence of the fluorescence at the upconversion frequency results in high dark count rate, high input and output coupling loss at the waveguides. The best reported result using this scheme has a detection efficiency of 46% at 1550 nm, timing jitter of 40 ps and dark count rate of 800 kHz [102].

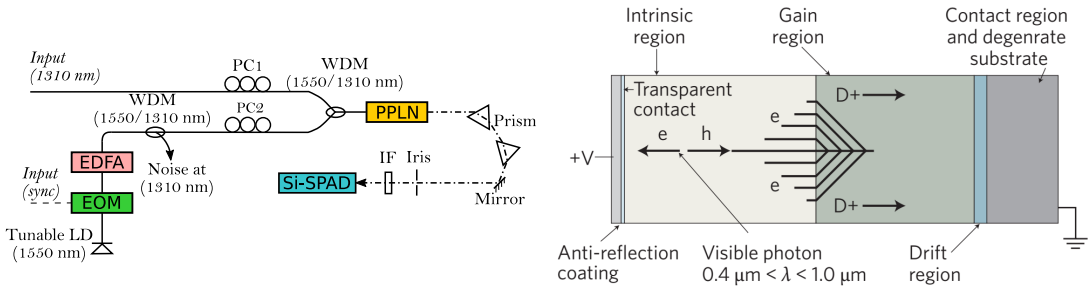

(a) (b)

FIGURE 5.6: (a) Schematic of a frequency up-conversion detector [103]. (b) Schematic of a VLPC detector [95]

Visible light photon counter (VLPC): VLPCs are low-temperature (∼6 K) Si-based SPDs with a separate absorption and gain layer which operates at ≈ 7 V (Figure 5.6b). It offers high-efficiency detection of single-photon up to wavelengths of 1 μm, photon number resolution (PNR), moderate dark count rate and timing jitter. In these devices, the absorption of a photon in the undoped Si produces an electron–hole pair, and the resulting hole triggers an avalanche in the gain region, thereby producing a multiplication process. This gives rise to a signal that is proportional to the photon number and has been proven successful for counting up to five photons. A quantum efficiency up to 88% at 694 nm with a dark count rate of 20 kHz and dead time of 100 ns has been reported [104].

Superconducting transition-edge sensor (TES): Superconducting TESs are highly sensitive microcalorimeters made from superconducting films operated by voltage bias near its transition temperature where a small change in temperature can cause an abrupt change in resistance (Figure 5.7). Absorption of a photon can heat up the superconducting material (in mk range) and cause a large change in resistance which can be detected by a SQUID amplifier. These detectors offer very high detection efficiency (98% at 850 nm [108]), photon number resolution capability (up to 8 photons resolution has been reported [109]) and negligible dark count rate (0.6 Hz [108]). Due to the PNR, inherently TES is resistant to false

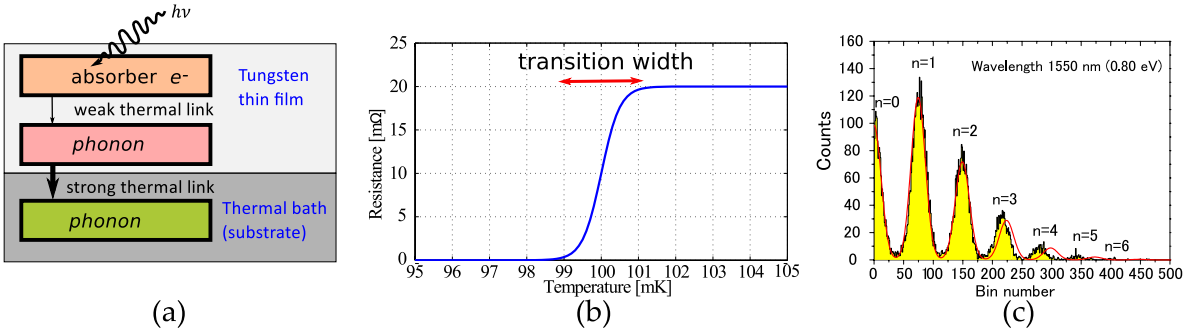

(a) (b) (c)

FIGURE 5.7: (a) Fundamentals of TES operation: optical photon absorbed by an electron in tungsten followed by energy distribution to phonon via thermal weak link and then to the phonon in the thermal bath via strong thermal link [105]. (b) Resistance vs. temperature in a typical TES. The transition width is couple of mK [106]. (c) Photon number histogram in a Ti-TES showing 6 photons resolution [107].

positive but there might be dark counts due to the background radiation. However, the timing properties of these detectors are relatively poor, timing jitter of 2.3 ns at 775 nm [110] and dead time of ≈ 0.5 µs [111] have been reported.

Superconducting nanowire single-photon detector (SNSPD): The superconducting nanowire single-photon detectors (SNSPDs) are a type of near-infrared and optical single photon detector based on a current-biased narrow (< 150 nm) and thin (< 10 nm) superconducting wire (Figure 5.8). The materials used for making the nanowires include niobium nitride (NbN), niobium titanium nitride (NbTiN), tantalum nitride (TaN), molybdenum silicide (MoSi), molybdenum germanium (MoGe), niobium silicide (NbSi), tungsten silicide (WSi) and magnesium diboride (MgB_2). They exhibit high detection efficiency (93% at 1550 nm [112]), low dark count rate (4 Hz at 70% SDE [113]), low timing jitter (18 ps [88]) and short recovery time from visible to mid-infrared wavelengths. The detector is current biased (a fixed current through the device) well below its critical temperature (T_c) but close to its critical current (I_c). Absorption of a photon locally destroys its superconductivity, leads to a nonzero resistance and thus triggers a voltage pulse that can be amplified and measured. The detection efficiency and dark count both are proportional to the bias current, but the latter rise more steeply close to the critical current.

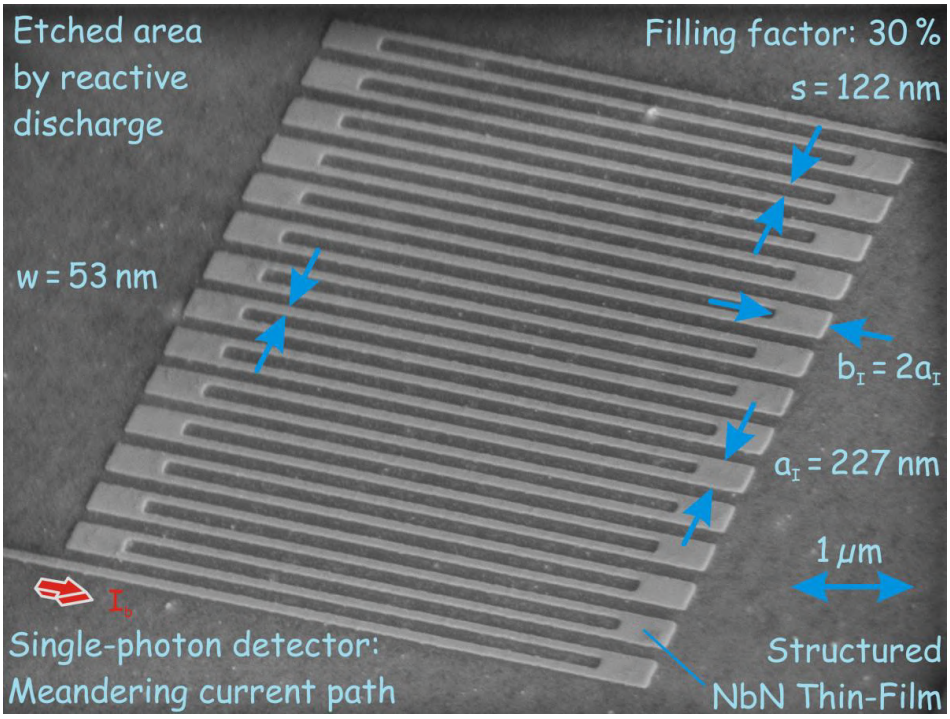

FIGURE 5.8: SEM image of a typical meander type SNSPD having an area of ~25 µm^2 [114].

5.3 SNSPD device physics

The nanowire in SNSPD is biased close to its superconducting critical current (current that destroys the superconductivity, above which the nanowire act as a normal conductor). When

a photon is incident and being absorbed by the detector, it generates an energetic quasiparticle which thermalizes a population of quasiparticles through electron-electron and electron-phonon scattering and creates a spatially localized region where the superconducting gap is suppressed (Figure 5.9 (a)). This non-superconducting area, referred to as hotspot, can be of ∼10 nm diameter which forces the supercurrent to go through the surrounding region, increases the current density of that region above critical current and the whole region becomes a normal conductor. In this process, the resistance of the wire grows from zero to several kΩ and causes a voltage drop that can be detected by the external electronics. A simplified circuit model is depicted in Figure 5.9 (b), where R_N is the normal state resistance of the nanowire (typically in few kΩ range), L_K is the kinetic inductance of the nanowire (typically a few µH), R_L is the impedance of the readout circuit (typically 50 Ω). The switch is closed in the steady state, causing the current to flow through it, and open in the case of absorption of a photon, forces the current to flow through the R_L ($R_L \ll R_N$).

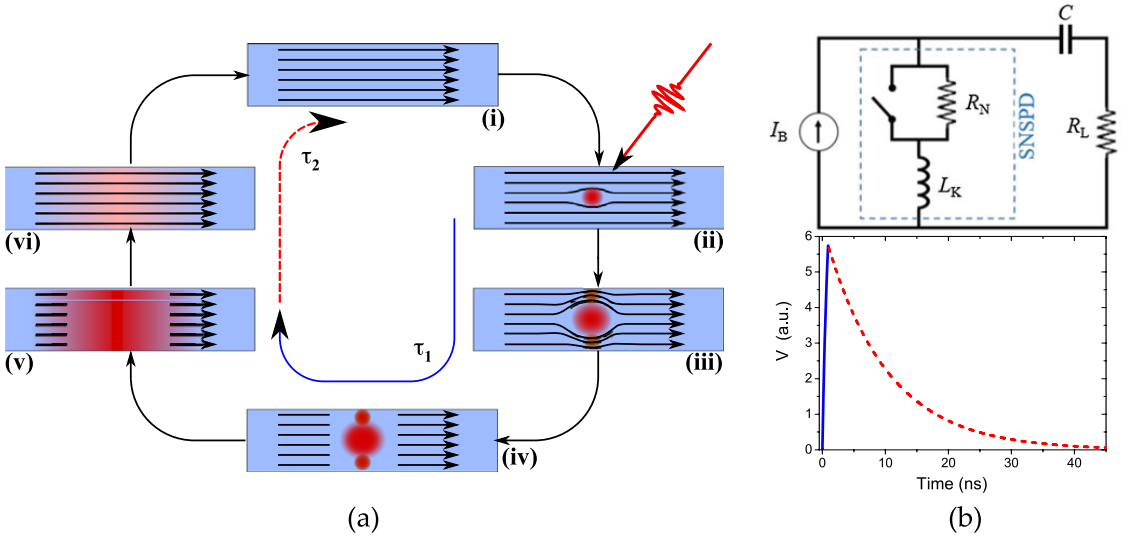

FIGURE 5.9: (a) Photodetection mechanism of SNSPD. Starting with the nanowire in superconducting steady state, upon absorption of a photon generates a hotspot that in turn creates a non-superconducting region. The voltage drop induced by this resistive region can be detected. (b-c) Simplified circuit model for SNSPD and typical voltage response in the readout circuit. (a) & (c) from [115] and (b) from [86].

5.4 Direct Laser Writing

When high energy fs-laser pulses are focused inside a glass substrate, the refractive index of the focal volume changes. By moving the beam focus, waveguides can be made inside the substrate [33]. These waveguides can have good mode matching with optical fibers, which can be used to increase the efficiency of light coupling from the external source to the chip. Different kinds of passive devices, such as power splitters, directional couplers, interferometers, Bragg gratings, waveguides and waveguide lattices, as well as active devices, such as waveguide amplifiers or lasers, can be made using DLW [34]. Additionally, the capability to write 3D photonic structures inside glass makes this technique more robust for fabricating on-chip integrated photonic devices.

5.4.1 Mechanisms for fs-laser induced structural changes

When tightly focused fs-laser pulses are incident inside a transparent material, the intensity can be high enough to initialize nonlinear field ionization and avalanche ionization in the focal volume in which one electron can gain sufficient energy from the laser to go to the conduction band and impact ionizes an additional electron. This nonlinear absorption can create electron-ion plasma in the focal volume (Figure 5.10 (a-d)). Three distinct regimes are normally associated with field-ionization process: the multiphoton ionization (MPI) regime, the tunneling ionization regime (TI) and the intermediate regime (Figure 5.10 (e)). Avalanche ionization is typically associated with material damage and it dominates when the laser pulse is in the order of 1 ps or more. Therefore, ultrafast lasers with pulse duration of 300 fs or less are employed to write photonic structures inside transparent materials. After the electron-ion plasma generation, the excess energy dissipates inside the material via plasma recombination. Depending on the laser energy and material parameters, three qualitatively different types of structural changes can occur: (i) isotropic refractive index change [116], (ii) birefringent refractive index change [117] and (iii) formation of void [118].

For low incident energy, the material in the focal volume melts and then quenches. Depending on the material, the density at the focal volume can increase, such as fused silica, or decrease, such as phosphate glass. Raman microspectroscopy indicates an increased number of 3- and 4- member ring structures in the silica after fs-laser irradiation [121, 122], while 5- and 6- member rings are predominate in untreated glass, and infrared spectroscopy indicates a decrease in the Si–O–Si bond angle [123]. Both of these indications point towards densification and increased refractive index in the irradiated zone. Apart from these, other processes, such as color center (positively charged oxygen vacancies) formation [124], can have small contribution to the refractive index change.

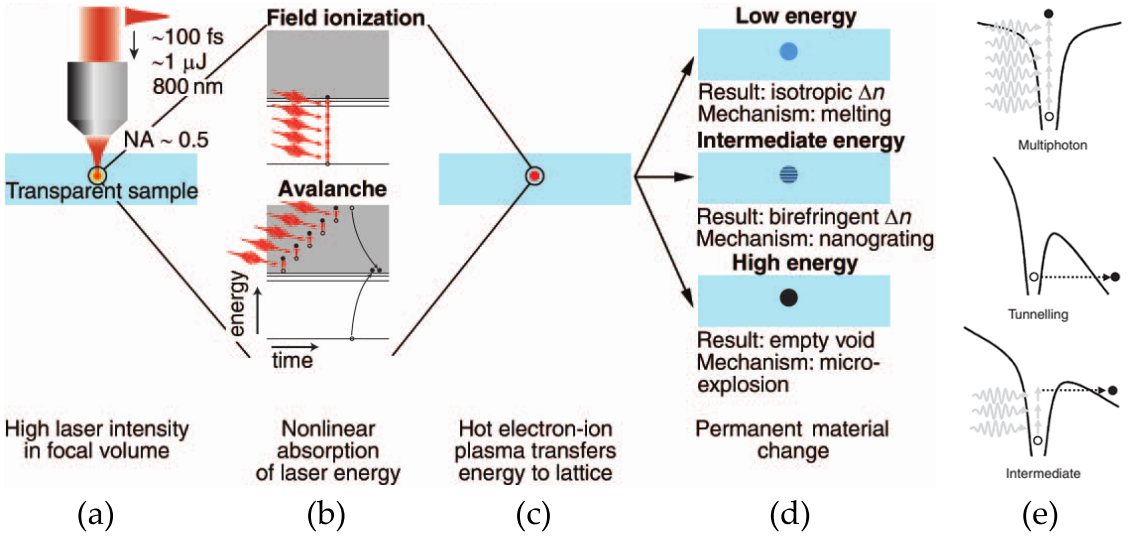

FIGURE 5.10: (a-c) Nonlinear absorption in the focal volume formed a hot electron-ion plasma [119]. (d) Depending on the energy, three different types of structural change can occur. (e) Three field ionization regimes. Multiphoton regime: a free carrier is predominantly generated through multiphoton absorption; Tunneling regime: a free carrier is predominantly generated through electron tunneling; Intermediate regime: combination of both [120].

5.4.2 Parameters of fabrication

The structural changes by ultrafast laser irradiation depends on laser parameters (such as pulse duration, wavelength, energy, repetition rate, writing speed, and number of passes), material parameters (such as band gap, thermal expansion coefficient) and numerical aperture of focusing. For a particular material and fixed numerical aperture, the laser parameters can be combined to a single equation, called Net Fluence, that can indicate the possible structural change.

$$NF = \frac{2w_0 RF_P}{v}$$

Here, w_0 = beam waist radius, R = repetition rate, F_P = per pulse energy, and v = writing velocity. For fused silica, the refractive index increases with the increase of net fluence. The effect of pulse energy, repetition rate and writing speed is depicted in Figure 5.11. For a fixed repetition rate, increase in energy has a moderate effect on the material while increasing repetition rate with constant energy shows more prominent effects due to cumulative heating. Typical parameters to write waveguides in fused silica are 100-300 fs-pulse, 1-1000 KHz repetition rate, 500-1000 nm wavelength, up to 100 mm/s writing velocity.

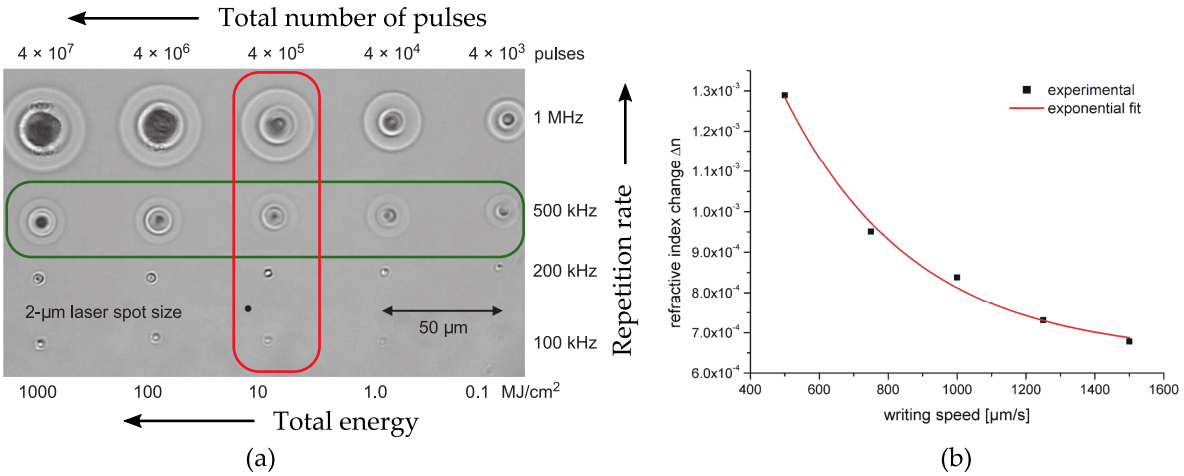

FIGURE 5.11: (a) Optical microscope images showing heat-affected zones created in borosilicate glass with 450 nJ pulse energy from a 1045 nm fs-laser [125]. (b) Refractive index change vs. writing speed in fused silica glass [126].

Femtosecond laser writing technique is capable of making a wide variety of active and passive, 2D and 3D integrated photonic structures in a wide variety of transparent materials. However, the challenges of using this technique includes slower writing speed compared to photolithography, smaller refractive index contrast which limits the waveguide bending radius, and higher propagation loss (~0.2 dB/cm) compared to optical fiber (0.2 dB/km). Nevertheless, with the advancement of laser technology and better understanding of material physics and chemistry, more practical applications of fs-laser writing is expected in the near future.

5.5 Design & Simulation

The major challenge of integrating SNSPDs with DLW waveguides is the very large mode field area (∼100 µm^2) of the glass waveguide compared to the nanowire size, which results in poor evanescent coupling. Therefore, to achieve high detection efficiency (>90%), very long (∼cm) nanowire detector is required which is extremely challenging to fabricate given the width of the nanowire is very small (∼100 nm). In this segment, a gradual progression of the design steps is presented, starting from the scenario of directly depositing the nanowire on top of the glass waveguide to the final proposed device structure.

The SNSPD design consists of NbN nanowire deposited on top of partially removed (by polishing) DLW waveguide, where the polishing helps to improve the light coupling to the nanowire. We start with an approximate calculation by modeling the waveguide-nanowire pair using Lumerical software to estimate the length needed for >90% absorption of light propagating in a variety of cylindrical waveguides with a pair of nanowires deposited along the waveguide length (Figure 5.12). The equations used to calculate the mode field area, effective absorption in the nanowires and the length needed to absorb 90% of the propagating light are respectively:

$$A_{mode} \approx \frac{\int n(r)|E(r)|^2 dA}{max\{n(r)|E(r)|^2\}} \tag{5.1}$$

$$\alpha_{eff} = \frac{A_{wire}\,\alpha_{metal}}{A_{mode}} \frac{I(r_0)}{max\{I(r)\}} \left[dB/\mu m\right] \tag{5.2}$$

$$L_{90\%} = \frac{10}{\alpha_{eff}} \left[\mu m\right] \tag{5.3}$$

Here, $n(r)$ = refractive index profile, $E(r)$ = electric field distribution, A_{wire} = cross sectional area of the nanowire, α_{metal} = absorption coefficient of the metal (NbN), $I(r_0)$ = intensity at the nanowire, $I(r)$ = intensity distribution. The waveguide-nanowire pair structure was simulated in Lumerical, electric field distribution was obtained for various materials and size combination and the simulation result was used to calculate the mode field area, effective absorption of the NbN nanowire placed at the radius of the waveguide and the length needed to absorb 90% of the guiding light as shown in Figure 5.13 & 5.14. Absorption in 100 µm and 500 µm nanowire was also calculated for comparison. The material combinations used for the calculation were DLW waveguides in glass, single mode fiber, tapered single mode fiber, glass in air, Si_3N_4 in air, GaP in air and Si in air. All the calculations were repeated for wavelength of 900 nm and 1550 nm.

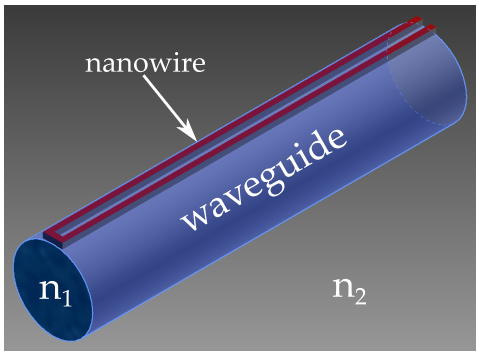

FIGURE 5.12: Schematic of the waveguide-nanowire pair

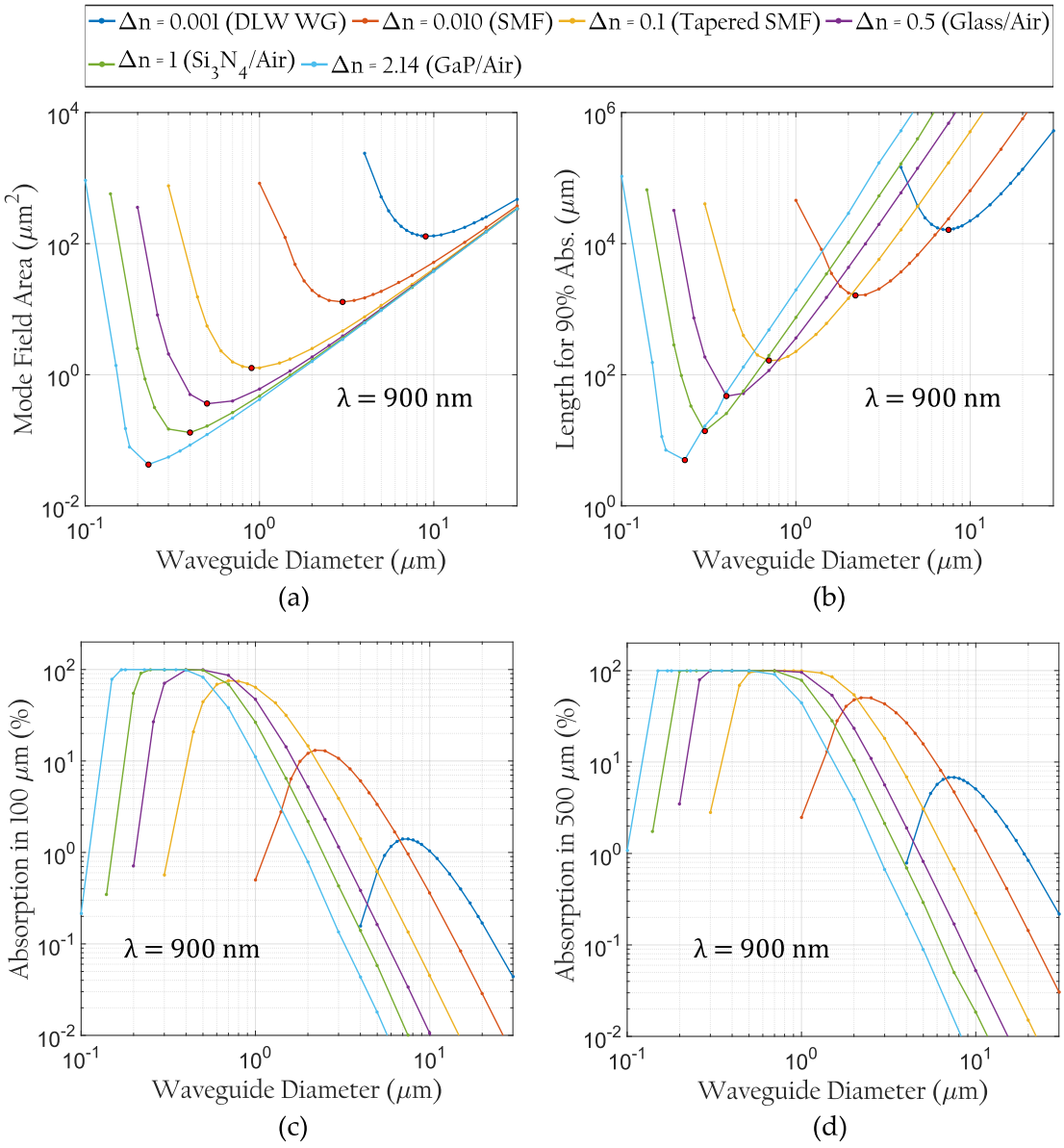

FIGURE 5.13: Mode field area, length needed to absorb 90% of the guided light, absorption in 100 µm and 500 µm NbN nanowire vs. waveguide core diameter for different material combinations at λ = 900 nm is plotted (extinction coefficient, $\kappa_{NbN} = 4.5$). The legends used for all the plots are shown on top.

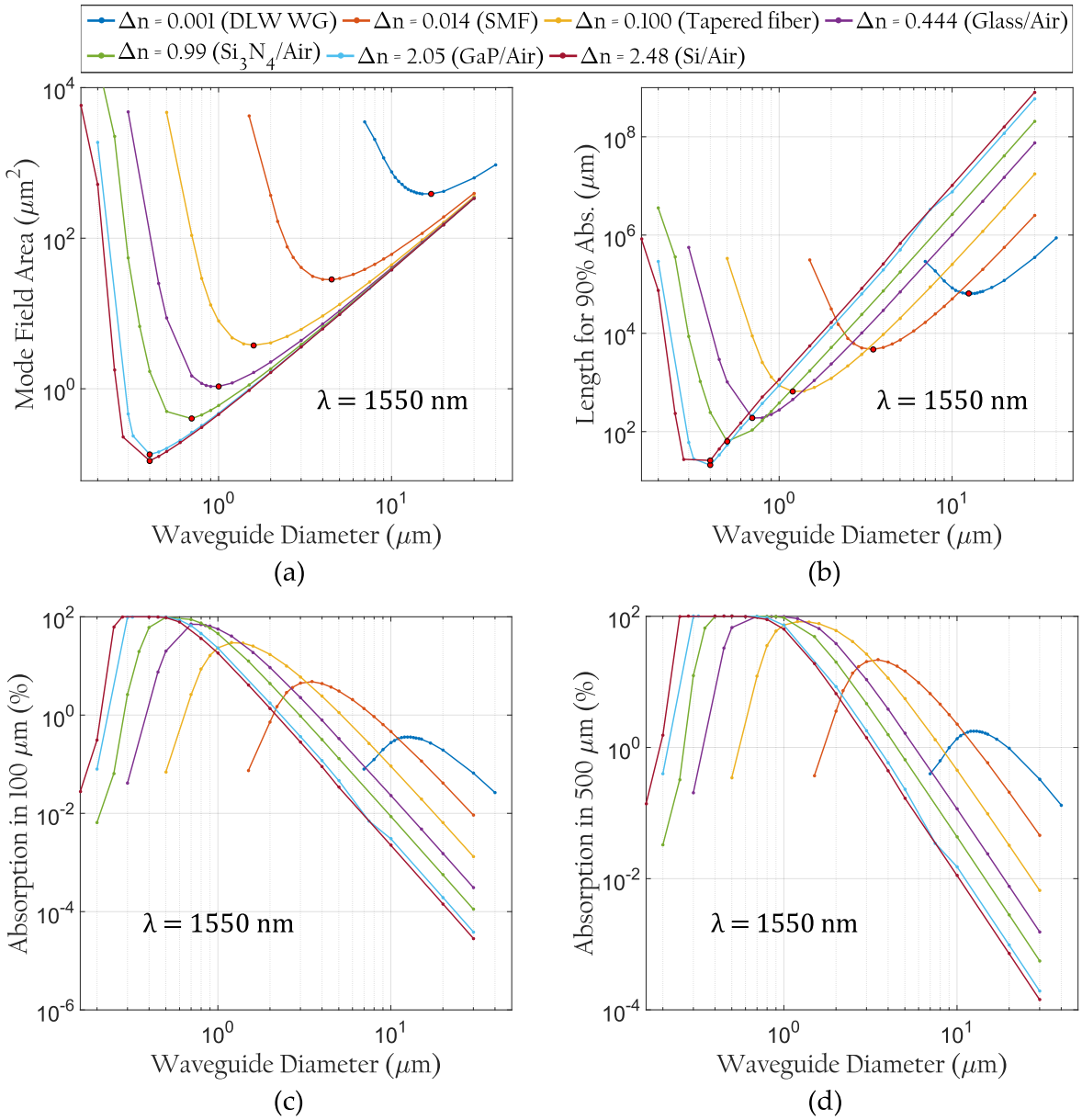

FIGURE 5.14: Mode field area, length needed to absorb 90% of the guided light, absorption in 100 µm and 500 µm NbN nanowire vs. waveguide core diameter for different material combinations at λ = 1550 nm is plotted (extinction coefficient, $\kappa_{NbN} = 5.82$). The legends used for all the plots are shown on top.

The calculated length needed for 90% absorption ($L_{90\%}$) at $\lambda = 900$ nm is ~16 mm, which is much larger than our target length of ~500 µm (single write field of e-beam lithography tool, to avoid stitching error). Therefore, to enhance the absorption further, a slab of SiO_2 with optimized dimension (from the Lumerical simulation) is used atop nanowires which pulls the light distribution towards the slab and results in increased absorption in the nanowire sandwiched between the slab and the waveguide. The optimization of the size of the slab depends on refractive index contrast, size, shape and amount of partial etching of the DLW waveguide. A schematic diagram of the simulated structure and result is shown in (Figure 5.15). Inclusion of the SiO_2 slab predicted a reduction in the $L_{90\%}$ by ~20%.

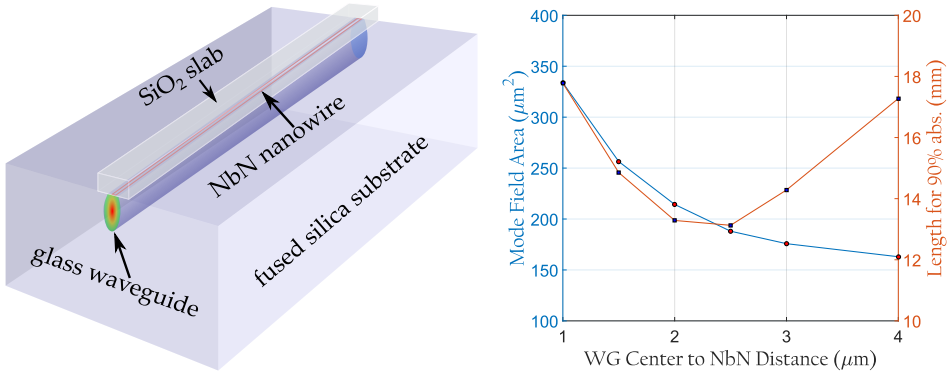

(a) (b)

FIGURE 5.15: (a) Schematic of SiO_2 slab atop nanowire and elliptical shaped waveguide (not to scale). (b) Mode field area and length needed for 90% light absorption vs. waveguide center to nanowire distance with partial removing of the waveguide (diameter = 8 µm) and with 20 µm × 6 µm SiO_2 slab.

Unfortunately, this would offer only an incremental improvement. We thus decided to approach the problem with a new design strategy, in which the light propagating in a DLW waveguide is first transferred via evanescent coupling to a high-index waveguide and then absorbed by the nanowires forming the detector. Addition of a higher refractive index material waveguide, such as Si_3N_4 waveguide, close to the glass waveguide instead of the SiO_2 slab will couple light to the Si_3N_4 waveguide due to mode overlap. The guided light will oscillate between the waveguides periodically, where the amount of maximum light transfer depends on the effective refractive index contrast and overlap of the modes. If the initial power is launched at waveguide 1 and being coupled to waveguide 2, from the coupled mode theory:

$$P_1 = 1 - F\sin^2(\psi z)$$

$$P_2 = F\sin^2(\psi z)$$

$$\text{where,} \quad F = \frac{\kappa_{12}\,\kappa_{21}}{\psi^2}, \quad \psi = \sqrt{\kappa_{12}\kappa_{21} + \delta^2}, \quad \delta = \frac{\beta_2 - \beta_1}{2},$$

$$\kappa_{pq} = \frac{\omega\varepsilon_0 \int_{-\infty}^{\infty}\int_{-\infty}^{\infty} (\varepsilon_r - \varepsilon_{r,q})\vec{E}_p^* \cdot \vec{E}_q \, dxdy}{\int_{-\infty}^{\infty}\int_{-\infty}^{\infty} \hat{z} \cdot (\vec{E}_p^* \times \vec{H}_p + \vec{E}_p \times \vec{H}_p^*)\, dxdy}$$

Here, κ_{pq} = mode coupling coefficient that quantifies how efficiently power leaks from waveguide p to waveguide q; ε_r = dielectric function containing both waveguides; $\varepsilon_{r,q}$ = dielectric function with only waveguide q; β = effective refractive index of the mode. Plots for P_1 and P_2 for different values of κ and β are shown in Figure 5.16. To maximize the power coupling from one waveguide to another, the β values should be as close as possible and κ values should be as large as possible. The mode coupling coefficients, κ, can be increased by reducing the distance between the waveguides and the difference in mode effective refractive indices, δ, can be reduced by choosing materials with close refractive indices. In the

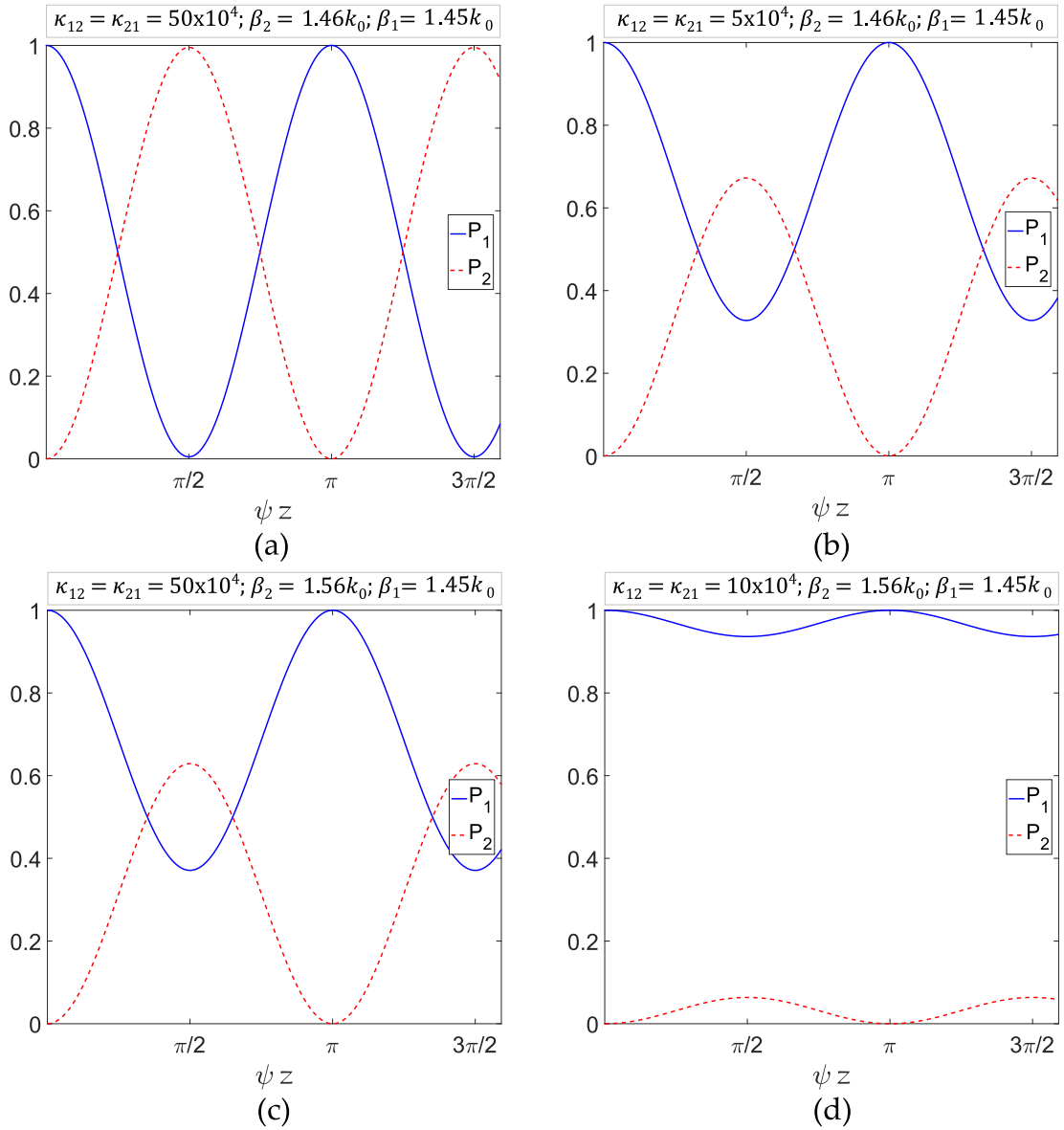

FIGURE 5.16: Coupling between two waveguides with different mode coupling constants and mode effective refractive indices are shown. (a) κ_{12} and κ_{21} are large and $\beta_1 \approx \beta_2$, so that all the power transfers to the second waveguide. (b) effect of reducing κ by tenfold. (c) effect of increasing $\Delta\beta$ by ~10 times. (d) effect of reducing κ and increasing $\Delta\beta$.

SNSPD design, focus is being given to increase the mode coupling coefficient by optimizing the size, shape and distance between the glass waveguide and the Si_3N_4 waveguide. In Figure 5.17, a simulation from Lumerical shows the power coupling between two waveguides at different distances. Initially power is launched at the glass waveguide, and then after a certain distance, the Si_3N_4 waveguide is introduced. Along the propagation direction, the power is being transferred to the second waveguide, and then again to the first waveguide.

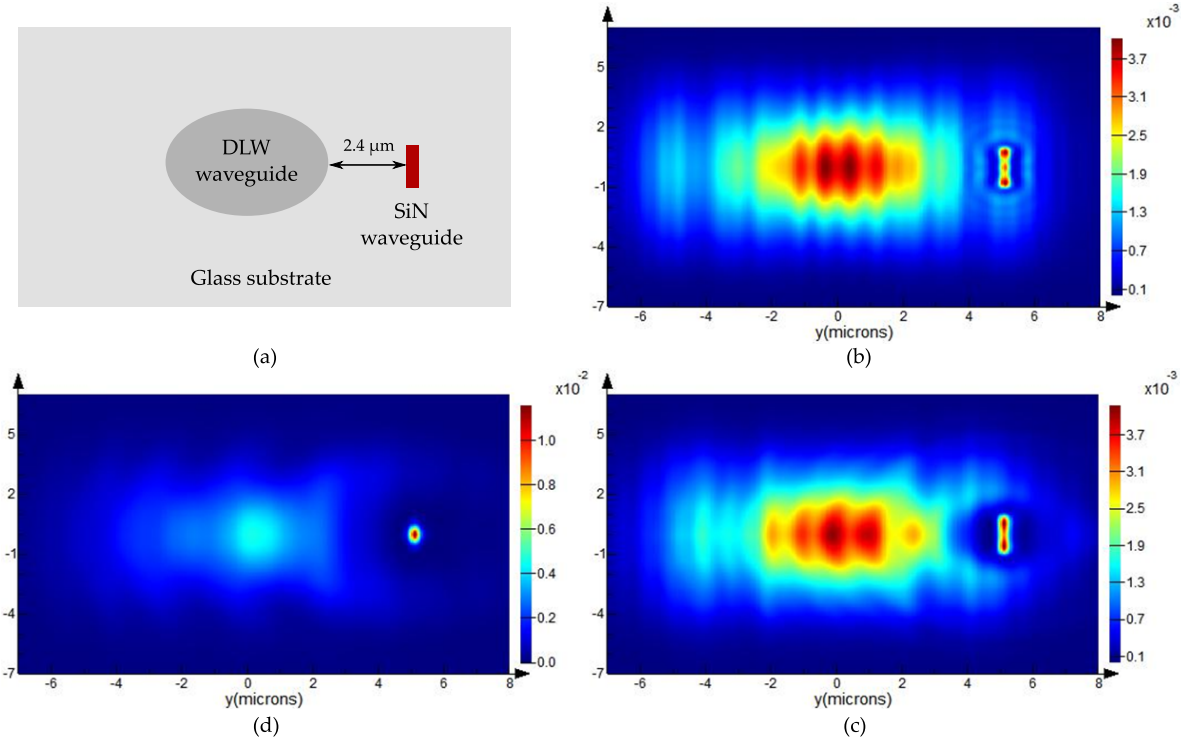

FIGURE 5.17: Coupling between two waveguides, a DLW glass waveguide and a Si_3N_4 waveguide at a distance of 2.4 μm, simulated in Lumerical. (a) Schematic of the simulated structure. (b-d) Measured power after 1 μm, 11 μm and 31 μm of introducing the Si_3N_4 waveguide.

5.5.1 NbN nanowire evanescently coupled to SiN waveguide evanescently coupled to Glass waveguide

When two waveguides are parallel to each other and their mode fields overlap, light oscillates between the two waveguides along the propagation direction. To transfer light from one waveguide to another, several methods can be used including abrupt ending of a waveguide, bending away one waveguide or tapering one waveguide. Here we propose to use tapered SiN waveguide as it requires a shorter length compared to the other methods for light transferring from the glass waveguide to the SiN waveguide. The initial proposal is schematically illustrated in Figure 5.18. The NbN nanowire is evanescently coupled to the tapered SiN waveguide which is evanescently coupled to the glass waveguide.

The simulation result is illustrated in Figure 5.19. The left figure is for a tapered SiN waveguide located 1 μm above the glass waveguide, and has the parameters: thickness = 240 nm, W1 = 800 nm, W2 = 240 nm, W3 = 80 nm to 160 nm, L1 = 200 μm, L2 = vary along x

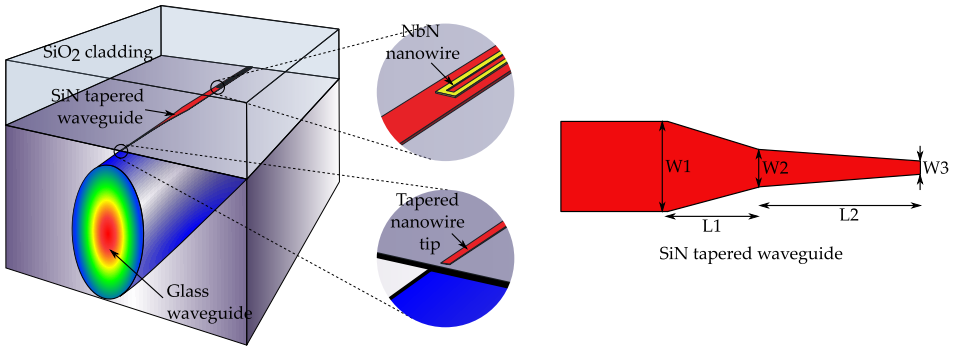

FIGURE 5.18: Schematic of NbN nanowire evanescently coupled to SiN waveguide evanescently coupled to Glass waveguide. SiN tapered waveguide dimensions are marked at different locations.

axis, $\Delta n_{glass} = 0.001$, diameter$_{\text{glass waveguide}}$ = 10 µm. As can be seen from the figure, coupling from the glass waveguide to the SiN waveguide can be >95% for taper region length ∼3 mm. The structure is not very sensitive to the variation of the taper tip width. The right figure is for the same parameters except the gap between the glass waveguide and SiN waveguide is 10 µm. It takes ∼2 cm long taper region to couple >90% of light from the glass waveguide and the structure is very sensitive to the variation of width of the taper tip.

Though the coupling can reach >90% from the glass waveguide to the SiN waveguide, some practical considerations suggest further improvement in the design. First of all, a larger gap between the waveguides makes the structure very sensitive to the dimensions of the taper region. A few nanometers variation can cause significant drop in the coupling efficiency. Secondly, smaller gap between the waveguides makes the structure more robust in terms of width variation, however, fabricating ∼3 mm long waveguide with 100-200 nm width is very challenging. Therefore, a further modified in the design is explored next.

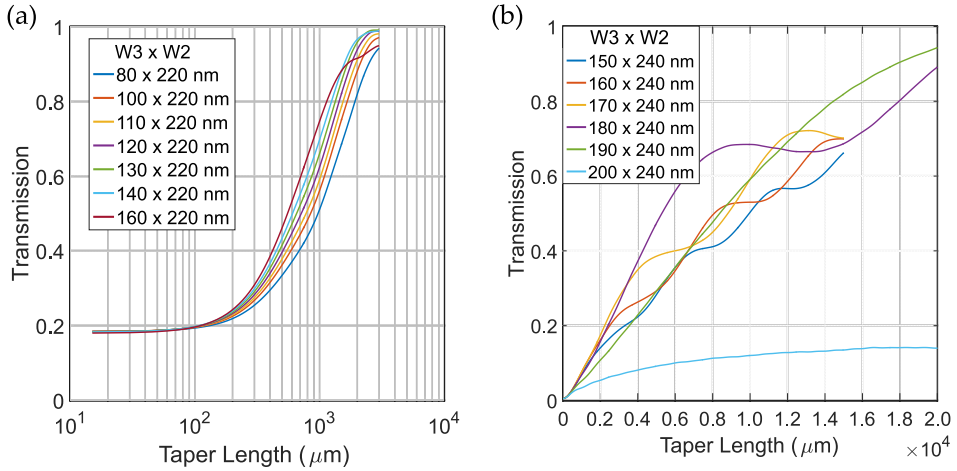

FIGURE 5.19: Coupling efficiency from glass waveguide to SiN tapered waveguide as a function of taper length. (left) distance between the waveguides = 1 µm and the parameters are: thickness = 240 nm, W1 = 800 nm, W2 = 240 nm, W3 = 80 nm to 160 nm, L1 = 200 µm, L2 = vary along x axis, $\Delta n_{glass} = 0.001$, diameter$_{\text{glass waveguide}}$ = 10 µm. (right) distance between the waveguides = 10 µm and the other parameters are identical.

5.5.2 NbN nanowire sandwiched between TiO_2 rib waveguide & TiO_2 interface layer on Glass substrate

In the new proposed design, a high-index interface layer would be used on top of glass substrate, and then a grating coupler would be used to couple light to a rib waveguide (illustrated in Figure 5.20). The grating coupler and the rib waveguide is also made of TiO_2. The NbN nanowire would be sandwiched between the rib waveguide and the interface layer.

The purpose of the high-index interface layer would be to bend the incoming light from glass waveguide, almost at a critical angle of refraction. We propose to use TiO_2 as the interface layer for its low absorption and high-index at the designed wavelength ($n_{TiO_2} \approx 2.5$ at $\lambda = 900\,nm$). From glass to TiO_2, the light would be refracted at $\sim 35°$, which would then be incident upon the grating coupler at the same angle. The proposed structure would be very robust against the glass waveguide fabrication variation, for example $5°$ deviation in glass waveguide angle would result in only $0.15°$ change in the refracted light. A disadvantage of the proposed design would be the need to fabricate a large area (cm long) grating coupler to collect most of the light. However, considering the pros and cons, the proposed design is a better choice that would have efficient coupling from the glass waveguide to the rib waveguide and the placement of the NbN nanowire in between two TiO_2 layers would absorb photons in a relatively short distance due to high intensity of the mode near the center of the rib waveguide.

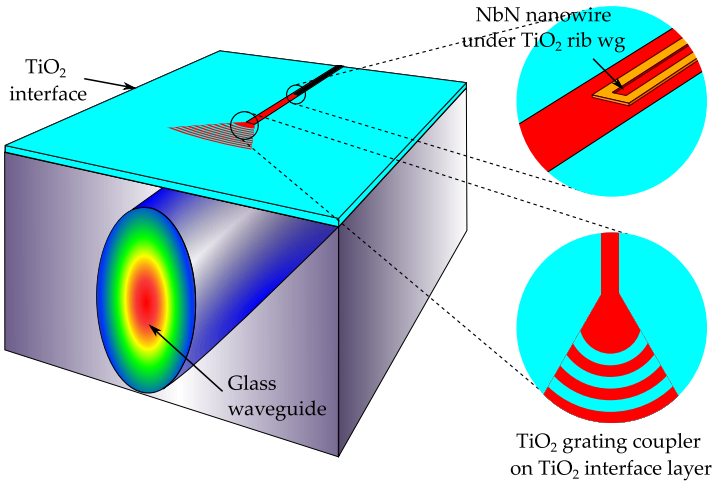

FIGURE 5.20: Schematic of NbN nanowire sandwiched between TiO_2 rib waveguide on TiO_2 interface layer on Glass substrate. Cyan and red both represents TiO_2. Red color is used for the grating coupler and rib waveguide for better visualization.

5.6 Fabrication progress and outlook

Optimizing the fabrication process for NbN deposition and nanowire formation is one of the major challenges for this project. In this chapter, after a brief description of the fabrication of laser written waveguides, the fabrication process developed for NbN nanowire formation and the future plan for integrating TiO_2 grating coupler rib waveguide atop the nanowire is described.

5.6.1 Direct Laser Writing of Waveguides in Fused Silica

We obtained the fused silica substrate inscribed with DLW waveguides from our collaborator A. Szameit's group at University of Jena. For fabricating the waveguides, 800 nm laser pulses with an energy of 300 nJ and a duration of ∼150 fs were focused into a polished fused silica substrate (Figure 5.21 (a)). The pulses were generated by a Ti:sapphire laser system with a repetition rate of 100 kHz. The depth of the focus inside the substrate can be varied as needed. For better coupling between the glass waveguide and the NbN nanowire detector, the waveguides were written very close to the surface (Figure 5.21 (b)).

The refractive index changes was determined by measuring the near-field profile (Figure 5.22 (a)) and solving the Helmholtz equation [128] at $\lambda = 633$ nm (Figure 5.22 (b)). The maximum index change calculated was $\Delta n = 8.7 \times 10^{-4}$ with a mode field diameter of ∼10 µm × 19 µm calculated from FWHM at $1/e^2$ intensity (Figure 5.22 (c, d)). The elliptical shaped waveguide is due to the nature of the Gaussian beam at the focus.

5.6.2 Fabrication of NbN nanowire

The fabrication of the NbN nanowire detectors is very challenging due to the high-sensitivity of their critical temperature to the process conditions and low-tolerance to the wire geometry variations. The SNSPD detectors are biased well below the T_c, so that the thermal noise doesn't affect the detector performance, and very close to the I_c, so that the absorbed photon can create a hotspot to yield high detection efficiency. Any imperfection in the thickness and/or in the width locally limits the I_c, which in turns affects the overall detector performance. Therefore, fabricating nanowires having constant thickness and width is very important.

Deposition of NbN film

The most commonly used technique for depositing NbN films is DC reactive megnetron sputtering. The basic principle is to ignite a plasma using argon, and then to introduce a small additional nitrogen flow to achieve the nitridation of a Nb target. Subsequent sputtering leads to the deposition of NbN onto the host substrate. The properties of the sputtered

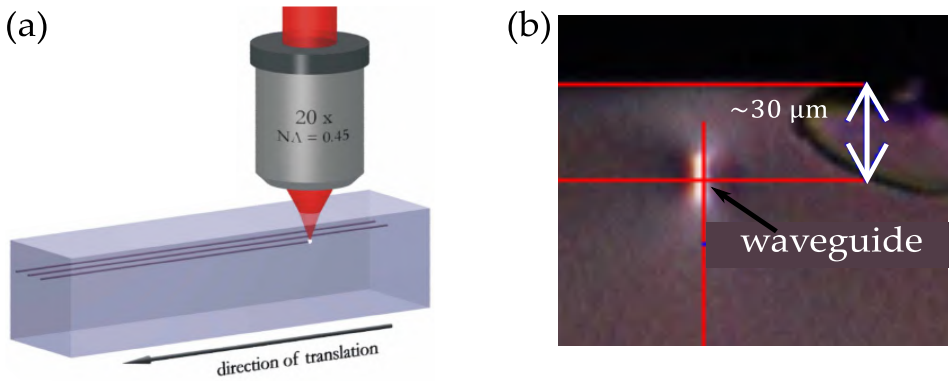

FIGURE 5.21: (a) Schematic of a direct laser writing inside a glass substrate [127]. (b) Microscope image of a glass waveguide ∼30 µm below the surface.

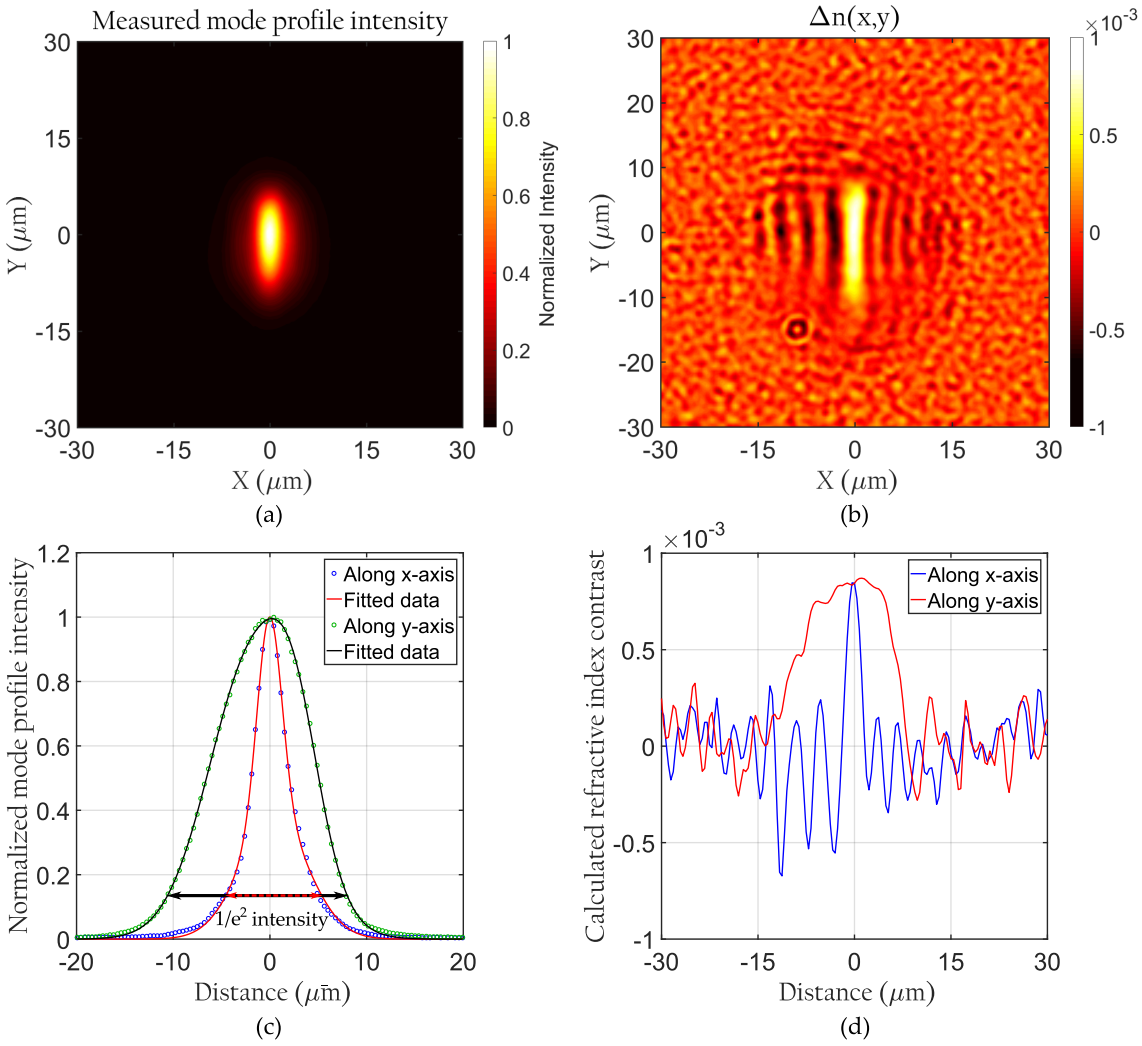

FIGURE 5.22: (a) Measured mode field intensity profile. (b) Calculated refractive index. (c) Measured data and fitted Gaussian for mode field profile along x and y direction. The FWHM at $1/e^2$ along x and y directions are respectively ∼10 µm and 19 µm. (d) Calculated refractive index contrast along x and y direction. The maximum index change was 8.7×10^{-4}.

film depend on various process parameters, such as argon pressure, nitrogen flow rate, substrate material and temperature. Along with the process conditions, the critical temperature is a strong function of the film thickness, especially below 10 nm. In Figure 5.23, the dependence of NbN critical temperature on Ar pressure, N_2 flow rate, substrate materials and film thickness are depicted.

The reduction in T_c for ultra-thin film, especially below 10 nm, is due to the proximity effect: this is the influence of a normal conducting layer on the superconducting film. Ultra-thin layer of superconducting films on a substrate can be modeled as a normalconductor-superconductor-normalconductor (NSN) layer system, with the normalconductor being the interface layer between the superconductor and the substrate and the oxide layers on the open surfaces. Changes in T_c on different substrates is caused by the lattice parameter mismatch issue; for example NbN lattice has a mismatch with Si of ∼20 %, with MgO ∼4 %,

with sapphire ∼9 % and with GaAs ∼23 %.

In this work, the NbN films were deposited on SiN_x film on Si substrates by DC reactive magnetron sputtering in a Plassys Bestek MP700S system at a base pressure of $\approx 6 \times 10^{-8}$ Torr. Initially the SiN_x film is being used rather than TiO_2 due to its availability. Sputtering was done at room temperature considering the possibility to use the same process for depositing NbN on bare optical fiber. Argon was flowed into the chamber at a rate of 30 sccm to a pressure of 3 mTorr along with nitrogen having 1.5 sccm flow rate. The deposition voltage and current was 350 V and 500 mA respectively. NbN films were deposited with a target thickness of 4 to 7 nm. The superconducting transition (T_c) measurements for these films were done using a dilution refrigerator and is illustrated in Figure 5.24. For the [4, 5, 6, 7] nm thick NbN film, T_c was measured as [5.6, 6.3, 7.7, 7.6] K. Process optimization is in progress to improve the T_c.

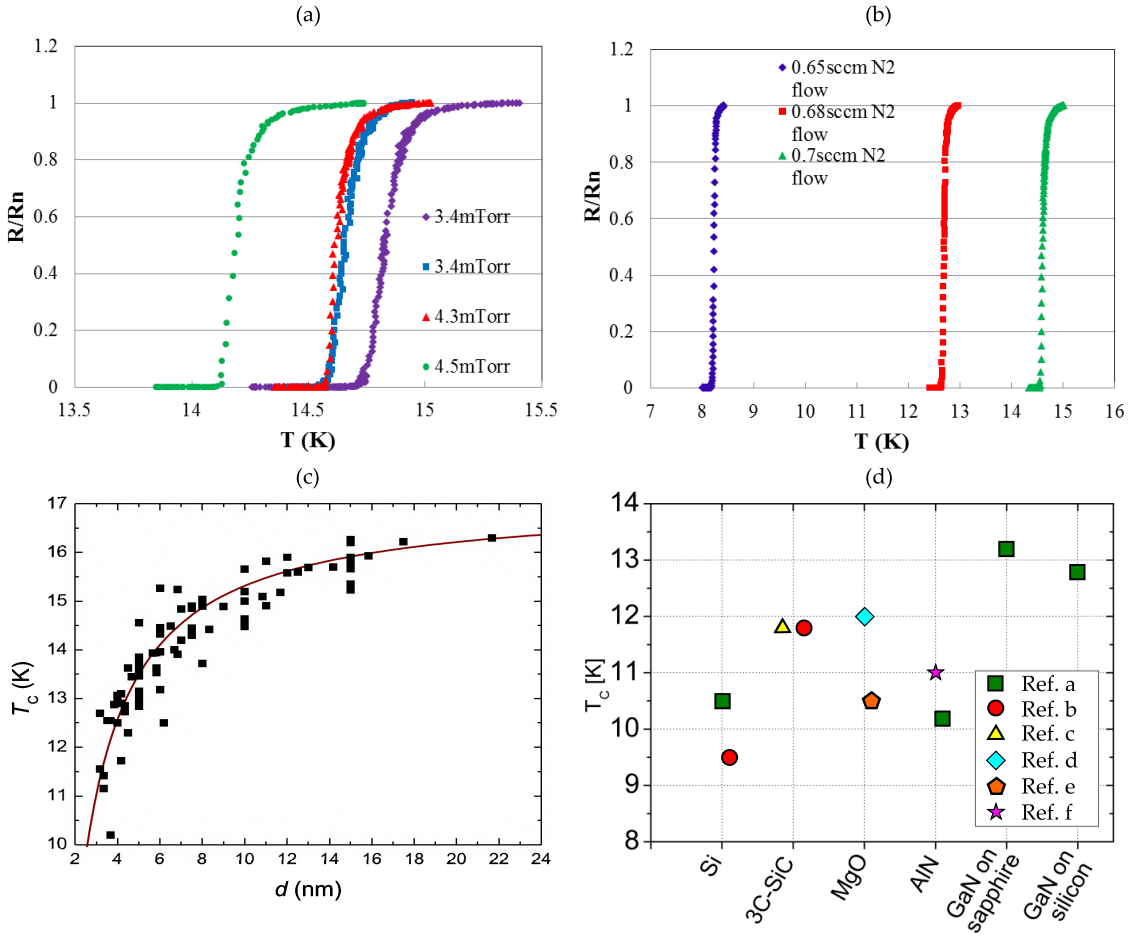

FIGURE 5.23: (a) Resistance vs. temperature plots for NbN films deposited on silicon nitride substrate with constant 0.7 sccm N_2 flow but different Ar pressures [129]. (b) Resistance vs. temperature plots for different N_2 flow rates at constant Ar pressure of 4.3 mTorr [129]. (c) Dependence of NbN critical temperature on the film thickness (substrate: polished R-plane sapphire, dep. temp.: 650°C) [130]. (d) Critical temperature variation of NbN films with thicknesses ranging from 3.5 to 6 nm grown on different buffer-layers. References [a-f] are respectively [131–136]

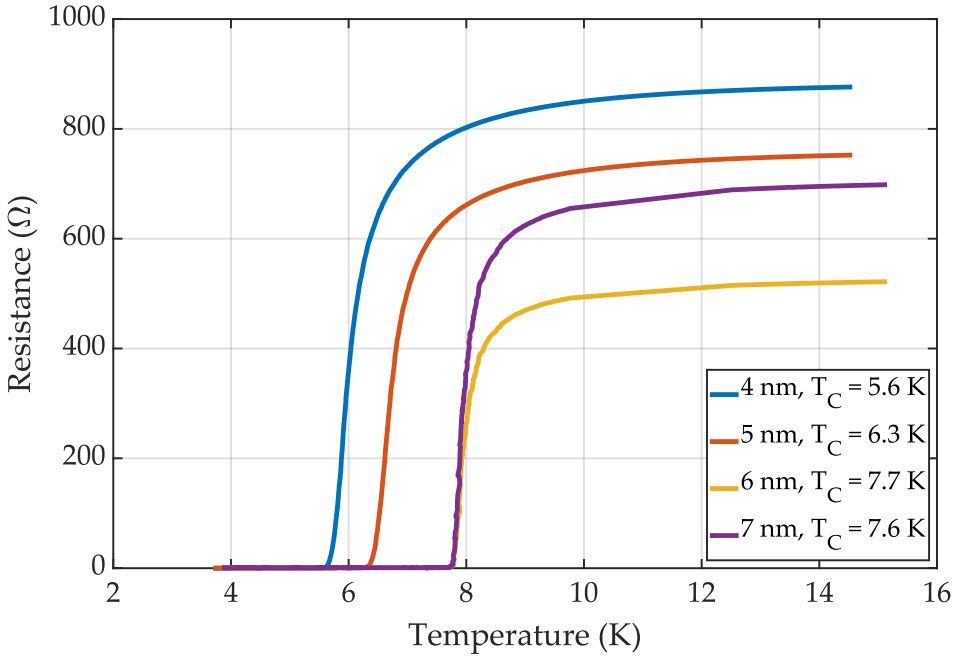

FIGURE 5.24: Resistance vs. temperature of different thickness NbN film on SiN_x film on Si substrate.

Formation of NbN nanowire using e-beam lithography

Patterning of a ∼100 nm wire on NbN imposes a unique set of challenges. Due to the detector's U-shaped geometry, a negative tone high resolution e-beam resist with good adhesion to the substrate is necessary. Initially Ma-N 2403 negative tone e-beam resist was tried but it has a poor adhesion. Hydrogen silsesquioxane (HSQ) is a good choice of resist capable of writing fine structures (< 10 nm) with excellent line edge roughness. However, after e-beam exposure, HSQ essentially turns into glass and subsequent removal requires a hydrofluoric acid dip or a CF_4 reactive ion etch (RIE), both can damage the underlying glass substrate and metallic thin film. Therefore, a HSQ/PMMA bilayer resist, in which HSQ acts as the negative tone e-beam resist top layer and PMMA acts as the sacrificial layer, was used to pattern the nanowire on NbN [137]. The bilayer resist process combines the high resolution and high etch resistivity of HSQ with an underlying PMMA layer that has good adhesion to the substrate and can be removed by using n-methyl-2-pyrrolidone (NMP) based solvent, such as Remover PG, or acetone which does not affect the NbN or glass substrate.

The fabrication steps of the HSQ/PMMA bilayer are illustrated on Figure 5.25. Starting with the SiN_x film atop Si substrate, standard solvent cleaning (acetone: 5 min., IPA: 5 min., water rinse: 2 min.) and O_2 plasma cleaning for 2 min. at 180°C was done. A 4 nm NbN film was deposited by DC magnetron sputtering on the fused silica substrate at room temperature. In the next step, 1% PMMA 950K in anisole (diluted from 6% PMMA 950k using anisole) was spun at 3000 rpm for 35 s, with 1500 rpm/s acceleration followed by a 20 min. bake at 180°C for a target thickness of ∼30 nm. Then 3% HSQ (XR-1541) in methyl isobutyl keton (diluted from 6% HSQ using 4-methyl-2-pentanone) was spun at 4000 rpm for 60 s, with 2250 rpm/s acceleration and baked at 110°C for 5 min. which produced ∼65 nm resist thickness. Immediately after that, HSQ was exposed under Raith 150TWO e-beam

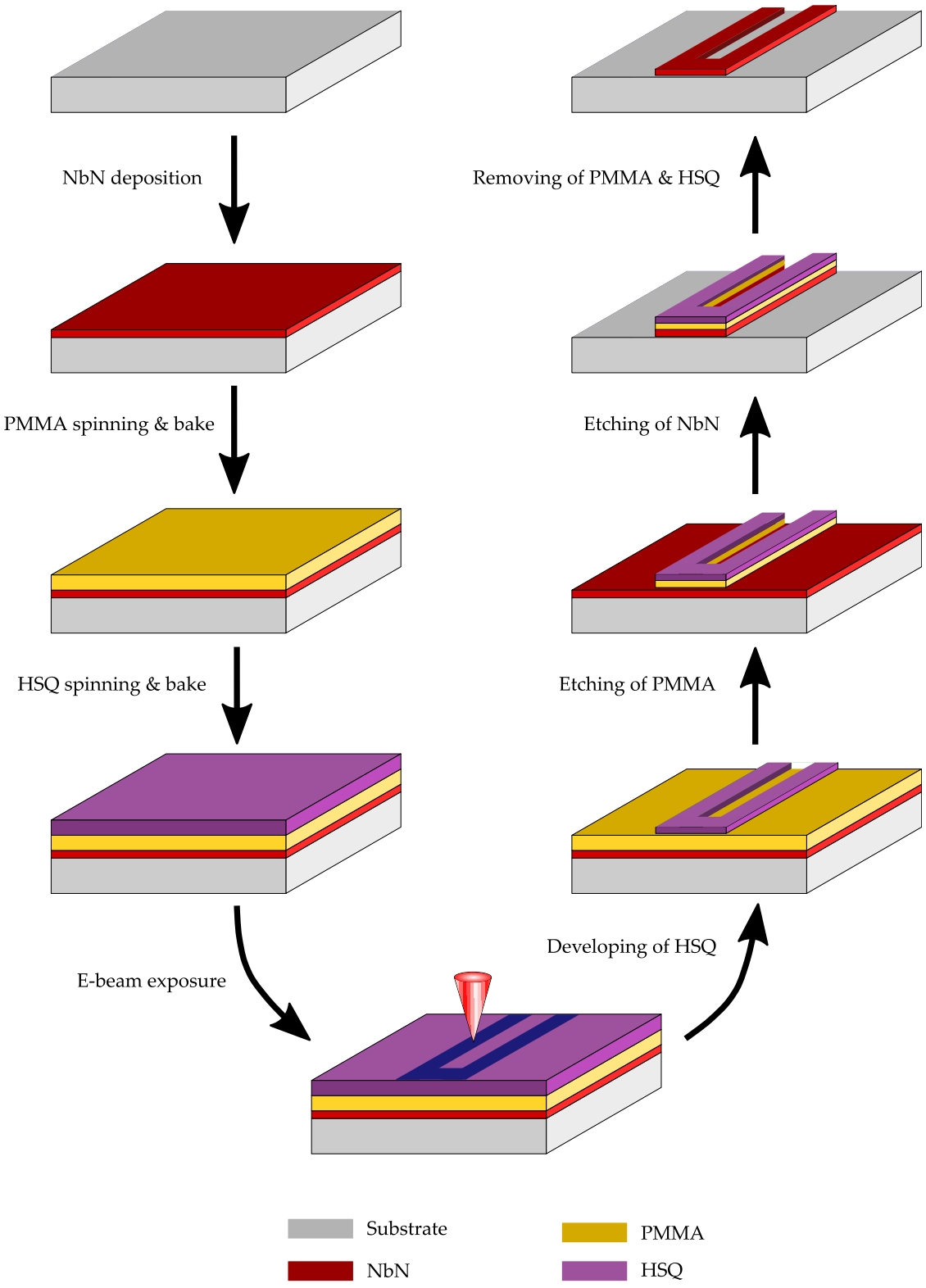

FIGURE 5.25: Fabrication steps of NbN nanowire formation.

lithography tool at 25 keV with an area dose of 510 µC/cm^2. The optimized dose was determined from a dose test where the area dose was varied from 400 - 700 µC/cm^2 and for the dose of 510 µC/cm^2, structure on HSQ resist yield the designed dimensions as the CAD file. Though the targeted dose was for HSQ at the top layer, but the e-beam also exposed the PMMA bottom layer which is a positive tone e-beam resist. Therefore HSQ developer to be used must not affect the exposed or unexposed PMMA bottom layer. Considering this, 2.45 % tetramethylammonium hydroxide (TMAH) in water (MF 319 developer) is a good choice that offers good resolution in HSQ without affecting the PMMA. As HSQ development is time sensitive, the exposed sample was developed using 2.45 % TMAH for 2 min., followed by a 2 min. rinse in deionized (DI) water promptly after the exposure.

Transferring the patterned nanowire on the PMMA layer from the HSQ layer was done by an O_2 plasma etch at a pressure of 100 mTorr, O_2 flow rate of 10 sccm, RF power of 100 W and temperature of 298 K. The etching rate was determined to be ∼18 nm/s for the PMMA and negligible effect on the HSQ. Pattern on the resist bilayer was transferred to the NbN thin film using a CF_4 RIE. In the next step, remover PG was used to remove the PMMA layer which in turn removed the HSQ layer and that left the NbN nanowire on the SiN_x film atop Si substrate.

The fabricated NbN nanowire is depicted in Figure 5.26 & 5.27. The structure has 4 contact pads with 100 µm × 100 µm dimension for 4-probe measurement, 2 for current injection and 2 for measuring voltage. This particular nanowire is ∼110 nm wide with ∼100 nm gap in between them and ∼480 µm long written using a 500 µm × 200 µm write field. The most common write field used in Raith 150TWO system is 100 µm × 100 µm write field, but to avoid stitching error in the nanowire segment, a larger write field is used. Due to the beam deflection in the large write field, the width of the nanowire has increased ∼10% near the edge of the write field.

The superconducting transition measurement was performed for the fabricated nanowire with 4 nm thick film. Though the 4 nm thick film was superconducting, however, the 100 nm wide nanowire made out of the film was not always superconducting. Therefore, optimization of the fabrication steps for a consistent superconducting nanowire is in progress.

5.6.3 Fabrication outlook

The overview of the fabrication steps would be following:

1. Formation of laser written glass waveguide in the glass substrate. The waveguide is written not very close to the surface, rather $\sim 100\,\mu m$ below the surface. Writing very close to the surface results in a high-loss waveguide.
2. Etch necessary amount of top glass surface to get closer to the glass waveguide.
3. Deposit $\sim \mu m$ thick layer of TiO_2 as an interface layer.
4. Deposit NbN thin film
5. Formation of NbN nanowire
6. Deposit $\sim \mu m$ thick TiO_2 layer.
7. Formation of grating coupler and rib waveguide on top of NbN nanowire.

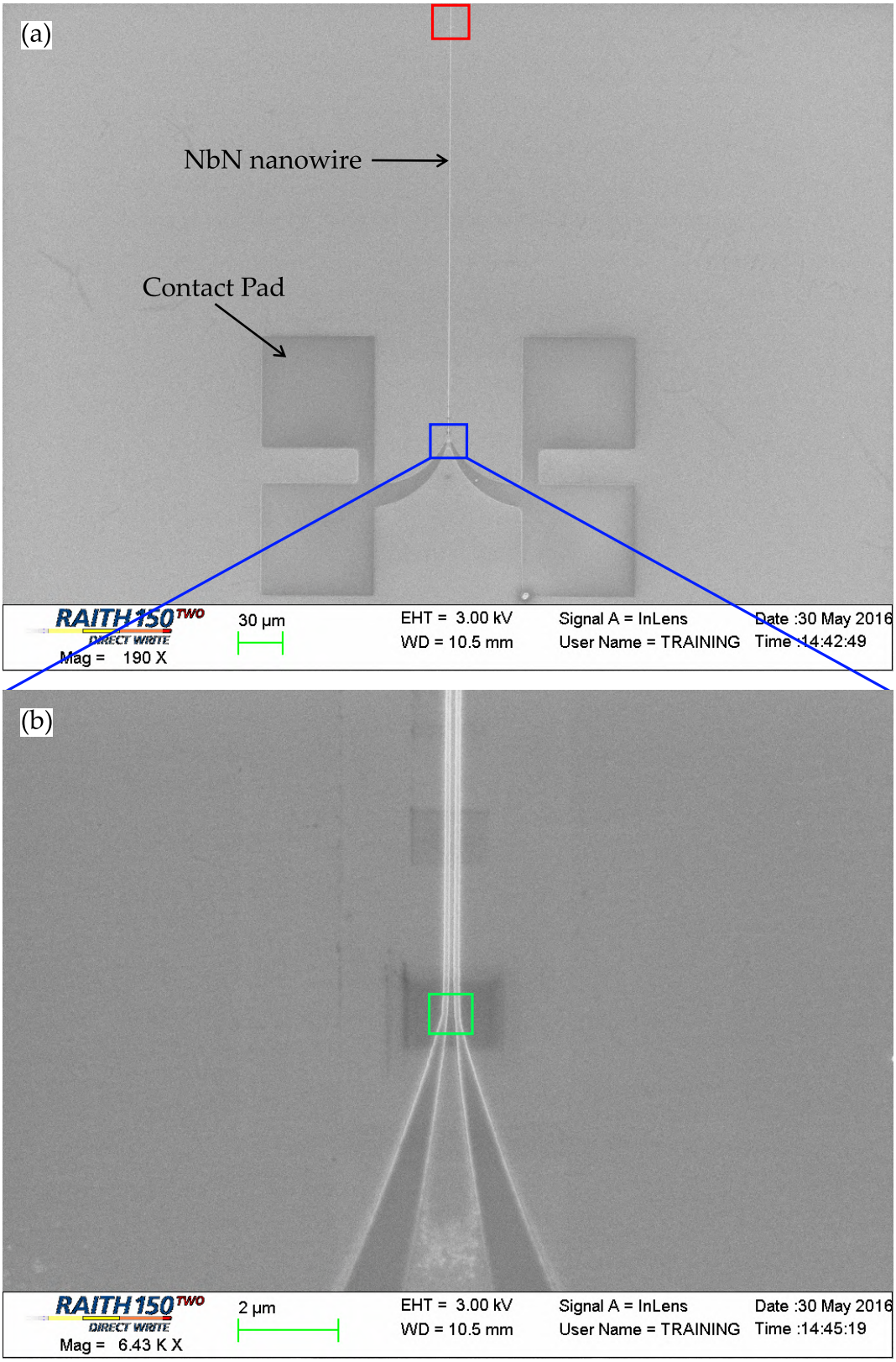

FIGURE 5.26: (a) Superconducting nanowire (∼480 µm long) for a single-photon detector made using NbN. (b) Neck of the nanowire. Zoomed in at red (green) square is depicted in the next page with red (green) frame.

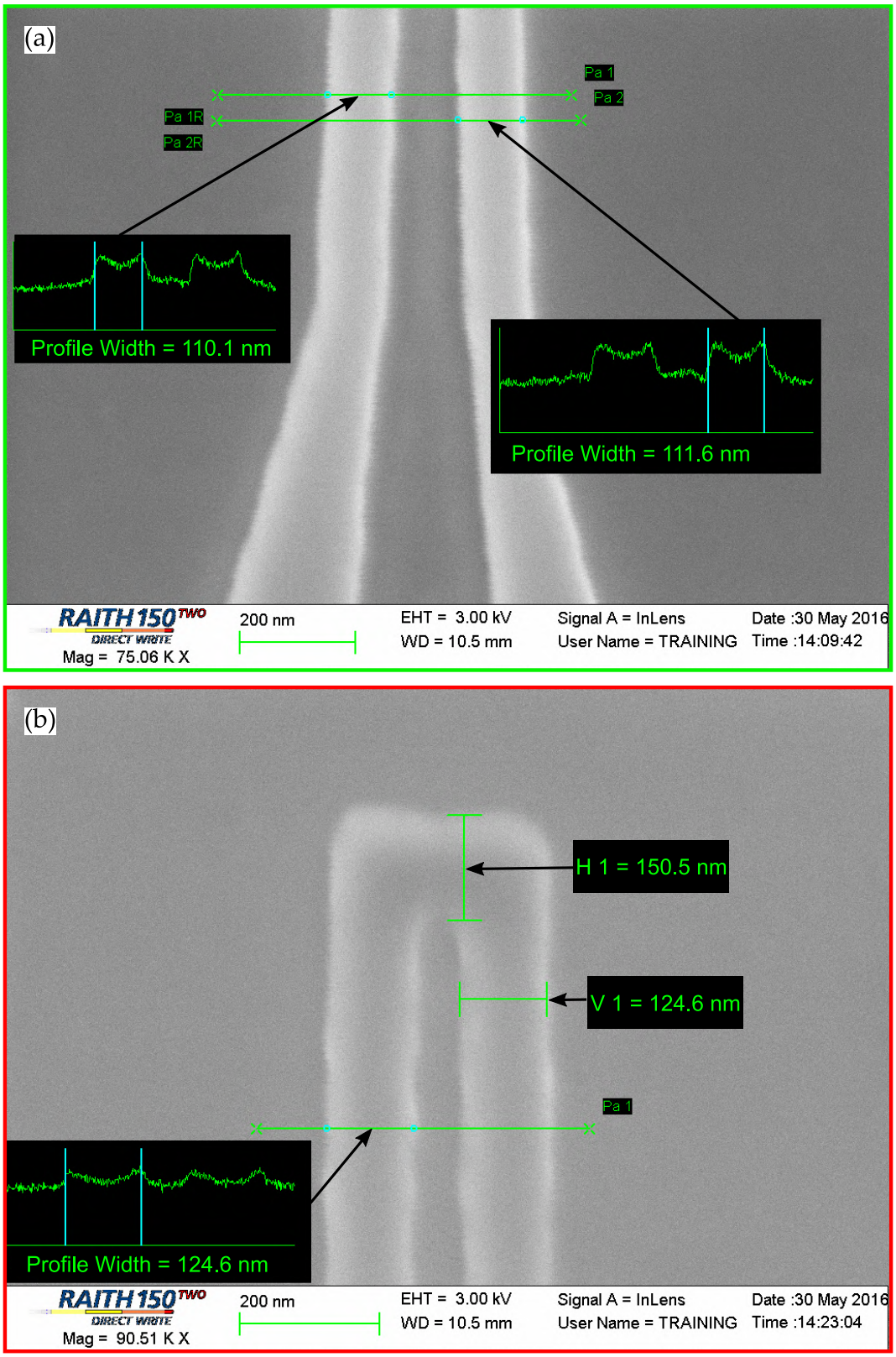

FIGURE 5.27: (a) ∼110 nm wide nanowire with ∼100 nm gap in between them. (b) Top of the nanowire. The width has increased ∼10% due to large write field.

5.7 Conclusion

In this work, we report the progress in design and fabrication of a superconducting nanowire single photon detector on glass substrate that could potentially be integrated with 3D photonic lattices. This device can be a step forward towards the on-chip manipulation and detection of photons on glass platform.

Chapter 6

Conclusions and Outlook

The work presented in this thesis explores the integration and interfacing of a variety of photonics devices with optical waveguides, aiming to minimize the optical losses and physical footprint, as well as to improve other aspects of such systems. The specific investigations include interfacing solid-core and hollow-core optical fibers, development of a monolithic single-photon source based on a quantum dot embedded in a semiconductor nanowire aligned with a single-mode fiber, a proposal for a waveguide-integrated power limiter that can protect detectors in a quantum key distribution (QKD) network, and integrating superconducting-nanowire single photon detectors (SNSPD) with laser-written waveguides. The outcomes of these investigations can be summarized as follows::

1. The on-chip fiber splicer offers an excellent alternative to fusion splicing for applications where a connection between solid-core fiber and HCPCF is needed, such as fiber-integrated cavities and spectroscopy cells and cold atomic ensemble in a HCPCF. The maximum observed efficiencies from a SC SMF to HCPCF is 90% and from a HCPCF to a SC SMF is 80%. Efficiency between conventional SMFs can be as high as $\sim$100% with the inclusion of index matching liquid at the joint region. Additionally, a relatively high coupling efficiency is maintained even when a gap is introduced between the two fiber ends and the coupling in the presence of a gap could be further improved by fabricating a lens at the fiber tip. Having such a gap can be potentially utilized for lab-on-a-chip applications [53, 54] in which the gap would be combined with microchannels to introduce liquids or gases into the HCPCF or anti-resonant reflecting optical waveguide (ARROW) for probing by tightly-confined guided light.

2. The proposed design protocol for fiber coupled single photon source based on quantum dot embedded in a semiconductor nanowire could potentially achieve an overall collection efficiency of $\sim$40% to the SMF. Addition of a reflective surface, like gold, at the bottom could potentially increase the efficiency by a factor of 2. Possible fabrication variations, their effect on the collection efficiency and necessary measures to minimize them was also discussed. We also report the fabrication progress towards the proof-of-concept device. Successful demonstration could be a significant improvement towards fiber integrated single photon source.

3. The proposed solid state optical power limiter offers protection against both intentional and accidental damage from high power signal and could be used in specialized applications including quantum cryptography, as well as other areas of photonics which require such functionality. The proposed device's cut-off intensity and bandwidth can be varied by changing the mirror reflectivity, and very narrow bandwidth (sub-nm) can be achieved with highly reflective mirrors. The peak transmission roll off after the

cut-off is -20 dB/decade which is independent of the mirror reflectivity. Two possible fabrication plans are proposed, one is with vertical stacking where the optical axis is perpendicular to the device plane and the other one is a planar structure where the optical axis is in plane of the device.

4. The progress in design and fabrication of a superconducting nanowire single photon detector integrated with DLW glass waveguides is reported that could potentially be integrated with DLW photonic lattices. This device could potentially be a step forward towards the goal of making this platform fully on-chip.

6.1 Future Directions

For the on-chip splicer, a few immediate applications are in progress. Use of the splicer for coupling light between SMF and HCPCF containing cold atomic ensemble could potentially increase the coupling efficiency >85% compared to the present efficiency of <40%. Fiber integrated cavity consists of different types of fibers and mirrors have several potential applications including spectroscopy cells and further enhancing light-matter interactions in HCPCF. Especially potential inclusion of photonic crystal mirror [52], polarization sensitive mirror, and spin-preserving chiral photonic crystal mirror [138] cavity in HCPCF integrated with SMF would allow higher atom-photon interaction probability along with efficient coupling of fibers. One of the major challenges of fabricating the photonic crystal mirror integrated HCPCF cavity is the mounting technique of mirrors onto the HCPCF. Therefore, an efficient mirror mounting protocol should be developed for achieving good cavities. SMF integrated HCPCF cavity could have potential applications in fiber integrated lasers [139].

For the fiber integrated QD nanowire, fabrication progress such as integration of GRIN fiber with SMF and proof of concept of SU-8 fiber alignment structure have been demonstrated. Future progress should be directed towards optimizing the integrated SMF —Coreless fiber —GRIN fiber lens for desired spot size and focal distance. Possibility of inclusion of melted tip lens could be investigated if additional tight focusing is required. Fiber alignment structure should be optimized with thicker (>100 µm) resist for better alignment of the fiber. Sub-micron fabrication tolerance, especially in the transverse direction, should be achieved. Appropriate alignment marker could be used to achieve such precision. Lastly, proper mounting of the fiber into the alignment structure should be developed. A precision micro-manipulator could be used to guide the fiber and UV-cured adhesive could be used to hold the fiber at the desired position.

For the OPL integrated optical filter, one of the major challenges in fabricating the device is the integration of GaAs with Si based dielectric. Depending on the availability of GaAs chip or access to MBE growth facility for GaAs, either the in-plane or out-of-plane structure could be pursued. If access to MBE growth facility is available, the vertical stacking structure could be used for demonstrating the proof of concept. Otherwise, off the shelf GaAs chip could be used to fabricate the in-plane structure for the device.

For the SNSPD integrated with DLW waveguides, future work could be divided into a few key milestones. First of all, further simulation should be done for better estimation of the coupling from the DLW waveguides to the TiO_2 grating coupler integrated rib waveguide. Secondly, experimental demonstration of light being coupled from DLW waveguide to

TiO_2 rib waveguide should be achieved. Thirdly, though the 4 nm thick NbN film was superconducting, however, the 100 nm wide nanowire made out of the film was not always superconducting. Therefore optimizing the fabrication steps for a consistent superconducting nanowire is necessary. After that, demonstration of a working SNSPD should be achieved. And lastly, full integration of SNSPD with DLW waveguides should be done to demonstrate the final milestone of a high efficiency SNSPD integrated with DLW waveguide platform.

Bibliography

[1] H Jeff Kimble. "The quantum internet". In: *Nature* 453.7198 (2008), pp. 1023–1030.

[2] Gabriele Bulgarini et al. "Nanowire waveguides launching single photons in a Gaussian mode for ideal fiber coupling". In: *Nano letters* 14.7 (2014), pp. 4102–4106.

[3] Lars Lydersen et al. "Hacking commercial quantum cryptography systems by tailored bright illumination". In: *Nature photonics* 4.10 (2010), p. 686.

[4] Vadim Makarov et al. "Creation of backdoors in quantum communications via laser damage". In: *Physical Review A* 94.3 (2016), p. 030302.

[5] Andrea Crespi et al. "Integrated photonic quantum gates for polarization qubits". In: *Nature communications* 2.1 (2011), pp. 1–6.

[6] Kali P Nayak et al. "Nanofiber quantum photonics". In: *Journal of Optics* 20.7 (2018), p. 073001.

[7] A Goban et al. "Atom–light interactions in photonic crystals". In: *Nature communications* 5.1 (2014), pp. 1–9.

[8] Saikat Ghosh et al. "Low-light-level optical interactions with rubidium vapor in a photonic band-gap fiber". In: *Physical review letters* 97.2 (2006), p. 023603.

[9] Joo Hin Chong et al. "An effective splicing method on photonic crystal fiber using CO 2 laser". In: *IEEE Photonics Technology Letters* 15.7 (2003), pp. 942–944.

[10] Andrew D Yablon and Ryan Bise. "Low-loss high-strength microstructured fiber fusion splices using GRIN fiber lenses". In: *Optical Fiber Communication Conference*. Optical Society of America. 2004, MF14.

[11] R Thapa et al. "Arc fusion splicing of hollow-core photonic bandgap fibers for gas-filled fiber cells". In: *Optics Express* 14.21 (2006), pp. 9576–9583.

[12] Limin Xiao et al. "Fusion splicing photonic crystal fibers and conventional single-mode fibers: microhole collapse effect". In: *Journal of lightwave technology* 25.11 (2007), pp. 3563–3574.

[13] MLV Tse et al. "Fusion splicing holey fibers and single-mode fibers: a simple method to reduce loss and increase strength". In: *IEEE Photonics Technology Letters* 21.3 (2009), pp. 164–166.

[14] Tao Zhu et al. "Pressure-assisted low-loss fusion splicing between photonic crystal fiber and single-mode fiber". In: *Optics express* 20.22 (2012), pp. 24465–24471.

[15] Vinod Parmar, Randhir Bhatnagar, and Pawan Kapur. "Optimized butt coupling between single mode fiber and hollow-core photonic crystal fiber". In: *Optical Fiber Technology* 19.5 (2013), pp. 490–494.

[16] David Hunger et al. "A fiber Fabry–Perot cavity with high finesse". In: *New Journal of Physics* 12.6 (2010), p. 065038.

[17] Xiyuan Liu et al. "Fabrication of alignment structures for a fiber resonator by use of deep-ultraviolet lithography". In: *Applied optics* 44.32 (2005), pp. 6857–6860.

[18] H Jeff Kimble, Mario Dagenais, and Leonard Mandel. "Photon antibunching in resonance fluorescence". In: *Physical Review Letters* 39.11 (1977), p. 691.

[19] Frank Diedrich and Herbert Walther. "Nonclassical radiation of a single stored ion". In: *Physical review letters* 58.3 (1987), p. 203.

[20] Th Basché et al. "Photon antibunching in the fluorescence of a single dye molecule trapped in a solid". In: *Physical review letters* 69.10 (1992), p. 1516.

[21] Michael E Reimer et al. "Bright single-photon sources in bottom-up tailored nanowires". In: *Nature communications* 3 (2012), p. 737.

[22] Xing Ding et al. "On-demand single photons with high extraction efficiency and near-unity indistinguishability from a resonantly driven quantum dot in a micropillar". In: *Physical review letters* 116.2 (2016), p. 020401.

[23] Niccolo Somaschi et al. "Near-optimal single-photon sources in the solid state". In: *Nature Photonics* 10.5 (2016), p. 340.

[24] Luca Sapienza et al. "Nanoscale optical positioning of single quantum dots for bright and pure single-photon emission". In: *Nature communications* 6 (2015), p. 7833.

[25] Julien Claudon et al. "A highly efficient single-photon source based on a quantum dot in a photonic nanowire". In: *Nature Photonics* 4.3 (2010), p. 174.

[26] Eleana Makri, Tsampikos Kottos, and Ilya Vitebskiy. "Reflective optical limiter based on resonant transmission". In: *Physical Review A* 91.4 (2015), p. 043838.

[27] Jarrett H Vella et al. "Experimental realization of a reflective optical limiter". In: *Physical Review Applied* 5.6 (2016), p. 064010.

[28] Rodion Kononchuk et al. "Photonic limiters with enhanced dynamic range". In: *Components and Packaging for Laser Systems IV*. Vol. 10513. International Society for Optics and Photonics. 2018, 105130W.

[29] Roney Thomas, Ilya Vitebskiy, and Tsampikos Kottos. "Resonant cavities with phase-changing materials". In: *Optics letters* 42.23 (2017), pp. 4784–4787.

[30] N Antonellis et al. "Nonreciprocity in Photonic Structures with Phase-Change Components". In: *Physical Review Applied* 11.2 (2019), p. 024046.

[31] Zheng Wu, Mengxi Ji, and Yi Wang. "Ultra low threshold optical power limiter based on a silicon photonic crystal cavity". In: *Conference on Lasers and Electro-Optics/Pacific Rim*. Optical Society of America. 2015, 26C1_6.

[32] Siqi Yan et al. "Chip-integrated optical power limiter based on an all-passive microring resonator". In: *Scientific reports* 4 (2014), p. 6676.

[33] K Miura Davis et al. "Writing waveguides in glass with a femtosecond laser". In: *Optics letters* 21.21 (1996), pp. 1729–1731.

[34] G Della Valle, R Osellame, and P Laporta. "Micromachining of photonic devices by femtosecond laser pulses". In: *Journal of Optics A: Pure and Applied Optics* 11.1 (2008), p. 013001.

[35] Won-Jong Kang et al. "Novel exposure methods based on reflection and refraction effects in the field of SU-8 lithography". In: *Journal of Micromechanics and Microengineering* 16.4 (2006), pp. 821–831.

[36] R Feng and RJ Farris. "The characterization of thermal and elastic constants for an epoxy photoresist SU8 coating". In: *Journal of Materials Science* 37.22 (2002), pp. 4793–4799.

[37] Herwig Kogelnik. "Coupling and conversion coefficients for optical modes". In: *Symposium in quasi optics*. Polytechnic Press. 1964, pp. 333–347.

[38] Thorlab. *Hollow Core Photonic Crystal Fibers*. https://www.thorlabs.com/newgrouppage9.cfm?objectgroup_id=912.

[39] Taehyun Yoon and Michal Bajcsy. "Laser-cooled cesium atoms confined with a magic-wavelength dipole trap inside a hollow-core photonic-bandgap fiber". In: *Physical Review A* 99.2 (2019), p. 023415.

[40] Michal Bajcsy et al. "Efficient all-optical switching using slow light within a hollow fiber". In: *Physical review letters* 102.20 (2009), p. 203902.

[41] Frank Blatt et al. "Stationary light pulses and narrowband light storage in a laser-cooled ensemble loaded into a hollow-core fiber". In: *Physical Review A* 94.4 (2016), p. 043833.

[42] Vivek Venkataraman, Kasturi Saha, and Alexander L Gaeta. "Phase modulation at the few-photon level for weak-nonlinearity-based quantum computing". In: *Nature Photonics* 7.2 (2013), p. 138.

[43] MR Sprague et al. "Broadband single-photon-level memory in a hollow-core photonic crystal fibre". In: *Nature Photonics* 8.4 (2014), pp. 287–291.

[44] Ewelina Obrzud, Steve Lecomte, and Tobias Herr. "Temporal solitons in microresonators driven by optical pulses". In: *Nature Photonics* 11.9 (2017), p. 600.

[45] Scott M Hendrickson, Todd B Pittman, and James D Franson. "Microcavities using holey fibers". In: *Journal of lightwave technology* 25.10 (2007), pp. 3068–3071.

[46] Nanfang Yu and Federico Capasso. "Flat optics with designer metasurfaces". In: *Nature materials* 13.2 (2014), pp. 139–150.

[47] Amir Arbabi et al. "Dielectric metasurfaces for complete control of phase and polarization with subwavelength spatial resolution and high transmission". In: *Nature nanotechnology* 10.11 (2015), p. 937.

[48] JP Balthasar Mueller et al. "Metasurface polarization optics: independent phase control of arbitrary orthogonal states of polarization". In: *Physical Review Letters* 118.11 (2017), p. 113901.

[49] Shanhui Fan and John D Joannopoulos. "Analysis of guided resonances in photonic crystal slabs". In: *Physical Review B* 65.23 (2002), p. 235112.

[50] Connie J Chang-Hasnain and Weijian Yang. "High-contrast gratings for integrated optoelectronics". In: *Advances in Optics and Photonics* 4.3 (2012), pp. 379–440.

[51] Onur Kilic et al. "Miniature photonic-crystal hydrophone optimized for ocean acoustics". In: *The Journal of the Acoustical Society of America* 129.4 (2011), pp. 1837–1850.

[52] Jeremy Flannery et al. "Fabry-pérot cavity formed with dielectric metasurfaces in a hollow-core fiber". In: *ACS Photonics* 5.2 (2018), pp. 337–341.

[53] Holger Schmidt and Aaron R Hawkins. "The photonic integration of non-solid media using optofluidics". In: *Nature photonics* 5.10 (2011), pp. 598–604.

[54] Xudong Fan and Ian M White. "Optofluidic microsystems for chemical and biological analysis". In: *Nature photonics* 5.10 (2011), pp. 591–597.

[55] Matthew D Eisaman et al. "Invited review article: Single-photon sources and detectors". In: *Review of scientific instruments* 82.7 (2011), p. 071101.

[56] Pascale Senellart, Glenn Solomon, and Andrew White. "High-performance semiconductor quantum-dot single-photon sources". In: *Nature nanotechnology* 12.11 (2017), p. 1026.

[57] Michael E Reimer and Catherine Cher. "The quest for a perfect single-photon source". In: *Nature Photonics* 13.11 (2019), pp. 734–736.

[58] Alan Migdall et al. *Single-photon generation and detection: physics and applications*. Vol. 45. Academic Press, 2013, p. 31.

[59] Igor Aharonovich, Dirk Englund, and Milos Toth. "Solid-state single-photon emitters". In: *Nature Photonics* 10.10 (2016), p. 631.

[60] Hui Wang et al. "Towards optimal single-photon sources from polarized microcavities". In: *Nature Photonics* 13.11 (2019), pp. 770–775.

[61] Henrik Mäntynen et al. "Single-photon sources with quantum dots in III–V nanowires". In: *Nanophotonics* 8.5 (2019), pp. 747–769.

[62] Klaus D Jöns et al. "Bright nanoscale source of deterministic entangled photon pairs violating Bell's inequality". In: *Scientific Reports* 7.1 (2017), pp. 1–11.

[63] Simon Daley. "Electro-optic rotating half-waveplate for a quantum dot fine-structure eraser". MA thesis. University of Waterloo, 2019.

[64] WL Emkey and C Jack. "Analysis and evaluation of graded-index fiber lenses". In: *Journal of Lightwave Technology* 5.9 (1987), pp. 1156–1164.

[65] H. Kogelnik. "Imaging of optical modes — resonators with internal lenses". In: *The Bell System Technical Journal* 44.3 (1965), pp. 455–494.

[66] R. Kishimoto and M. Koyama. "Coupling Characteristics Between Single-Mode Fiber and Square Law Medium". In: *IEEE Transactions on Microwave Theory and Techniques* 30.6 (1982), pp. 882–893.

[67] DG Hall, RR Rice, and JD Zino. "Simple Gaussian-beam model for GaAlAs double-heterostructure laser-diode-to-diffused-waveguide coupling calculations". In: *Optics letters* 4.9 (1979), pp. 292–294.

[68] Alvaro Mata, Aaron J Fleischman, and Shuvo Roy. "Fabrication of multi-layer SU-8 microstructures". In: *Journal of micromechanics and microengineering* 16.2 (2006), p. 276.

[69] Akihiro Fushimi and Takasumi Tanabe. "All-optical logic gate operating with single wavelength". In: *Optics express* 22.4 (2014), pp. 4466–4479.

[70] Kengo Nozaki et al. "Ultralow-power all-optical RAM based on nanocavities". In: *Nature Photonics* 6.4 (2012), p. 248.

[71] Eiichi Kuramochi et al. "Large-scale integration of wavelength-addressable all-optical memories on a photonic crystal chip". In: *Nature Photonics* 8.6 (2014), p. 474.

[72] Cuicui Lu et al. "Chip-integrated ultrawide-band all-optical logic comparator in plasmonic circuits". In: *Scientific reports* 4.1 (2014), pp. 1–8.

[73] NQ Ngo et al. "A new theoretical basis of higher-derivative optical differentiators". In: *Optics Communications* 230.1-3 (2004), pp. 115–129.

[74] Jing Xu et al. "High-speed all-optical differentiator based on a semiconductor optical amplifier and an optical filter". In: *Optics letters* 32.13 (2007), pp. 1872–1874.

[75] Fangfei Liu et al. "Compact optical temporal differentiator based on silicon microring resonator". In: *Optics Express* 16.20 (2008), pp. 15880–15886.

[76] Jianji Dong et al. "Compact, flexible and versatile photonic differentiator using silicon Mach-Zehnder interferometers". In: *Optics express* 21.6 (2013), pp. 7014–7024.

[77] M Ferrera et al. "On-chip CMOS-compatible all-optical integrator". In: *Nature communications* 1.1 (2010), pp. 1–5.

[78] Marcello Ferrera et al. "All-optical 1st and 2nd order integration on a chip". In: *Optics express* 19.23 (2011), pp. 23153–23161.

[79] Nikolay L Kazanskiy and Pavel G Serafimovich. "Coupled-resonator optical waveguides for temporal integration of optical signals". In: *Optics Express* 22.11 (2014), pp. 14004–14013.

[80] Sisi Tan et al. "All-optical computation system for solving differential equations based on optical intensity differentiator". In: *Optics express* 21.6 (2013), pp. 7008–7013.

[81] Sisi Tan et al. "High-order all-optical differential equation solver based on microring resonators". In: *Optics letters* 38.19 (2013), pp. 3735–3738.

[82] Ting Yang et al. "All-optical differential equation solver with constant-coefficient tunable based on a single microring resonator". In: *Scientific reports* 4 (2014), p. 5581.

[83] Herman Van de Stadt and Johan M Muller. "Multimirror Fabry–Perot interferometers". In: *JOSA A* 2.8 (1985), pp. 1363–1370.

[84] Chunfei Li. *Nonlinear optics: principles and applications*. Springer, 2016.

[85] Andrea Ballabio et al. "GaAs epilayers grown on patterned (001) silicon substrates via suspended Ge layers". In: *Scientific reports* 9.1 (2019), pp. 1–8.

[86] Robert H Hadfield and Göran Johansson. *Superconducting Devices in Quantum Optics*. Springer, 2016.

[87] Shigehito Miki et al. "High performance fiber-coupled NbTiN superconducting nanowire single photon detectors with Gifford-McMahon cryocooler". In: *Optics express* 21.8 (2013), pp. 10208–10214.

[88] Wolfram HP Pernice et al. "High-speed and high-efficiency travelling wave single-photon detectors embedded in nanophotonic circuits". In: *Nature communications* 3 (2012), p. 1325.

[89] Christopher J Chunnilall et al. "Metrology of single-photon sources and detectors: a review". In: *Optical Engineering* 53.8 (2014), pp. 081910–081910.

[90] George A Morton. "Photomultipliers for scintillation counting". In: *RCA Rev.* 10 (1949).

[91] URL: https://en.wikipedia.org/wiki/Photomultiplier.

[92] URL: https://www.hamamatsu.com/resources/pdf/etd/PMT_handbook_v3aE.pdf.

[93] URL: https://www.hamamatsu.com/resources/pdf/etd/m-h7422e.pdf.

[94] S Cova et al. "Evolution and prospects for single-photon avalanche diodes and quenching circuits". In: *Journal of modern optics* 51.9-10 (2004), pp. 1267–1288.

[95] Robert H Hadfield. "Single-photon detectors for optical quantum information applications". In: *Nature photonics* 3.12 (2009), pp. 696–705.

[96] URL: https://www.lasercomponents.com/us/product/count-t/.

[97] Sara Pellegrini et al. "Design and performance of an InGaAs-InP single-photon avalanche diode detector". In: *arXiv preprint quant-ph/0605042* (2006).

[98] URL: http://www.micro-photon-devices.com/Docs/Datasheet/InGaAs_Datasheet.pdf.

[99] URL: http://www.idquantique.com/photon-counting/photon-counting-modules/id230/.

[100] Marius A Albota and Franco NC Wong. "Efficient single-photon counting at 1.55 μm by means of frequency upconversion". In: *Optics letters* 29.13 (2004), pp. 1449–1451.

[101] Aaron P Vandevender and Paul G Kwiat. "High efficiency single photon detection via frequency up-conversion". In: *Journal of Modern Optics* 51.9-10 (2004), pp. 1433–1445.

[102] Carsten Langrock et al. "Highly efficient single-photon detection at communication wavelengths by use of upconversion in reverse-proton-exchanged periodically poled LiNbO 3 waveguides". In: *Optics letters* 30.13 (2005), pp. 1725–1727.

[103] Lijun Ma, Oliver Slattery, and Xiao Tang. *Single Photon Detection Using Frequency Up-Conversion with Pulse Pumping*. INTECH Open Access Publisher, 2011.

[104] Shigeki Takeuchi et al. "Development of a high-quantum-efficiency single-photon counting system". In: *Applied Physics Letters* 74.8 (1999), pp. 1063–1065.

[105] Döndü Sahin et al. *Superconducting Devices in Quantum Optics*. 2016, pp. 61–83. URL: http://link.springer.com/10.1007/978-3-319-24091-6.

[106] Enectali Figueroa Feliciano. *Theory and development of position-sensitive quantum calorimeters*. 2001.

[107] D Fukuda et al. "Photon number resolving detection with high speed and high quantum efficiency". In: *Metrologia* 46.4 (2009), S288.

[108] Daiji Fukuda et al. "Titanium superconducting photon-number-resolving detector". In: *IEEE Transactions on Applied Superconductivity* 21.3 (2011), pp. 241–245.

[109] Adriana E Lita, Aaron J Miller, and Sae Woo Nam. "Counting near-infrared single-photons with 95% efficiency". In: *Optics express* 16.5 (2008), pp. 3032–3040.

[110] Antia Lamas-Linares et al. "Nanosecond-scale timing jitter for single photon detection in transition edge sensors". In: *Applied Physics Letters* 102.23 (2013), p. 1117.

[111] Brice Calkins et al. "Faster recovery time of a hot-electron transition-edge sensor by use of normal metal heat-sinks". In: *Applied Physics Letters* 99.24 (2011), p. 241114.

[112] F Marsili et al. "Detecting single infrared photons with 93% system efficiency". In: *Nature Photonics* 7.3 (2013), pp. 210–214.

[113] Justin D Cohen et al. "Phonon counting and intensity interferometry of a nanomechanical resonator". In: *Nature* 520.7548 (2015), pp. 522–525.

[114] H Bartolf et al. "Symbiotic Optimization of the Nanolithography and RF-Plasma Etching for Fabricating High-Quality Light-Sensitive Superconductors on the 50 nm Scale". In: *arXiv preprint arXiv:1011.4676* (2010).

[115] Chandra M Natarajan, Michael G Tanner, and Robert H Hadfield. "Superconducting nanowire single-photon detectors: physics and applications". In: *Superconductor science and technology* 25.6 (2012), p. 063001.

[116] K Miura et al. "Photowritten optical waveguides in various glasses with ultrashort pulse laser". In: *Applied Physics Letters* 71.23 (1997), pp. 3329–3331.

[117] Lionel Sudrie et al. "Study of damage in fused silica induced by ultra-short IR laser pulses". In: *Optics Communications* 191.3 (2001), pp. 333–339.

[118] EN Glezer et al. "Three-dimensional optical storage inside transparent materials". In: *Optics Letters* 21.24 (1996), pp. 2023–2025.

[119] Kazuyoshi Itoh et al. "Ultrafast processes for bulk modification of transparent materials". In: *MRS bulletin* 31.08 (2006), pp. 620–625.

[120] Nikolaos A Vainos. *Laser growth and processing of photonic devices*. Elsevier, 2012.

[121] James W Chan et al. "Structural changes in fused silica after exposure to focused femtosecond laser pulses". In: *Optics letters* 26.21 (2001), pp. 1726–1728.

[122] James W Chan et al. "Waveguide fabrication in phosphate glasses using femtosecond laser pulses". In: *Applied physics letters* 82.15 (2003), pp. 2371–2373.

[123] Ken-ichi Kawamura et al. "Holographic encoding of fine-pitched micrograting structures in amorphous SiO2 thin films on silicon by a single femtosecond laser pulse". In: *Applied Physics Letters* 78.8 (2001), pp. 1038–1040.

[124] P Dekker et al. "Annealing dynamics of waveguide Bragg gratings: evidence of femtosecond laser induced colour centres". In: *Optics express* 18.4 (2010), pp. 3274–3283.

[125] Shane M Eaton et al. "Heat accumulation effects in femtosecond laser-written waveguides with variable repetition rate". In: *Optics Express* 13.12 (2005), pp. 4708–4716.

[126] Dominik Bl et al. "Nonlinear refractive index of fs-laser-written waveguides in fused silica". In: *Optics express* 14.6 (2006), pp. 2151–2157.

[127] Alexander Szameit et al. "Control of directional evanescent coupling in fs laser written waveguides". In: *Optics express* 15.4 (2007), pp. 1579–1587.

[128] I Mansour and F Caccavale. "An improved procedure to calculate the refractive index profile from the measured near-field intensity". In: *Journal of lightwave technology* 14.3 (1996), pp. 423–428.

[129] DM Glowacka et al. "Development of a NbN deposition process for superconducting quantum sensors". In: *arXiv preprint arXiv:1401.2276* (2014).

[130] Dagmar Henrich. *Influence of material and geometry on the performance of superconducting nanowire single-photon detectors*. Vol. 10. KIT Scientific Publishing, 2013.

[131] Sascha Krause et al. “Epitaxial growth of ultra-thin NbN films on AlxGa1- xN buffer-layers”. In: *Superconductor Science and Technology* 27.6 (2014), p. 065009.

[132] JR Gao et al. “Monocrystalline NbN nanofilms on a 3C-SiC/Si substrate”. In: *Applied Physics Letters, 91 (6), 2007* (2007).

[133] Dimitar Dochev et al. “Growth and characterization of epitaxial ultra-thin NbN films on 3C-SiC/Si substrate for terahertz applications”. In: *Superconductor Science and Technology* 24.3 (2011), p. 035016.

[134] Zhen Wang et al. “Superconducting properties and crystal structures of single-crystal niobium nitride thin films deposited at ambient substrate temperature”. In: *Journal of applied physics* 79.10 (1996), pp. 7837–7842.

[135] A Kawakami et al. “Design and Fabrication of NbN terahertz hot electronolometer mixer”. In: *24th Int. Symp. on Space Terahertz Technology*. 2013.

[136] Tatsuya Shiino et al. “Improvement of the critical temperature of superconducting NbTiN and NbN thin films using the AlN buffer layer”. In: *Superconductor Science and Technology* 23.4 (2010), p. 045004.

[137] Haifang Yang et al. “Electron beam lithography of HSQ/PMMA bilayer resists for negative tone lift-off process”. In: *Microelectronic Engineering* 85.5 (2008), pp. 814–817.

[138] Behrooz Semnani et al. “Spin-Preserving Chiral Photonic Crystal Mirror”. In: *2019 Conference on Lasers and Electro-Optics (CLEO)*. IEEE. 2019, pp. 1–2.

[139] Ying Y Wang et al. “Compact and portable multiline UV and visible Raman lasers in hydrogen-filled HC-PCF”. In: *Optics letters* 35.8 (2010), pp. 1127–1129.